Surface Heat Flux Recovery during Short Duration Experiments–Conceptual Demonstration from Probe Design to Soft computing Analysis

A thesis

Submitted in Partial Fulfillment of the Requirements for

the Award of the Degree of

DOCTOR OF PHILOSOPHY

By

ANIL KUMAR ROUT

SCHOOL OF ENERGY SCIENCE AND ENGINEERING

INDIAN INSTITUTE OF TECHNOLOGY GUWAHATI

MAY, 2022

In the loving memory of my mother
Late Sebati Rout
who met an untimely death.

DECLARATION

I hereby certify that the work compiled in this dissertation is the outcome of the research work, performed by myself, else stated, under the guidance of **Prof. Niranjan Sahoo** and **Dr. Pankaj Kalita.**

Any part of this work has not been submitted for the award of any degree, diploma, associate-fellowship, fellowship or its equivalent to any university or institution.

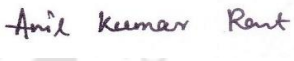

Anil Kumar Rout

Registration No. 166151109
School of Energy Science and Engineering
Indian Institute of Technology Guwahati

CERTIFICATE

It is certified that the work contained in the thesis entitled **"**Surface Heat Flux Recovery during Short Duration Experiments – Conceptual Demonstration from Probe Design to Soft computing Analysis**"** by **Mr. Anil Kumar Rout**, a student, in the School of Energy Science and Engineering, Indian Institute of Technology Guwahati, India, for the award of the degree of the Doctor of Philosophy, has been carried out under our supervision and, that this work has not been submitted elsewhere for the degree.

Date: 23.05.2022

Dr. Niranjan Sahoo
Professor
Department of Mechanical Engineering
Indian Institute of Technology Guwahati
Guwahati-781039, Assam, India

Dr. Pankaj Kalita
Associate Professor
School of Energy Science and Engineering
Indian Institute of Technology Guwahati
Guwahati-781039, Assam, India

Acknowledgements

"*Every successful work requires a lot of effort & support from many people, and this work has no difference.*"

This Preface is to express the author's gratitude to all those individuals who, with their generous co-operation, guided him in every aspect to make the thesis work successful.

In presenting this thesis, the author would like to express his sincere gratitude and Indebtedness to his Thesis advisers **Prof. Niranjan Sahoo,** Professor, Department of Mechanical Engineering, IIT Guwahati, Assam, and **Dr. Pankaj Kalita,** Associate professor, School of Energy Science and Engineering, IIT Guwahati, Assam for their valuable suggestion and requisite guidance in various aspects of this project work. It was a great pleasure for him to work under their supervision. This has been a precious opportunity for him to learn skills and approaches towards the work. They inspired him and remained a constant catalyst throughout the work. The author is also profoundly obligated to the Director of Indian Institute of Technology Guwahati to provide such pleasing circumstances for the inception of his research career.

Besides supervisors, the author would like to acknowledge the doctoral committee members, **Prof. Vinayak Kulkarni**, **Dr. Pranab Kumar Mondal, Prof. Sisir Kumar Nayak, and Dr. Balkrishna Mehta** for their valuable recommendations and insightful remarks throughout research activities, which has constantly engaged him towards undertaking a meaningful thesis work.

The author would like to convey his regards to the HOS, School of Energy Science and Engineering and HOD, Department of Mechanical Engineering, to facilitate the administration, which helped in smooth conduction of the experimental work.

The author would like to convey his esteems to **Prof. U.K. Saha** for his suggestions as and when required.

Further, the author would like to express special appreciation to the senior technician and support staff of the School of Energy Science and Engineering and the Department of

Mechanical Engineering for their valuable help. The author also likes to thank the CIF and workshop team for their support and co-operation.

The author would sincerely thank all his fellow lab-mates in the Gas dynamics Laboratory: **Dr. Sumit Agarwal, Mrs. Priyanka Dash**, **Mr. Abhishek Kamal, Mr. Anand Verma, Mr. Nikki Rajaura, Mr. Sashank Kulkarni, Mr. Menelik Walle**, **Mr. Himansu Sahoo, Mr. Deepak Yadav, Mr. Anurag Shrivastav, Mr. Gagan, Mr. Anurag, Mr. Pankaj, Mr. Amit Kumar, and Miss. Sima Nayak** for all the enriching and valuable discussions and sleepless nights spent working together. Without this group, the journey perhaps would have been less fun.

The author would like to rejoice in the support from all his Batch mates and colleagues from the School of Energy Science and Engineering, namely, **Ankita, Ojing, Samar, Sunita, Mrinal, and Muniraja.**

The author also owe thanks to his seniors, fellow mates and Utkalika family members namely, **Mr. Shuvayan, Mr. Siddesh, Mr. Rasmi Ranjan Behera**, **Mrs. DVN Lakshmi, Miss Sangjukta**, **Mrs. Nirja Kulkarni, Mr. Sibananda, Mr. Sujit, Mr. Abinash, Mr. Uttam, Mr. Ankan Mishra, Dr. Kajwal, Mr. Pratap Behera, Mr. Priyabrata Nath, Mr. Sangram, Mr. Rupak, Mr. Swagat, Mr. Sanjeev Mishra, Mr. Buddhadeb Maity, Mr. Dudul, Mr. Mrutunjaya, Mr. Gautam, Mr. Sibabrata, Mr. Bibhuti, Mr. Sritam, Mr. Biswa, Mr. Umesh, Mr. Manoj, Mr. Manmath, Mr. Tushar, Mr. Dillip, Mr. Subas, Mr. Niranjan, Mr. Subhasish, Miss Tapaswini, Mr. Prince, Mr. Bikas, Mr. Juba, Mr. Shailendra, Mr. Sandeep, Mr. Abhhishek, Mr. Swaroop, Mr. Lalatendu, Mr. Bighna, Dr. Asish Chaudhary, Mr. Adil, Mr. Achyut, Mr. Umang, Mr. Rabi, Mr. Rabindra, Mr. Ali, Mr. Pankaj, Mr. Bastav, Miss Amrita, Dr. Wittison Kamei, Dr. Amit Kumar. Dr. Avnish Tiwari**

As a special mention, the author would like to convey his love to **Dr. Soumya Ranjan Nanda** and **Dr. Saibal Kanchan Barik** for their unconditional support when needed, even when not asked.

This Ph.D. journey was made smoother due to the homely atmosphere created by a few families especially providing tasty foods and arranging many memorable gatherings. The author would like to convey his gratitude to them: **Nibedita Madam, Sana**, **Saukhyada**

Madam, Mihika, **Hota bhai and Sikha bhauja**, **Bidu bhai and Lipsa Bhauja, Lipu bhai and Lipi bhauja, Prakash bhai and Jayashree bhauja, Sunil and Kabita.**

Sincere Obligations to **Dr. M.M. Nayak**, Visiting professor, Centre for nano science and engineering, IISC, Bangalore, and **Dr. Sathesh Mariappan,** Associate professor, IIT Kanpur, for allowing the author to explore their labs and to carry out experiments.

Special thanks by the author to the Odia TV Channel Prarthana TV for the "Bhajan Antakhyari" program that remained a constant companion during night working hours.

Last but not least, the author owes his profound gratitude towards his parents and family members for being the constant guiding and supporting force throughout.

Anil Kumar Rout
Indian Institute of Technology Guwahati
May, 2022

List of publications

Journals:

1. Rout, A. K., Sahoo, N., & Kalita, P. (2020), "Effectiveness of coaxial surface junction thermal probe for transient measurements through laser based heat flux assessment". *Heat and Mass Transfer*, *56*(4), 1141-1152.
   DOI: https://doi.org/10.1007/s00231-019-02775-y

2. Rout, A. K., Sahoo, N., & Kalita, P. (2021), Transient Response Characteristics and Performance Assessment of a Calorimetric Surface Junction Probe Under Impulsive Thermal Loading. *Journal of Heat Transfer*, *143*(6), 062901.
   DOI: https://doi.org/10.1115/1.4050822

3. Rout, A. K., Agarwal, S., Sahoo, N & Kalita, P. (2021), "Fast response transient behaviour of a coaxial thermal probe and recovery of surface heat flux for shock tube flows". *Experimental Thermal and Fluid Science*, *127*, 110427.
   DOI: https://doi.org/10.1016/j.expthermflusci.2021.110427

4. Rout, A. K., Nanda, S. R., Sahoo, N., Kalita, P., & Kulkarni, V. (2021). Soft Computing—A Way Ahead to Recover Heat Flux for Short Duration Experiments. *Journal of Thermal Science and Engineering Applications*, *14*(3), 031008.
   DOI: https://doi.org/10.1115/1.4051726

5. Rout, A. K., Nanda, S. R., Sahoo, N., Kalita, P., & Kulkarni, V. (2021), "Implementation of Soft Computing Technique for Recovery of Impulsive Heat Loads". *Journal of Thermophysics and Heat Transfer*, 36(1), 108-117.
   DOI: https://doi.org/10.2514/1.T6269

Conferences:

1. Rout, A. K., Sahoo N. and Kalita P., "Experimental investigation of tapered surface junction probe in a shock tube", 5th National Symposium on Shock Waves, (**NSSW**),TBRL Chandigarh, Feb 26 - Feb 28, 2018. (**ID: IITG-006**)

2. Rout, A. K, Sahoo N and Kalita P, "laser based calibration of co-axial surface junction thermocouple for Transient temperature measurement", Proceedings of 7th International and 45th National Conference on Fluid Mechanics and Fluid Power (**FMFP**), IIT Bombay, Mumbai India, December 10-12, 2018 (**ID: 202**)

3. Rout, A. K, Sahoo N and Kalita P., "Characterization of High Frequency Thermal Sensor for Transient Temperature Measurement", International Conference on Advances in Materials and Manufacturing Engineering (**ICAMME),** KIIT University, Bhubaneswar, Odisha, March 15-17, 2019 (**ID-54**)

4. Rout, A. K, Sahoo N.,Kalita P. and Kulkarni V, "Transient Response Characteristics of a Surface Junction Probe"ASME 2019 Gas Turbine India Conference,(**GTINDIA)** December 5-6, 2019, Bangalore, India (**GTINDIA2019-2536**)

5. Rout, A. K, Hotta S.K., Sahoo N.,Kalita P. and Kulkarni V, "Validation for Fast Response Characteristics of a Co-axial Thermal probe in an IC Engine Based Experiment " 7th international conference on advances in Energy Research, (**ICAER)**, IIT Bombay, Mumbai India, December 10-12, 2019 (**ID-208**)

6. Rout, A. K, Sahoo N. and Kalita P. "Coaxial Thermal Probe as a Heat Flux Sensor: An Analytical, Numerical and Experimental Approach", Advances in Mechanical Processing and Design (**ICAMPD**), KIIT University, Bhubaneswar, Odisha, October 18-20, 2019. (**ID-20)**

Abstract

Recovery of surface heat flux in short duration experiments is a challenging task due to the dominance of unsteadiness in the temperature signal. Therefore, the heat flux estimation is carried out using the transient temperatures through suitable sensor modeling. In most of the cases (e.g., in thin-film gauges and coaxial probes), the sensor is assumed as a semi-infinite body with one-dimensional heat conduction through the sensing surface and substrate. In some cases, the surface heat flux is computed through numerical simulation. Nevertheless, all these processes involve various assumptions, simplifications and mathematical complications. In recent years, the advanced data science and soft computing methods are considered as important techniques in various applications. Therefore, the theme of the thesis is to introduce soft computing approach as a benchmark tool for recovery of surface heat flux in short duration experiments. The foremost intention of the present study is to implement a soft computing technique; Adaptive neuro-fuzzy inference system (ANFIS), to recover heat flux from the temperature signal in case of short duration experiments. The ANFIS technique needs a training process through known data sets (temperature signals and their corresponding heat flux). Therefore, the training data sets (transient temperature and surface heat flux) have been generated through various heat transfer experiments involving step and impulsive loads, convective and radiative heat loads. Side by side, numerical modelling of sensors (with similar experimental environment) is also considered as training data generation for ANFIS methods. Subsequently, inverse approach is followed to recover unknown (surface heat flux) parameters through trained data sets of ANFIS.

The short duration experiments (during millisecond flow duration) are characterized as transient for which there is no possibility of ensuring steady flow over a test model. In fact, these are the flow environments of ground-based aerodynamic experimental facilities (shock tubes and shock tunnels, expansion tubes). Capturing of the signatures of high-speed flows in these facilities need high frequency sensors. The calorimetric heat flux gauges (thin film sensors and coaxial surface junction thermocouples) are used to measure temperature responses from the flow environment for estimation of surface heat fluxes. These heat flux parameters are required for the management of “thermal protection system” of re-entry vehicles. Nevertheless, each sensor has advantages and limitations depending on the flow condition and experimental requirements. For example, the thin film gauges provide very fast response, but prone to shear after each blow-down. Apart from this, these probes are not efficient for measuring heat flux of higher order of magnitude. On the other hand, the coaxial thermal probes are rugged, can measure high heat flux, and have appreciable fast response. Unlike thin film gauges, it has the advantage of easy junction repair if lost during experimentation. Considering various advantages, coaxial thermal probes (CTPs) are found appropriate and cost-effective sensors at laboratory scale. An E-type CTP has been fabricated in-house from chromel and constantan materials. The constantan wire (0.91mm diameter and 15 mm length) is placed inside the chromel cylinder with a thin layer of insulation thickness

(~20 μm) in between them. The junction is prepared at the surface through the abrasion technique, which forms a junction between the two thermo-elements of the coaxial probe. The material property of the thermo-elements is obtained through energy dispersive *x*-ray technique and the internal as well as external surface dimensions have been checked through field emission scanning electron microscope. The sensor is calibrated experimentally using a glycerin bath to obtain the "sensitivity" value (relation between voltage and temperature). Similarly, water plunging and droplet techniques are used to obtain "thermal product value" of sensing substrate for surface heat flux estimation. Finally, the CTP is used to generate training data sets experimentally and the same sensor model is used for the numerical simulation.

Prior experimentation, the selection of an appropriate sensor for short duration experiments is the primary requirement. The ground-based experimental facilities are used for the generation of artificial shock wave over the aerodynamic models mounted in the test section. They mimic similar environment as experienced by the aero-vehicles during their realistic operation. In the present investigation, shock tube is used as an experimental tool for exposing the sensors for step heat loads with typical flow duration of 2 ms. By mounting the sensors at the driven section of the tube, the temperature response (static as well as stagnation) of shock wave can be captured. Due to the short experimental time scale, these facilities never have a scope for equilibrium (steady state) temperature measurement; thereby, the "heat flux" measurement leads the side as an essential thermal parameter.

As an experimental calibration of CTP for step/ramp heat loads, the E-type CTP is exposed to a laser source of known wattage and the corresponding temperature signals are recorded. In numerical simulations, step/ramp heat inputs (1W-5W) are applied to the CTP and temperature response are obtained using ANSYS module. All these signals are used for training and recovery purpose to test the applicability of the ANFIS system for short duration step/ramp thermal load recovery. The heat flux is recovered using ANFIS for two different modes of experimentation; convection and radiation. In the convection mode, the static temperature from the shock tube is recovered in a 2 ms time scale after training the system with known data set obtained from numerical simulation. For the radiation mode of experimentation, the heat flux signal is recovered from the trained ANFIS after training it with the combined signals from laser-based experiments and numerical simulations for 0.4s. The "time-temperature-heat flux" is used to train the ANFIS module using the Matlab platform, and the heat flux is recovered. These results are also compared with analytical and numerical heat flux signals obtained from the same temperature signal. Hence, it can be emphasized that ANFIS based soft-computing approach can be used as a potential computational tool for inverse prediction of short duration thermal loads in aerodynamic experiments.

Contents

Nomenclature and abbreviations

Nomenclature (Upper case letters)

A	Area (m^2)
D	Laser beam diameter (mm)
E	Electric field (V/m)
F_o	Fourier number
G	Individual gas constant (J/Kg. K)
K	Laser beam radius (mm)
M	Mach number
Q	Quality factor
O	Output in ANFIS network
P	Power (W)
R	To denote ramp angle in combination with θ
S	Seebeck tensor/Sensitivity (V/ºC)
T	Temperature (K)
V	Voltage (V)
Z	Sensor length (mm)

Nomenclature (Lower case letters)

a	Speed of sound in the driver section of the shock tube (m/s)
b	Insulation thickness (mm)
c	Specific heat (J/kg-K)
e	Standoff distance in laser setup (mm)
f	Focal length of lens (mm)
h	Heat transfer coefficient ($W/m^2 K$)
k	Thermal conductivity (W/m-K)
l	Distance between pressure sensors in shock tube (m)
m	Mass (kg)
p	Pressure (N/m^2, bar)
q	Heat load (W)
$\dot{q}$	Heat Flux (W/m^2)
r	Radial coordinate
t	Time (s)
u	Velocity (m/s)
w	Firing strength
x,y,z	Cartesian Co-ordinates

Greek Letters

α	Thermal diffusivity (m^2/s)
β	Thermal Product ($\sqrt{\rho ck}$, $Jm^{-2}s^{-1/2}K^{-1}$)
Δ	Change in the variable
δ	Uncertainty
ϕ	Radial angle (Degree)
γ	Specific heat ratio
η	Absorption coefficient
λ	Wave length of Laser (nm)
μ	Membership function
θ	To denote ramp angle in combination with R
ρ	Density (kg/m^3)
τ	Time constant of sensor (s)

Subscripts

1	Shock tube: Driven section initial condition ; Sensor: medium-1
2	Shock tube: Test gas condition behind primary shock ; Sensor:
3	Shock tube: Test gas condition behind contact surface
4	Shock tube: Driver section initial condition
5	Shock tube: Test gas condition behind reflected shock
6	Shock tube: Driver section final condition
∞	Ambient condition
a	analytical
ac	Uncertainty from experimental sources
ai	Uncertainty related to instrument
au	Uncertainty related to accuracy
av	Average
b	before
bw	Beam waist
ct	Contact
cu	Uncertainty from combined sources
FL	Fluid
in	Input
nu	Numerical
o	Initial
op	Overall output
pu	Uncertainty related to precision
s	Sensor surface

sh	Shock
TC	Thermocouple
w	water

Superscripts

•	Flux
*	Dimensionless parameter

Symbols

∇	Gradient
$\frac{\partial}{\partial x}$	Partial differentiation
$R_x\theta_y$	Ramp signal of (x) watt with ramp angle ($R_x\theta_y$)

Abbreviations

ALTP	Atomic Layer Thermopile
ANFIS	Adaptive Neuro Fuzzy Inference System
CFD	Computational Fluid Dynamics
CTP	Coaxial Thermal Probe
CW	Continuous Wave
DAS	Data Acquisition System
DIS	Direct Ignition System
ECU	Electronic Control Unit
EDX	Energy Dispersive X-ray Spectroscopy
EMF	Electromotive Force
FE	Field Emission
FESEM	Field Emission Scanning Electron Microscope
ht-CTP	High Temperature Coaxial Thermal Probe
ICE	Internal Combustion Engine
IITG	Indian Institute of Technology Guwahati
IMF	Input Membership Function
IR	Infrared
MF	Membership Function
OMF	Output Membership Function
PP	Pressure probe
RMSE	Root Mean Square Error

RPM	Revolution Per Minute
RTD	Resistance Temperature Detector
SEM	Scanning Electron Microscope
TCR	Temperature Coefficient of Resistance
TEM	Transmission Electron Microscopy
TFG	Thin Film Gauge
TP	Thermal probe
TSE	Transverse Seebeck Effect
VCR	Variable compression Ratio
YBCO	Yattrium-Barium-Copper-Oxide

List of figures

List of tables

CHAPTER 1

State of the art and objective of the work

Overview

The famous quote by J. Fourier "Heat, like gravity, penetrates every substance of the universe, its rays occupy all parts of space" is one of his influential statements that has motivated many researchers to study heat transfer in different objects. The measurement of heat transfer is one of the primary aspects of the development of civilization. In fact, the measurement process has evolved from making a guess i.e., "sense of cold or warmth," to quantification of the heat. The temperature being a measurable quantity has played a significant role through this process. Later, the temperature data is interpreted in various ways to find the heat flux density, which is a more convincing way of defining the heat transfer magnitude. Various sensors have been developed in due course of time to measure the temperature and heat flux. Some of the sensors are pretty useful for the measurement of steady-state phenomena; however fail to provide transient temperature data due to the constraint related to the time constant. In fact, many engineering systems require transient temperature and heat flux information for their efficient design and operation. For example, the ground-based experimentation of aerodynamic vehicles needs fast responsive sensors to capture the flow information. This is because the experiment time in these cases is very short, and the flow is highly transient. Apart from this, internal combustion (IC) engines and gun barrels are some examples where the transient temperature plays a vital role. Therefore, the present investigation focuses on developing a coaxial thermal probe (CTP) at the laboratory scale and studying its characteristics to capture transient flow phenomena in a shock tube and in an IC engine. A brief introduction to the various sensors available for transient temperature and heat flux measurement is elaborated in this chapter. A comparative review of the available sensors and their pros and cons, has been presented here. In addition, a comprehensive review of the available literature has been explained and the objective of the thesis has been framed.

1.1 Heat flux measurement in short duration flows: A brief discussion

The human desire to explore outer space has inspired as well as compelled researchers towards the development of modern aerospace vehicles. With technological advancement, many countries have progressed in rocket science, satellite launching, etc. Therefore, the development of satellites, space crafts, and re-entry vehicles has undergone a radical shift in a short period. Nevertheless, this development process is associated with many challenges and complexities. These high-speed re-entry vehicles often come across the deadly thermal influence induced due to the frictional effect between the atmosphere and the outer surface of such vehicles. Hence, pre-design criteria for such vehicles require the management of "thermal protection system" to survive those massive heat loads. Therefore, extensive ground-based experimentation is essential to determine the thermal loads impacted in similar environments (Agarwal et al., 2017). The categories of heat loads acting on the aero vehicles are instantaneous, leading to either step/impulsive in nature. The near-realistic experimental simulation of such flows is replicated in the test sections of different ground-based aerodynamic testing facilities such as shock tunnel, Ludwig tube, Expansion tube, etc. The high-speed nature of the flow in such testing facilities (except for continuous tunnels) prevails for a few milliseconds, within which the experimentation needs to be completed. Due to the short experimental time scale, these experimental facilities never have a scope for equilibrium (steady-state) temperature measurement, for which the "heat flux" measurement leads the side as an important thermal parameter. Therefore, an accurate estimation of wall/surface heat flux is essential for the proper design and optimization of prototype vehicles. The application can be extended manifold; to almost all engineering devices dealing with heat transfer and energy conversion. In addition to aerodynamic heating, transient temperature and heat flux parameters are also very important in design aspects of health monitoring in engines, gun barrels, etc. Therefore, the knowledge of transient temperature and heat flux are the essential thermal parameter for the design and modification of various engineering systems and sub-systems.

1.2 Temperature and heat flux

"Temperature" and "heat flux" are two key parameters whose magnitude are pretty essential for designing any thermal management system. Temperature is one of the

fundamental properties of a substance. In general, the temperature is a measurable quantity, whereas; heat flux is derived from the temperature data. The temperature can be easily determined by human senses; therefore, more people are familiar with its meaning. However, heat flux is a derived quantity that is not measured easily. The movement of thermal energy is known as “heat” and the rate of its transfer is called as “heat transfer”. The heat is denoted by a symbol $'q'$ having the unit of watts, whereas heat flux $(\dot{q})$ expressed as “Watt per $m^{2"}$. The heat flux is also reffered as thermal flux, heat flux density, or heat flux rate intensity which means a flow of thermal energy per unit area per unit time. Heat flux occurs wherever there is the nonequilibrium of temperature between two objects or between two points (Incropera et al., 1996). Being a vector quantity, the heat flux has both magnitudes as well as the direction in contrast to the temperature, which is a scalar quantity. The direction of the heat flux vector is always towards the lower temperature. However, in anisotropic bodies, the direction vectors of temperature and heat flux may be different.

1.3 Fundamental principles of heat transfer

The magnitude of heat flux can be measured with the help of heat flux sensors that work on the basic heat transfer principle. Heat flux sensors measure the “energy flux” onto or through the surface of interest where the energy source may be from conduction, convection, or radiation mode of heat transfer. When the transfer of energy takes place within a stationary medium (solid or liquid), it is defined as conduction mode. In contrast, when the heat transfer takes place between a moving fluid and a surface, maintained at a temperature gradient is termed as convection mode. Additionally, the third mode of heat transfer is the radiation mode which holds its principle that “all surfaces at finite temperature emit energy in the form of electromagnetic waves.” Therefore, without the interference of an intervening medium, there occurs a net heat transfer by radiation heat transfer between two surfaces maintained at different temperatures. In the case of combined heat and mass transfer, the effective heat flux may increase substantially than the value due to heat conduction only (Diller, 1999).

The heat transfer taking place through the conductive and convective process is associated with a temperature gradient where heat always flows from a higher potential to a lower potential. The conductive and convective heat fluxes are measured by allowing the heat flux through the sensor; however, radiative heat flux is measured with specialized

sensors having black absorbers. The role of the black absorbers is to convert the radiative heat to conductive energy mode. The transfer of heat taking place between the objects in real life mostly fall under the category of these three common modes of heat transfer. Therefore, an estimation of heat flux can be helpful to understanding many physical phenomena, for example, the amount of heat passed through a human body, through a wall, the energy from a laser source, energy from solar, etc. In some special cases, mass flux methods are also used for heat flux estimation. Often the spatial and temporal variation of the heat flux is important for performance enhancement. However, the simultaneous measurement of spatial and temporal measurement is difficult. The principle of conservation of energy (i.e., the overall energy to and fro a system is conserved) plays a significant role in the thermal analysis of the gauges. It includes all types of energy transfer across the system boundary, including the three modes of heat transfer. Therefore, in some cases, only the overall heat transfer from a system is required for the analysis. As shown in the **Fig. 1.1**, the transient energy balance on the control volume can be expressed as

$$mc\frac{\partial T}{\partial t} = q_{\text{convection}} + q_{\text{radiation}} - q_{\text{conduction}} \quad \ldots\ldots\ldots\ldots\ldots\ldots\ldots\ldots\ldots\ldots \text{(1.1)}$$

Where $'m'$ is the mass of the system and $'c'$ is corresponding specific heat. The effect of "heat capacity" (mc) or "thermal capacitance" of the material plays a major role in causing a time lag in the temperature response of the material subjected to a change in heat transfer (Diller, 1993).

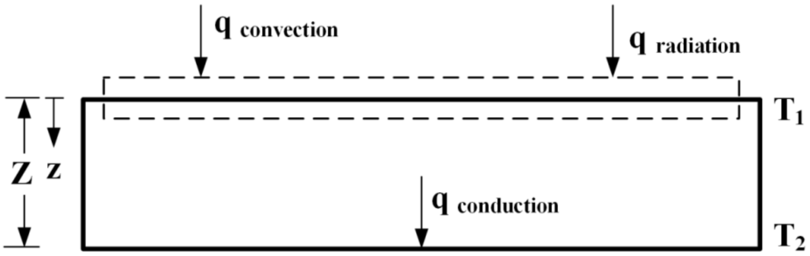

Fig. 1.1: Presentation of Energy balance

1.3.1 Governing equations of heat transfer

Conduction deals with heat transfer through a stationary medium due to the movement of electrons and protons. Here, the heat flux and temperature distribution are primarily

governed by Fourier's Law, which states that the heat flux vector is proportional to the temperature gradient and acts in the opposite direction of the gradient.

$$\dot{q} = -k\nabla T \quad \text{..... (1.2)}$$

The constant $'k'$ is the thermal conductivity of the material. Use of this temperature gradient is one of the elementary methods for determining heat flux. In Cartesian coordinates with an assumption of homogeneous material Eq. 1.1 becomes

$$\frac{\partial T}{\partial t} = \alpha\left(\frac{\partial T}{\partial x^2} + \frac{\partial T}{\partial y^2} + \frac{\partial T}{\partial z^2}\right) \quad \text{..... (1.3)}$$

The term $'\alpha'$ is the thermal diffusivity of the material. It can be expressed as $\left(\alpha = \frac{k}{\rho c}\right)$ where, $'\rho'$ is the density. As per this equation, determination of heat transfer by measuring the temperature response of the sensor can be considered as the second major method. Due to the complexity associated with the solutions of Eq. 1.3, this method can be complicated if multidimensional effects are considered. For a steady-state one-dimensional heat transfer assumption throughout the planar solid (**Fig. 1.1**), the temperature distribution in the heat flux $(\dot{q})$ direction is linear. Therefore, Eq. 1.2 can be simplified to a form as in Eq. 1.4 where; the temperatures are mentioned on either side of the material of thickness $'Z'$.

$$\dot{q} = -k\frac{T_1 - T_2}{Z} \quad \text{..... (1.4)}$$

The heat transfer in convection occurs by the same physical mechanism as conduction, but the fluid is free or forced to move relative to the surface. This fluid motion makes the analysis complicated by coupling the heat transfer problem with fluid mechanics, and the case becomes more complicated when the flow is turbulent. Therefore, the heat transfer and fluid mechanics are commonly separated by introducing a heat transfer coefficient which includes all the fluid flow effects.

$$\dot{q} = h_T\left(T_r - T_s\right) \quad \text{..... (1.5)}$$

Where 'T_r' is the fluid temperature whose value for low speed flows is considered as the temperature of fluid away from the surface. Whereas for high-speed flows, the recovery temperature is taken for analysis considering the effect of frictional heating in the fluid. The term 'h_T'corresponds to the heat transfer coefficient assuming a constant surface temperature 'T_s'.

Similarly, radiation phenomena occur by the electromagnetic emission and adsorption of photons. As this does not depend on a medium for energy transmission, it is different from conduction and convection in many ways. Radiation phenomena are associated with a spectrum of wavelength which is a function of temperature and characteristics of the emitting surface material. It may be noted that the surface properties are dependent on the wavelength and angular direction of the radiation. The power emitted from the detector may affect the results because the power emitted from a surface is proportional to the fourth power of the absolute temperature. Therefore, radiation detectors are often cooled sufficiently to minimize the effect. Unlike convection measurements, in case of radiation measurement, the distribution of the temperature on the sensor is not so important (Diller, 1999).

1.4 Heat flux measurement

The heat load encountered by the sensing surface of the sensor may be transient in nature or steady. The same sensor may or may not be capable of capturing the heat load in both cases. Some specialized sensors with fast response characteristics are required especially to capture the heat load in short duration experiments (e.g. hypersonic aerodynamic applications) where the entire event lasts for a few milliseconds. Nevertheless, in some cases, the sensors meant for short duration studies may be applied for long-duration studies but not vice-versa. Therefore, the measurement becomes challenging when the nature of heat load is highly transient in nature as prevails in the test section of “shock tubes” and “shock tunnels.” For years, different sensors have been developed and tested to capture such transient flows.

Most of the methods dealing with heat flux measurement depend on temperature data on the surface or close to the surface of the solid material. This process involves insertion of a device either onto or into the surface, which can cause both physical and chemical

disruption of the surface (Childs et al., 1999). However, a good sensor design always demands a minimum disruption due to the presence of the sensor (Wu et al., 2014). In fact, it is important to understand and identify the thermal disruption due to the presence of the sensor as it cannot be easily visualized, and most of the sensors depend on the change in temperature (Van der Graaf, 1995). Moreover, an appropriate selection of the sensor type and operating range is important for accurate heat flux measurements.

1.5 Heat flux gauges

There are different measurement techniques which are employed for heat flux estimation. The measurable outputs of most of the heat flux sensors are recorded in terms of temperature, voltage, or resistance. Therefore, the varieties of heat flux sensors can be classified into five different categories (Rodiger, 2010).

Type I: Sensors based on spatial temperature gradient: Here, temperature difference is measured over a spatial distance. The heat flux can be obtained using temperature gradient, material properties, and thermal resistance.

Type II: Sensors based on temporal temperature measurement: Here, the temperature difference is measured over time, and heat flux can be obtained with the knowledge of thermal capacitance.

Type III: Sensors based on direct energy exchange (Energy supply or removal): In this case, a direct measure of the input and output energy is made at a steady-state or quasi-steady-state).

Type IV: Sensors based on mass transfer analogy: An estimation of heat transfer is done here by measuring the mass transfer in place of energy transfer.

Type V: Sensors based on transverse Seebeck effect (TSE): In this case, the TSE causes a signal with linear dependency on the temperature difference across an isotropic film.

The working principles of these methods have been discussed in the following sections.

1.5.1 Sensors based on spatial temperature gradient (Type-I)

These sensors can provide output signals corresponding to the heat flux into or out of the surface. In fact, these gauges can provide continuous heat flux values as long as the signal is monitored. Here, the difference in temperature between locations in a component is monitored, and the heat flux is determined using conduction analysis with the knowledge of thermal properties. Common heat flux sensors that use this principle are "differential layered sensors," "planar differential temperature sensors," "circular foil gages," "wire-wound gages," etc. Among these sensors, a description of a few sensors has been given here.

Differential layer sensors

The measurement of the temperature difference across a spatial distance within a medium and subsequent heat flux calculation is the basic philosophy of this method. The temperature difference can be measured by using any one of the popular temperature sensors e.g. thermometers, thermocouples, thermistors, thermopiles, resistance temperature detectors (RTDs), etc. (**Fig. 1.2**). Apart from this, radiation-based devices or optical temperature measuring methods can also be used. The selection of the technique for temperature measurement depends on the measurable output parameter and sensitivity corresponding to the range of heat flux under consideration. Thereafter, Fourier's one-dimensional law of heat conduction (Eq. 1.2) can be used for the evaluation of heat flux. The important concern and also limitation of this method is that the heat flux must be one-dimensional across the space under consideration (Diller, 1993).

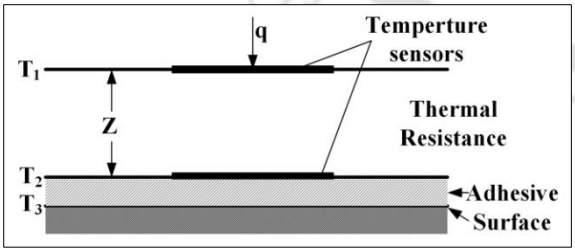

Fig. 1.2: Schematic representation of a layered gauge (Diller, 1999)

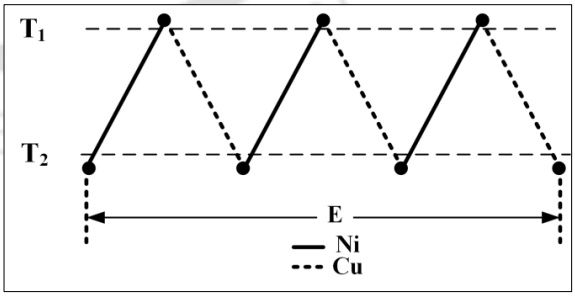

Fig. 1.3: A thermopile circuit for differential temperature measurement (Diller, 1999)

Planar differential temperature sensors

In differential layer sensors, the temperature is measured across a thermal resistance layer. In this method, a thermal gradient can be artificially created by using alternate layers of materials of different thermal conductivity or varying thickness or by exposing some part of the sensor to a convective boundary condition (e.g. the gradient can be achieved by exposing one-half of the thermopile junctions to a convective fluid flow). It may be noted that the thermopile sensor is a combination of several thermocouples connected in series (usually) or parallel (less likely) (**Fig. 1.3**).

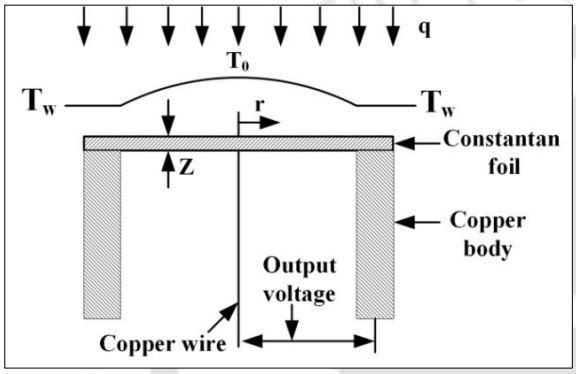

Fig. 1.4: Schematic of a circular foil gauge. (Diller, 1993)

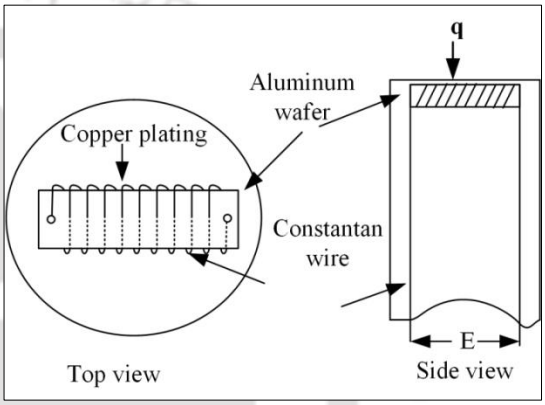

Fig. 1.5: Schematic of a wire-wound gauge (Diller, 1993)

Circular foil gauges

These gauges were originally proposed by R. Gardon to measure radiation heat transfer therefore; these are popularly called as "Gardon gauges" (**Fig. 1.4**). Thereafter, it is found suitable for measuring convective heat flux. Consequently, it is used in a wide variety of situations. The difference in temperature between the center and the edge of the disk is measured using a differential thermocouple. The unique feature of the gauge is that the heat transfer is not in the same direction that it enters the surface. The heat energy is transferred to the heat sink (present at the edge of the disk) after being collected by the disk.

Wire-wound gauges

This gauge is commonly known as Schmidt-Boelter gauge (**Fig. 1.5**). The concept used for this gauge is similar to the idea of the thermopile. Here, a fine wire of one of the

thermocouple thermo-element (say constantan) is wrapped for N terns around the thermal resistance layer. Half of the wire is electroplated with other thermo-element (say, copper). This forms a set of thermocouple junctions or a thermopile with N number of junctions.

1.5.2 Sensors based on temporal temperature measurement (Type-II)

Unlike differential temperature methods, this method requires a single temperature to calculate heat flux at a particular location. Moreover, a heat balance is applied to a particular region, and the temperature-time history is recorded for time-varying heat flux calculation. This method is popularly known as the "calorimetric method." The principle works by solving the heat conduction equation in the gauge as well as wall material through various approximations. Therefore, the solution type varies depending on the gauge under consideration and the assumptions used. The slug calorimeter, null point calorimeter, thin skin gauges, thin film gauges, coaxial thermocouples are common examples of these type of gauges. The working principle of some of the gauges is explained briefly here.

Slug calorimeter

The amount of energy absorbed can be measured by a calorimeter. A slug calorimeter often uses a single point temperature (at the back surface) to represent the complete slug of mass (**Fig. 1.6**). The slug of mass is mostly a high conductive material (say copper) which has a minimal thermal resistance and high thermal conductivity. Therefore, the single-point temperature representation is justified. By applying conservation of energy principle around a control volume in the vicinity of the slug, the conservation equation can be written as

$$q = mc\frac{dT}{dt} + q_{loss} \quad \text{..... (1.6)}$$

Where, "q" is the heat entering to the gauge which is to be measured and "mc" is the thermal mass of the slug. The heat loss is minimized by insulating all the exposed surfaces except the sensing surface. Several solutions can be obtained by neglecting the losses depending on the nature of the heat flux. If "$\dot{q}$" is constant with time and constant spatially over the gauge, the temperature of the gauge increases linearly with time.

$$T = T_o + \frac{\dot{q}A}{mc}t \quad \text{..... (1.7)}$$

The solution to the equation is exponential of the form.

$$\frac{T - T_\infty}{T_o - T_\infty} = e^{-t/\tau} \quad \text{..... (1.8)}$$

The time constant can be written as

$$\tau = \frac{mc}{hA} \quad \text{..... (1.9)}$$

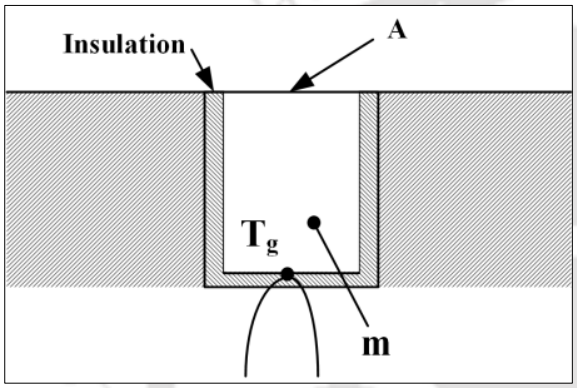

Fig. 1.6: Schematic of slug calorimeter (Diller, 1993)

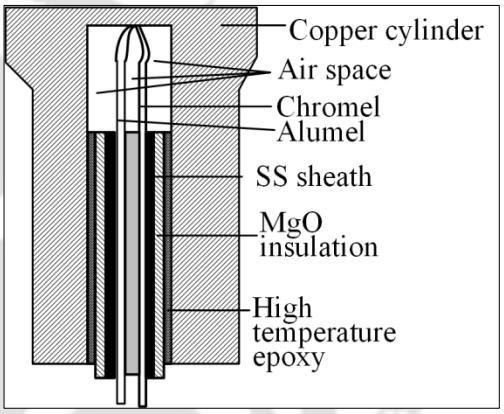

Fig. 1.7: Schematic of null point calorimeter (Diller, 1993)

Null point calorimeter

The null point calorimeter is mostly used for transient heat flux measurement. Here, the thermocouple position is placed much closer to the sensing surface as compared to the slug calorimeter. This improvement provides a temperature that is much closer to the actual surface temperature and also a much faster time response. Due to these improved characteristics, the sensor is named as null-point calorimeter. Various analytical modeling has been carried out to find out the optimum geometrical configuration for the size and depth of the hole along with the position of the thermocouple, as shown in **Fig. 1.7**. The main aim of this design is to have the same temperature history at the null point (thermocouple position) as would occur on the surface of a semi-infinite slab of the model if the gauge was not present. Due to this, a number of data reduction schemes have been developed for the temperature and heat flux on a semi-infinite substrate with one-

dimensional transient heat transfer. One common method based on linear spline fits of the temperature history is given by

$$\dot{q}(t_n) = \frac{2\sqrt{k\rho c}}{\sqrt{\pi}} \sum_{i=1}^{n} \frac{T_i - T_{i-1}}{\sqrt{t_n - t_i} + \sqrt{t_n - t_{i-1}}} \quad \ldots\ldots\ldots\ldots\ldots\ldots\ldots\ldots\ldots\ldots \quad (1.10)$$

Thin skin gauges

The thin-skin method can be considered as a continuous slug calorimeter that forms the entire body of a model. The term "thin" is used to indicate the constant temperature assumption through the material except in the transverse direction along the skin. The local temperature is measured by placing thermocouples on the backside of the skin. The heat flux at the measurement location is calculated from the transient temperature data using Eq. 1.1. More details for these types of sensors can be obtained from the reference (Schultz and Jones, 1973).

Thin film gauges

The thin-film method completely dominated over the thin-skin method for the purpose of aerodynamic testing due to various reasons. The improvement in the sputtering technique or thin film deposition technique is the major reason which simplified the fabrication of resistance elements on the surface of models that ultimately ease the temperature measurement. Due to the minimal thickness of the thin films (less than a micrometer), the initial response is very fast $(<1\mu s)$. When these gages were placed on any model having insulating substrate, the temperature response is quite appreciable with very minimal thermal disruption.

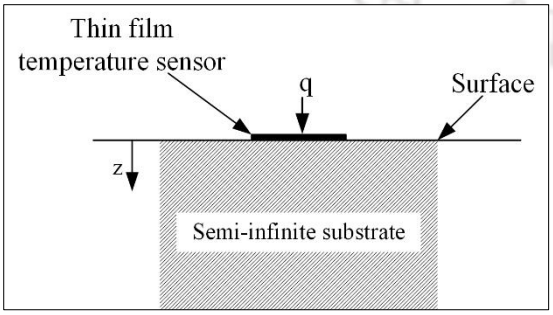

Fig. 1.8: Schematic of thin-film gauge (Childs et al., 1999)

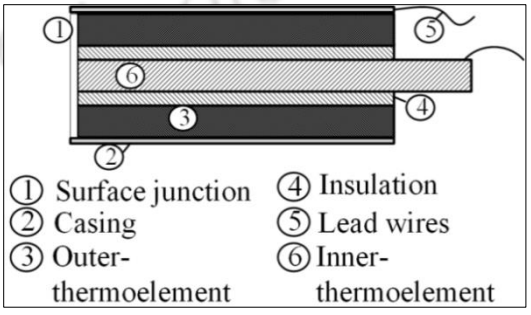

Fig. 1.9: Schematic of coaxial thermal probe (Schultz and Jones, 1973)

The operating principle of the thin-film gauges is to measure the surface temperature of a semi-infinite material (substrate) in response to the applied surface heat flux (**Fig. 1.8**). The biggest drawback for these sensors when exposed to high-speed flows is the film degradation, i.e., during high speed and high-temperature testing, the gauges placed on the model surface experience degradation. More details regarding the sensor can be obtained from the research article (Schultz and Jones, 1973).

Coaxial thermocouples

The working approach of the coaxial thermocouple is to record the model wall surface temperature at a certain time interval and then Eq. 1.10 can be used to find out the corresponding heat flux. These thermocouples are preferred widely due to the ease of fabrication compared to the null point calorimeters. The concept of fabrication is a bit simple as one thermoelement forms the center wire which is surrounded by an electrically insulating material (**Fig. 1.9**). The other thermoelement of the corresponding thermocouple forms an outer sheath around these two layers. The final assembly often takes the shape of a small diameter and is usually fitted in the desired model at an appropriate location. The connection between the two thermoelements is formed at the top end by plating a thin layer of one of the thermoelement materials, vacuum deposition, or gently sanding to mix the two thermoelements and bridge the insulating layer (Mohammed et al., 2008).

1.5.3 Sensors based on direct energy exchange or active heating (Type-III)

This technique relies on a physical balance between incoming and outgoing heat. A direct calculation of the energy transfers under steady-state conditions into or out of a surface can provide an accurate measure of the surface heat transfer. The electric circuits are mainly used as a heat source, and sometimes pulsed lasers are also used. Cooling can be done using convective passage ways within the device or through the Peltier effect. Due to time constraints (response time) and power limitations, these sensors are not recommended for high heat flux and high-temperature situations. Therefore, these sensors are not preffered for high-speed flows. Instead, these sensors can be used for steady-state measurements in well-controlled laboratory environments. Many researchers have used this method to prepare customized sensors based on constant heat flux boundary

conditions and constant temperature boundary conditions. More details regarding these sensors are elaborated in reference (Diller, 1993).

1.5.4 Sensors based on mass transfer analogy (Type-IV)

The governing equations that describe the transport of energy and mass contain some similarities between them, which can be utilized to correlate the quantitative estimation of heat transfer as a function of mass transfer. The advantage of this experiment is the ease of carrying out such experiments compared to other heat transfer experiments, especially on complex or difficult geometries. Additionally, these experiments are less prone to experimental uncertainties and errors. One of the best methods is the “naphthalene sublimation technique.” The naphthalene can be evaporated and converted directly from solid-state to vapor without any intermediate stage. Apart from this, "naphthalene can be easily cast into the desired shape. The naphthalene is applied on the surface of interest either through casting, machining, spraying, etc. The mass distribution of the naphthalene is measured before and after the experiment, and the mass is correlated with the heat transfer. This method may not be suitable for transient measurements rather can be useful for continuous experiments. The detailed procedure of this process is elaborated in reference (Childs et al., 1999).

1.5.5 Sensors based on transverse Seebeck effect (TSE) (Type-V)

The Seebeck effect for thermoelectric technology involves the direct energy conversion between heat and electricity. The relation is well established in the form $E = S\nabla T$ where, E is the electric field, S is Seebeck tensor, and ∇T is the temperature gradient which is not necessarily collinear. Conventional thermoelectric devices use only the diagonal term of the tensor S i.e. (S_{ii}) with an additional assumption of collinearity between the electric filed and the temperature gradient. On the other hand, the “transverse Seebeck effect” utilizes the off diagonal term of tensor S, i.e. $S_{ij}(i \neq j)$. To have non-vanishing off-diagonal terms, the material should have anisotropic transport properties. The principal axes of material anisotropy need to be tilted with respect to thermal input and electric output directions. Various materials exhibit these anisotropic properties; however, the material that is under focus is Yattrium-Barium-Copper-Oxide (YBCO). This crystal is the main constituent in the fabrication of the sensor known as “Atomic layer thermopile

(ALTP)". The working principle of ALTP is based on the thermoelectric field created by a temperature gradient inside a YBCO crystal (**Fig. 1.10**)**.** This sensor has a time constant of $<1\,\mu s$ and can work in a frequency range up to 1 MHz. Therefore, these sensors are quite helpful in capturing transient heat flux values. More details regarding the sensor can be obtained from the literature (Rodiger, 2010).

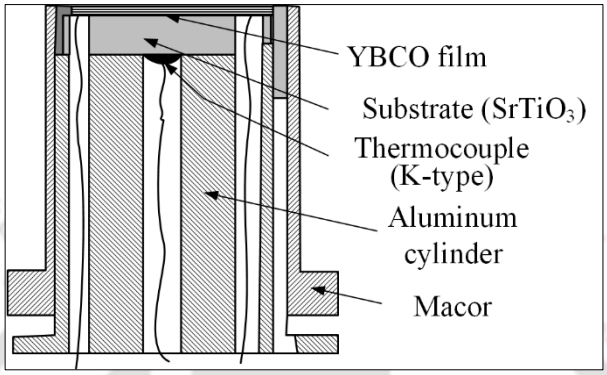

Fig. 1.10: Schematic cross-section of ALTP sensor module (Rodiger, 2010)

From the study of various sensors, it is observed that all the sensors are not meant for the measurement of transient temperature and heat flux. A comparative assessment of eligible sensors has been presented in **Table 1.1**(Childs et al., 1999; Diller, 1993; Diller, 1999; Rodiger, 2010; Schultz and Jones, 1973). Among the few qualified sensors, thin-film gauges (TFG) and coaxial thermal probes (CTP) are mostly preferred for impulsive applications like shock tubes and shock tunnels. The TFGs are prepared by placing a thin layer (~ few microns) of highly conductive material (gold, silver, platinum, nickel, etc.) on a non-conducting substrate (pyrex, quartz, etc.). The conductive layer is deposited over the substrate either through hand panting, sputtering, or vacuum deposition. The coating is fragile due to the weak bonding between metal and insulator. Similarly, the CTPs are prepared from bare thermo-elements by placing one thermo-element in the other's annulus, making it both concentric and coaxial. Nevertheless, each sensor has its benefits and demerits, e.g., in high-speed flow environments, the metallic residues present in the TFGs are often prone to wear, for which the thin film gets eroded out of the substrate with repeated trials (Irimpan et al., 2019). This process results in a change in resistance of the sensor and ultimately induces measurement errors for which the sensor is required to be replaced after almost each blowdown of the tunnel. Moreover, these sensors are passive, requiring an external constant current circuit to provide an external excitation for the

measurement, often attracting measurement uncertainties through self or Ohmic heating. On the other hand, CTPs are rugged, do not require replacement like thin films, and can be easily repaired if the junction is lost. Additionally, these probes are active sensors; produce emf when subjected to temperature change obeying the Seebeck effect (Mohammed et al., 2008). Therefore, considering the various advantages associated with the coaxial thermal probes, it has been selected for the present research work.

1.6 Survey of literature

Owing to the advantages associated with the coaxial thermal probe, it is found to be well fitted for the transient temperature measurement during short-duration flow conditions. Hence, it is proposed to have an in-depth investigation about the coaxial thermal probes and to review the associated heat flux recovery techniques. Therefore, a thorough literature review has been carried out to get an insight into the developments and progress of the coaxial probe to date. The survey has been categorically divided into different aspects and is placed in the subsequent sections.

1.6.1 Mathematical modeling of the calorimeter gauges

The coaxial thermal probe falls under the category of "calorimetric gauges," where the probe is used to capture the transient temperature history. Subsequently, the sensor is modeled according to the basic heat transfer principle. One such common method which is preferred for the CTPs and for a few other gauges (such as thin-film gauges, thick film gauges, etc.) is the semi-infinite assumption for the substrate having one-dimensional heat conduction (Schultz and Jones, 1973; Taler, 1996). The concept is generalized with the principle of mounting the gauge on a semi-infinite extent of another material. However, for CTP, the junction is prepared at the surface, and the entire sensor (except the sensing surface) can be assumed as a semi-infinite substrate. Due to the small time scale of application, the concept of one-dimensional heat conduction can be considered valid.

Table 1.1: Summary of popular heat flux sensors for high-speed aerodynamic experiments.

Heat flux Sensors	Working principle	Pros	Cons
Thin Film Gauge	A change in resistance of a metallic film subjected to change in temperature.	# Highly sensitive # Micro second response time	# Passive sensor (requires external power) # Problem with long term film sustainability: (degradation of sputtered thin metallic film due to high thermal stress or due to particle impact) # Individual sensor calibration is required # High-end equipment is needed for film deposition
Gardon Gauge	Heat flux derivation using differential temperature method by measuring temperature across a spatial distance.	# Active sensor (Does not require any external power) # Can measure high heat flux # Suitable for both steady and unsteady state	# Does not have fast response # Requires cooling (mostly water-cooled)
Schmidt-Boelter Gauge	The principle is similar to Gardon gage, but a single strand of a thermocouple thermo-element (say constantan) is wrapped N-turns around the thermal resistance layer forming an N-pair of thermocouple junctions.	# High durability # Sensitivity is appreciable # Output is directly proportional to heat flux	# Limitation with service temperature (~370 ºC). # Calibration is a challenging task, especially at elevated temperatures.
Heat Flux (using thermocouple)	Indirect measurement of heat flux using Fourier's law by placing thermocouples at a known distance	# Simplicity in construction as it uses readily available components	# Heat flux derivation deals with the 1D heat transfer assumption.
Heat Flux (using IR Camera)	Works on the principle of the optical pyrometer.	# Continuous acquisition can be performed	# High cost # Proper calibration is a challenge # Only applicable to setups with optical access.
Atomic Layer Thermopile (ALTP)	Works on the principle of transverse Seebeck effect	# Direct heat flux can be measured # Micro-second response time	# Application is limited to relatively low temperature and low heat flux # Frequent calibration is required
Thermal/Pressure Sensitive Paints	Change in colour takes place in the thermo-sensitive paint corresponding to the heat flux	# Relatively lower cost # Non-intrusive technique	# Calibration is a challenge # Requires re-application of paints
Coaxial Thermal probe	A change in voltage output is subjected to a change in temperature at the junction.	# Robust, highly durable # Suitable for harsh environments # Suitable for high pressure and high heat flux # Micro-second response time # Active sensor (does not require any external power)	# Recovery of heat flux depends on the surface temperature history, assuming the sensor as semi-infinite body # The heat flux is deduced in the direction perpendicular to the sensing surface.

Brief history, Design, fabrication, characterization, and calibration of the probe

Brief history, design, and fabrication

The coaxial thermocouple was developed many years after the discovery of the thermoelectric effect by Thomas Seebeck (1821), which is the basic governing principle of thermocouples (Velmre, 2007). As per the literature, the coaxial metal wall surface thermocouple was first documented in 1941 by P. Hackemann in Germany. Further development in this work was carried out by D. Bendersky at the Midwest Research Institute (MRI, 1953) and later by C.E. Moeller (1954 to 1966) (http://www.techno-office.com/file/MED_TCS.pdf). The Bendersky design was adopted during that time, which was made up of a small wire coated with very thin layer of aluminum oxide insulation (Bendersky, 1953; Mohammed et al., 2008). Other probes were fabricated using aluminum oxide and Sauereisen binder as insulating material. A small alumel wire was coated with the aluminum oxide, which was put on in the form of an aluminum nitrate solution. The Sauereisen binder was applied for every five layers of aluminum oxide. The outer element (chromel) was prepared in a tubular form through wire drawing technique with the help of different dies. The coated alumel was placed inside the chromel cylinder after drying the insulation using a Bunsen burner. The assembly was wire drawn to get its final shape and then mounted on a chromel strip. The thermocouple was polished flush with the surface, and the junction was created by scratching the surface with a sharp needle so that the insulation between the alumel and chromel tube was bridged. Subsequently, the deposition technique was adopted to create the junction between the two thermo-elements of the thermocouple (Kovacs and Mesler, 1964).

In some cases, the concept of surface junction thermocouple was interpreted differently, i.e., one approach was to put the thermo-elements in parallel and creating a junction at the surface. This practice was mostly adopted to measure the static and dynamic temperature on the inner wall of a combustion chamber during engine working. The bare thermo-element of the thermocouple (say iron and constantan) was inserted through the hole till it exposed to the combustion chamber. The wire was insulated carefully with specialized materials such that there was no contact between the thermo-elements and no contact of any of the thermo-

elements with the body of the engine cylinder. The criteria includes a stronger insulation compared to the impedance of the thermocouple, and the insulation should act as a binder keeping things intact. Both the protruding ends of the thermocouple were polished flush with the surface of the engine cylinder using sandpaper which served as a sensing surface (Ongkiehong and Duijn, 1960). Similarly, probes were also prepared by putting a deposition over two parallel wires of the thermocouple, which was popularly called a "pair wire thermocouple." Here, two thermoelements were separated by insulation and swaged together inside a tube; however, as the name suggests, pair-wire thermocouples use two thermo-elements wire installed next to each other instead of one wire inside a tube of the second thermoelement (Madison, 2013). A diagram showing sectional view of the thermocouple is shown in **Fig. 1.** 11. The junction were made either by vacuum depositing a thin metallic layer on the surface or by bending one wire over another.

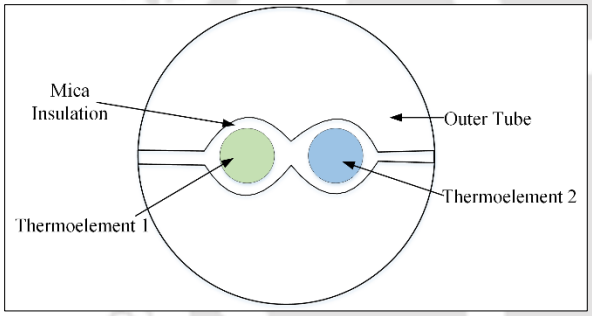

Fig. 1. 11: Schematic of pair wire thermocouple (Madison, 2013)

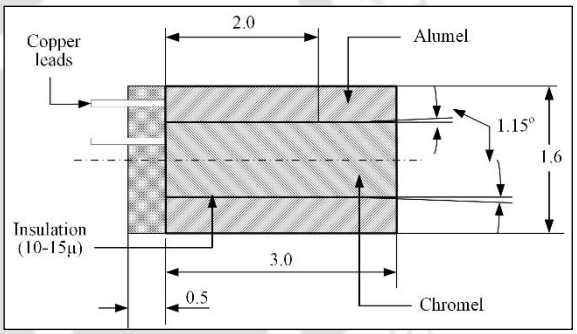

Fig. 1. 12: Schematic of a tapered probe (Desikan et al., 2016)

Probes were also fabricated with different designs (**Fig. 1.** 12) and also with the help of ribbon elements (**Fig. 1.13**). In case of thermocouples fabricated by using ribbon elements, ribbons are insulated from each other except at the exposed surface, where the insulation is again bridged either through plastic deformation of the thermoelements of the thermocouple or by the application of metallic plating. In fact, it is a special type of pair-wire thermocouple. These thermocouples have two flat ribbons of thermoelements instead of circular wires. The ribbons are separated and insulated by thin mica sheets and are pressed into a wide variety of substrates. A diagram of this type of thermocouple is shown in **Fig. 1.13.** The junction can be formed either by surface deposition or by abrading the surface

(Buttsworth et al., 2005). The “eroding” in its name refers to the ability to continually reform the hot junction as the surface erodes away. The eroding ribbon design has a uniqueness that, it is intended to remain functional even if the surface is worn away over time.

Coaxial thermocouples were fabricated by many researchers considering different dimensions (for the outer and inner elements), different insulation thicknesses, different insulating materials. One interesting work was carried out by Olivier and Gronig for simultaneous measurement of pressure and temperature at a location (at a spatial deviation of 1.5mm) in the Aachen shock tunnel. This work was focused on the fabrication of a customized coaxial thermocouple which had the provision to hold the Commercial Kulite pressure transducer, and both were placed under a single adapter (Olivier et al., 1995). The E-type thermocouple was prepared with chromel as an outer tube having 4.8mm diameter and constantan as inner element with 3 mm diameter, and both were insulated from each other by a dielectric material of 10µm thickness. The pressure hole (0.8mm) was drilled inside the inner element, which ultimately connected to the pressure gauge. Similarly, a K-type coaxial thermocouple was used for testing in UNITEN’s shock tube facility (Mohammed et al.). Here, a chromel wire of 1mm diameter was symmetrically disposed in the hollow cylinder made in alumel (3mm diameter), and both were separated by a thin film of electrical insulation of a few micrometer thicknesses (Mohammed et al., 2008).

The junction formation through abrasion technique is uncontrollable therefore, impart different thermal product values (Irimpan et al., 2015). To avoid this, a tapered type design of the coaxial thermal probe was developed (Desikan et al., 2016) which is the modified version of the original probe developed by (Sanderson and Sturtevant, 2002). The inner material (chromel, 0.8mm diameter) was provided a 5:1 tapper for a distance of 2mm which was inserted in the cylindrical hole of 0.84mm diameter drilled in the alumel (1.6mm diameter and 3mm length) with a thin layer of insulation in between. The tapper helps in the formation of a thin contact between the two thermoelements at one end, which provides a fast response to the thermocouple (**Fig. 1.** 12).

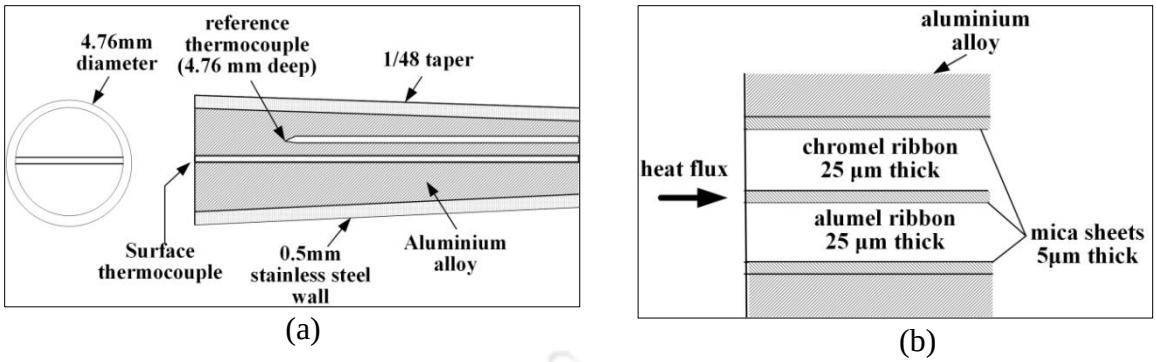

Fig. 1.13: Schematic of eroding ribbon thermocouple ; (a) Side view (b) Zoomed view near sensing surface (Buttsworth et al., 2005)

Characterization

The materials used as thermocouple thermo-elements are metal alloys consisting of different materials with varying percentages of composition. The composition of thermocouple materials is usually certified by manufacturers. However, sometimes locally available materials are used for fabrication. During that condition, the characterization of the material is required. Apart from this, the ideal composition of the sensing surface does not remain intact after the junction formation especially through the abrasion technique. During such conditions, the material characterization also helps. The energy dispersive x-ray technique and x-ray diffraction technique is popularly used by various researchers for finding the material composition (Manjhi and Kumar, 2019b; Mohammed et al., 2008). Apart from this, the inside and outside texture of the probe is required to be studied in minute detail. Therefore, the scanning electron microscopy (SEM) technique has been used by many researchers (Mohammed et al., 2008). An *x*-ray of the complete sensor is performed by few researchers to identify the internal configuration (Desikan et al., 2016).

Calibration

While solving the heat flux equation of the form as given in Eq. 1.10 or any other basic form, the requirements are the time-temperature history and the magnitude of the thermal product. Being an active sensor, these probes generate an electromotive force (EMF) corresponding to the change in temperature. A factor for converting the EMF to temperature is the inherent requirement which is popularly known as sensitivity of the probe, often interpreted as the

ratio of change in EMF to the change in temperature. Therefore, many authors have used the static calibration procedure to obtain the actual sensitivity of the probe within a definite temperature range. A hot water bath is often preferred for static calibration at a lower temperature range (~25ºC-80ºC) by many researchers (Manjhi and Kumar, 2019b). For a medium range of temperatures (~ 200ºC-250ºC), glycerin bath, silicone oil bath, or specialized medium-range ovens are used (Agarwal et al., 2016). For high-temperature calibrations (~500ºC-1000ºC), solid block heating, alumina powder bath, or high-temperature furnaces are used (Agarwal, 2018). In all these calibrations, the thermal probe is put in the calibration bath along with a reference temperature sensor. The temperature is noted from the reference probe and the emf generated by the thermal probe (corresponding to the same temperature) is recorded by the data acquisition system. The slope of the plot temperature vs. EMF provides the sensitivity of the probe.

Like sensitivity, the thermal product value also plays an essential role in estimating heat flux. As per the conventional analysis of a calorimetric probe with semi-infinite substrate and one-dimensional heat conduction approximation, the thermal product is considered as $\sqrt{\rho ck}$ Here, ρ, c and k are the density, specific heat, and thermal conductivity of the substrate material, respectively. These values are constant for insulating substrates (say macor/pyrex in case of thin-film gauge) but vary for the conducting substrates like coaxial probes (Schultz and Jones, 1973). In addition, the surface junction, when prepared through abrasion technique, provides a mixture of constituent elements which varies for different probes. Therefore, experimental determination of thermal product magnitude is preferred by many researchers. For the experimental determination of thermal product value, the plunging and droplet methods are preferred due to the experimental simplicity. In both methods, the sensor at room temperature is exposed to a heated fluid or vice versa. With the help of known ρck value and one-dimensional heat conduction theory, a simple relation is used for the determination of the ρck value of the thermal probe as given in literature (Olivier et al., 1995). For a water plunging technique with a hot water bath, Eq. 1.11 can be used to determine the $\rho ck-$ value of the thermocouple. This requires the knowledge of the initial

temperature of the fluid (T_{FL}), the initial temperature of thermocouple (T_{TC}), the contact temperature measured by the probe (T_{ct}) and the ρck value of the heated fluid.

$$(\rho ck)_{TC} = (\rho ck)_{FL} \frac{T_{ct} - T_{FL}}{T_{TC} - T_{ct}} \quad \text{..... (1.11)}$$

A different form of Eq. 1.11 for the droplet method was proposed where, a cold water droplet at temperature T_w was allowed to fall on the heated thermocouple at a temperature T_s that ideally resulted in a step-change in the temperature at the water-thermocouple interface. The temperature at the surface of the thermocouple, T after coming in contact with water, can be expressed through Eq. 1.12 where, β_w stands for the thermal product of water and β_s stands for the thermal product of the sensor. This equation is valid to a condition where the droplet does not undergo any rebound after coming in contact with the surface (Buttsworth, 2001).

$$\frac{T - T_s}{T_w - T_s} = \frac{\beta_w}{\beta_w + \beta_s} \quad \text{..... (1.12)}$$

With the knowledge of temperature response and the thermal product of water, the thermal product of the sensor can be obtained. Thereafter, many authors have used Eq. 1.12 to calculate the thermal product value for the sensor. The determination of thermal product for an E-type probe used in aerodynamic experiments is explained in the literature. (Mohammed et al., 2011; Mohammed et al., 2010).

Another important aspect of this type of probe is the accuracy of heat flux assessment from the transient temperature signal. Therefore, these probes were calibrated with a known heat flux supply, and the recovered heat flux values were compared to get an estimate about the heat flux trend and also about the error percentage for the time average magnitude. Researchers have used various sources to provide heat load to the probe such as Laser sources (Kumar et al., 2011; Sarma et al., 2016a), halogen lamps (Alam and Kumar, 2018), well directed sunlight (Manjhi and Kumar, 2019a) are the various methods reported in the

literature. Conduction-based calibration techniques are also performed by few researchers (Kumar et al., 2012).

1.6.3 Application of the probe in transient flow environments

Fast response characteristic is one of the key highlights of the coaxial thermal probe. Therefore, these probes are mostly preferred for short-duration experiments as in ground-based aerodynamic experiments like shock tubes and shock tunnels. Many authors have used it in shock tunnels along with thin-film gauges. These probes are mounted on the aerodynamic models at specific locations, and the transient temperature is noted. The thin-film gauges are unable to withstand the rough conditions of the hypersonic flow at locations around the aerodynamic model where high heat fluxes are generated. Therefore, the thin film gauges are used at some specific locations on the model where the heat fluxes are relatively low, and flow conditions are not too severe. Thermal probes are usually preferred at locations on the model where there is a probability of high heat flux, such as stagnation points, re-attachment points after flow separation, etc. The coaxial probes are therefore preferred at locations of high heat flux. Sometimes, combined sensors are used for accurate capture of the flow phenomena, i.e., to capture low heat flux thin film gauges, and for high heat flux, coaxial probes are used (Olivier et al., 1995). These probes are used in the test section and at the end flange of the shock tubes to capture the high-speed flow phenomena, (Agarwal, 2018; Mohammed et al., 2010b). The incoming shock wave (generated at the interface of the driver and driven section of the shock tube) is well captured by these probes in the shock tubes. The response time of these probes is found in the order of a few micro seconds (Desikan et al., 2016; Olivier et al., 1995).

Apart from the aerodynamic experiments, these probes are used in various other applications to capture the transient temperature. One such example is in the combustion chamber of an internal combustion engine. These probes were placed on the head of a combustion chamber of a divided chamber diesel engine, and the transient response was captured by Alkidas and Cole (Alkidas and Cole, 1985). The temperature variation was captured against the crank angle. Some similar work was also carried out by some other researchers (Mavropoulos et

al., 2009). These probes were also used in gas turbine engines to capture the screech phenomena (Agarwal, 2018).

1.6.4 Numerical simulation of the probe

With the advancement of computing facility, the thermal sensors are simulated as a whole in 3D or in 2D for different categories of heat loads, and the information is quite useful to justify the assumptions considered during analytical modeling. A very interesting simulation work is performed to find out the effect of junction depth on the heat transfer behavior of the coaxial probe fabricated using the abrasion technique (Li et al., 2017). Here, the sensor is assumed as having the similar design as shown in **Fig. 1.9**. The surface junction is modelled as a circular ring with a rectangular cross-section located on the insulation layer. A 2D unsteady heat conduction equation is applied to model the heat conduction process inside the probe. The equation is solved by the finite difference method for spatial discretization, and the fourth-order Runge-Kutta method is used for time integration. The results are plotted in terms of Fourier number. The simulations are carried out by different researchers using commercially available packages (e.g., ANSYS), with finite element method (Kumar and Sahoo, 2013), and transient thermal module (Agarwal, 2018). In these simulations, time-temperature or a time-heat flux history is provided as input to obtain the time-heat flux or time-temperature values, respectively. In all the cases, the sensors are considered as having adiabatic outer wall with a constant temperature bottom. The results obtained are having a nice match with the analytical results.

1.6.5 Heat flux recovery techniques for short duration experiments

The estimation of surface heat flux from the temperature history, especially for short-duration experiments, is a tedious task owing to the unsteadiness of the temperature signal. Therefore, the sensors are modeled with various simplified assumptions to estimate the heat flux from the temperature value. The analytical method is widely used by the researchers before the widespread of the numerical simulations for estimation of the heat flux. The method used popularly (typically for thin-film gauges and coaxial probes) is by assuming the sensor is sitting on a semi-infinite substrate having one-dimensional heat conduction through

it. This assumption provided a solid framework for the derivation of heat flux from the transient temperature signal. This principle is synoptically evaluated and elaborated in detail in the literature (Schultz and Jones, 1973). The detailed expression for coaxial probe and thin-film gauge is elaborated in Chapter 2. Many authors are still using the analytical expression for the estimation of heat flux. There are many correlations developed for heat flux estimation, especially for shock tunnel applications (Fay and Riddell, 1958). Afterwards, the numerical simulations are being performed widely by many authors to validate the analytical results. Nowadays, even more sophisticated methods involving data science and soft computing tools are in use for such estimations; however, implementation of these tools is in a preliminary stage. Therefore, the implementation of such a tool is one of the intentions of this thesis work.

1.7 Summary of literature review

From the literature review in the various aspects of the intended research work, it can be concluded that there are various areas that need more in-depth study and special attention. The outcomes of the literature studied can be summarized as follows:

- Research work related to surface junction thermocouples (mainly coaxial thermal probes) has been carried out for the study of heat flux measurement and instantaneous temperature measurement. An appreciable amount of study has not been done to declare the sensor as a heat flux sensor.
- The principle of heat flux assessment is still based on the conventional technique (heat flux on a semi-infinite solid) using simplified models and various approximations.
- The thermal product ($\rho ck-$value), which is essential for the determination of heat-flux from the obtained temperature-time history, has much not been focused on.
- A proper heat flux calibration approach has not been reported in the literature.
- The CTPs have been applied to moderate temperature applications but not to any high-temperature applications.

- Hence, to suggest surface junction thermocouples as potential device, there is still the requirement of further study in different aspects.

1.8 Framework of research and objective of the thesis

Considering the literature gap in various aspects of the present research work, it can be concluded that multiple areas need more in-depth study and special attention. The recovery technique of surface heat flux for short-duration experiments mainly rely on conventional methods. With the development of the artificial intelligence technique, the heat flux estimation technique can be well framed based on the soft-computing approach. In this regard, the objective of the present work is to implement **a novel soft-computing strategy for heat flux assessment in short-duration measurements.** The method is well supported through experiments, analytical methods, and numerical assessment techniques. In this regard, the transient temperature data are used to estimate the heat flux through the conventional analytical method, and it is validated with the heat flux value obtained from numerical simulation. In the end, a novel approach for heat flux assessment is proposed here using the soft computing technique. To accomplish the objective, the entire work is divided into a few subtasks, which are explained below.

- **Design and fabrication of coaxial thermal probe on a laboratory scale**

  The focus of the present sub-task is to design and study the effect of heat penetration into the sensor and the selection of an appropriate dimension of the sensor for the intended time scale of study. In addition, the sensor is fabricated in-house on a laboratory scale using the selected dimensions.

- **Mechanical characterization of the coaxial thermal probe**

  The constituent element percentage and the junction thickness play an essential role in the sensitivity and response time of the sensor, respectively. Therefore, a study is carried out for the CTP using energy dispersive x-ray spectroscopy (EDX) and field emission scanning electron microscopy (FESEM). This process not only gives an idea about the junction quality but also about the sensing surface composition after the

junction formation, which ultimately helps in getting an idea about the thermal product of the sensor.

- **Determination of sensor thermal parameters through calibration**

  The output of the thermocouple is obtained in terms of voltage. Therefore, sensitivity acts as a linked parameter between voltage and temperature. Along with this, the experimental determination of thermal product values is also an inherent requirement for heat flux estimation. Therefore, these values are obtained through the calibration process. Apart from this, the heat flux values need to be calibrated against a known heat flux source which is performed with the help of a laser heating.

- **Real time implementation of CTP for step and cyclic heat loads.**

  Due to the fast response characteristics of the CTP, it is exposed to a step heat load generated in a shock tube by putting the sensor at various locations in the shock tube. In this process, the response of the sensor towards high-speed flows can be observed from the recorded transient temperature signal. Apart from this, the response characteristics are compared with an in-house fabricated silver thin film gauge and with the pressure transducer. Similarly, the temperature response is captured for a cyclic heat load by mounting these sensors in an internal combustion engine exhaust.

- **Heat flux assessment using soft computing technique.**

  The transient temperature obtained from the shock tube experiment is post-processed to assess heat flux. The one-dimensional heat conduction onto a semi-infinite substrate is the basis for the conventional heat flux analysis of the CTP. Numerical simulations are carried out along with the analytical method to estimate the heat flux values. A hybrid soft computing technique, Adaptive neuro-fuzzy inference system (ANFIS), is also exercised for heat flux estimation.

The sequential approach of the entire thesis work is presented in the form of a flow chart, as shown in **Fig. 1.14**.

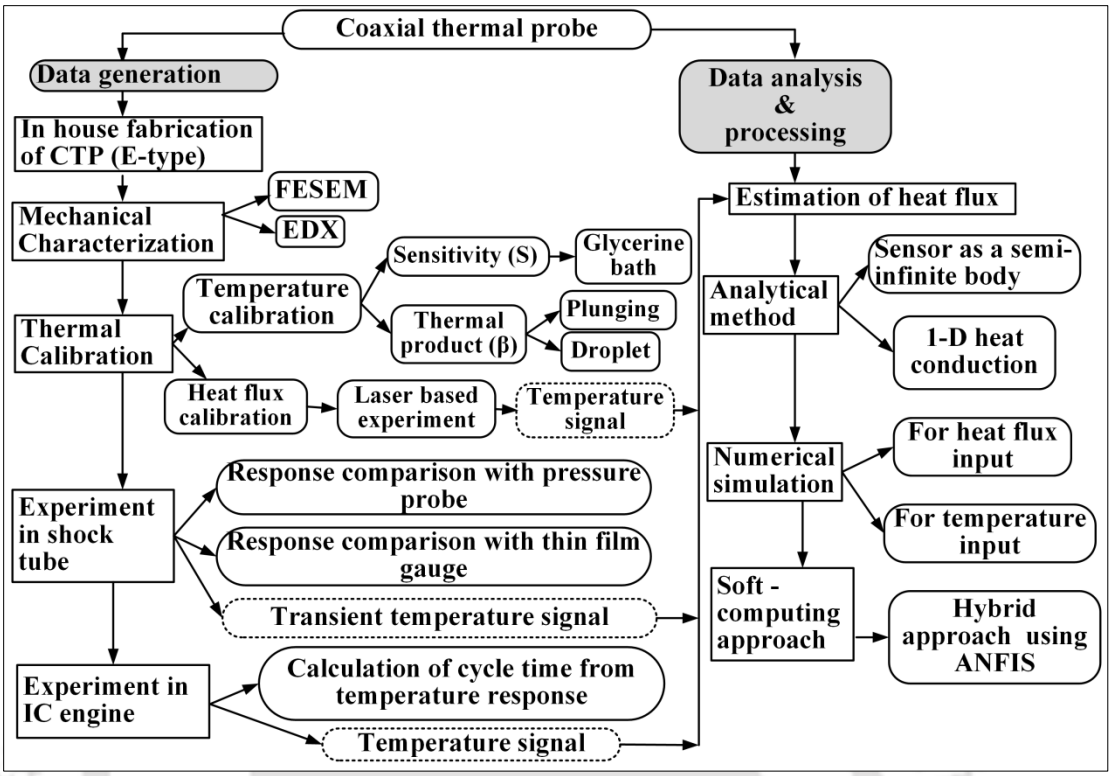

Fig. 1.14: Flow chart highlighting the overview of thesis work.

1.9 Delineation of the thesis work

The primary focus of the present thesis work is to understand the basic working philosophy of calorimetric heat flux probes with an aim to design and fabricate the coaxial thermal probe in the laboratory scale. Further, the idea is extended towards a cost-effective fabrication method to capture the high-speed flow in a shock tube. The fast response characteristic of the probe is tested in a shock tube and internal combustion engine. Subsequently, various heat flux assessment techniques have been employed for short-duration transient flow conditions, and implementation of a soft computing approach is proposed herein.

The sequential activities for the present thesis work are elaborated in the subsequent chapters. After the introduction and a brief literature review in Chapter 1, the mathematical modeling aspects of the probe are presented in Chapter 2, which describes the recovery techniques of the heat flux by analytical method and numerical simulations. The detailed fabrication technique and mechanical characterization of the sensor materials are elaborated in C***hapter***

3. Different sensor parameters are obtained after suitable static and dynamic calibration of the sensor. The aspects of temperature calibration and heat flux calibration using laser sources are highlighted in ***Chapter 4.*** After passing through the phase of fabrication, characterization, and calibration, the sensors are ready for real-time applications. ***Chapter 5*** then deals with the applications of the sensors in a "shock tube" for high-speed flow diagnostics during short-duration flow conditions. The chapter also includes the evaluated "surface heat flux" under this harsh flow condition. ***Chapter 6*** deals with the extended application of the sensors for internal combustion engines. Apart from conventional analytical heat flux recovery and the present numerical simulations, novel soft computing method (ANFIS) is also adopted for heat flux recovery in case of short duration flows which is elaborated in ***Chapter 7.*** The concluding views about the present investigation and the possible future extension of the study are placed in ***Chapter 8***.

CHAPTER 2

Design and modeling aspects of thermal probe

Overview

A brief introduction about the progress of the research carried out till date, in the field of heat flux recovery (for short duration experiments) has been elaborated in the previous chapter. The objective of the current work has also been explained in detail. The important objective of the present work is to estimate the heat flux in short-duration transient flow conditions with the help of various estimation methods. The temperature signal is the inherent ingredient for the estimation of heat flux. To fulfill the objectives, the fabrication of a fast response thermal sensor is the initial requirement for which pre-planning of the entire process is essential to get an idea about the intended task. Therefore, before carrying out the fabrication, the dimensions and the materials of the sensor need to be finalized. The dimensions can only be finalized after evaluating the heat transfer phenomena through the sensor. Hence, modeling and fundamental heat transfer analysis of the sensor is carried out with proposed dimensions considering the information from literature and suitability of fabrication. Transient temperature value mainly deals with the material properties of the sensor along with the time scale of application. To capture the time-temperature history and hence heat flux, the sensor dimensions and design are as crucial as other parameters. Depth of heat penetration into these probes plays a vital role in determining the magnitude of heat flux and its distribution. Hence, the thermal modeling aspects of such sensors have been analyzed in this chapter by assuming them having a semi-infinite substrate with one-dimensional heat conduction. The one-dimensional heat conduction equation has been solved with appropriate boundary conditions and assumptions to reach the final form. Similarly, numerical simulations have been carried out to find out the effect of thermal penetration and lateral heat conduction. The analysis has been carried out using a commercial solver (Ansys), imitating a near realistic model of the sensor. The results have been expressed in terms of Fourier number and through contour plots.

2.1 Introduction

As inferred from Chapter 1, different sensors have some advantages and limitations corresponding to the specific flow measurements. For the heat flux recovery, in the case of short duration experiments, the preferred probes are “coaxial thermal probes (CTPs)” and "thin-film gauges (TFGs).” Both the probes fall under the category of “calorimetric heat transfer gauge,” where the measuring parameter is the change in temperature over a time interval. Therefore, these gauges are the simplest to work with. In fact, a temperature-time history is often preferred for heat flux recovery. The transient temperature value is a function of the material properties of the sensor and the time scale of application. Therefore, sensor dimensions, sensor design has a direct impact on heat flux estimation. In fact, the depth of penetration of heat along the length of the sensor and lateral heat conduction over time plays a vital role in the accuracy of the magnitude of heat flux and its distribution. Hence, prior to the fabrication of the sensor, the heat transfer analysis of the sensor is required to get an insight into the transient behavior of the sensor.

A numerical analysis has been performed by taking a suitable sensor dimension. The choice of dimension is based on the available data in the open literature, the theoretical concept of semi-infinite body, and the possibility of the sensor fabrication on a laboratory scale. The effect of heat transfer along the length and in the lateral direction is studied. With the advancement of computational technology, a commercial software package, ANSYS-14.5 has been used for the study. The study is also intended to verify the semi-infinite body assumption for the sensor, which is the basic idea behind the analytical modeling of the sensor. It is carried out by solving the one-dimensional heat conduction equation for the sensor by assuming it is a semi-infinite body. These assumptions help to find a simplified solution for the differential equations. All these analyses are then implemented to justify the sensor dimension and proceed with the fabrication. The detailed process of numerical simulation and analytical modeling is described in the subsequent sections.

2.2 Numerical simulation

One of the intentions of the present research is to explore the usage of an E-type (Chromel-constantan) surface junction thermal probe as a heat flux sensor for short-duration experiments. The numerical simulation will help to get an idea about the thermal response corresponding to different heat loads. In the present era of computational advancement, a standard commercial solver (ANSYS 14.5) has been chosen to support the fact. The numerical simulation requires the sensor dimensions, boundary conditions, and the governing equations to be solved. The sensor dimensions are finalized by considering a few facts such as; the available data from open literature to have a justification for the semi-infinite method and the feasibility in laboratory-scale fabrication. As mentioned previously, these sensors fall in the category of calorimetric thermocouples, preferably find application in short-duration experiments due to fast response time. Unlike conventional types of thermocouples, having a volumetric contact, the design features of CTPs differ in terms of miniature type surface-contact between thermo-elements (Mohammed et al., 2010b). They are often fabricated by inserting one thermo-element of the thermocouple into the other's annulus concentrically. While restoring the coaxial nature of thermo-elements, a thin layer of insulation separates both the elements except at the sensing surface, where the contact thickness between the elements is about a few microns. This bridge element thickness has a significant effect towards response time of the sensors and falls in the range of 10-30 μm (Chapter 3).

One of the primary aspects of the present investigation is to fabricate a coaxial surface junction thermal probe (E-type) in laboratory scale for its usages in a shock tube for short duration measurements. Depending on the strength of the primary and reflected shock, the magnitude of step heat flux (in the range of 1.5 to 2 MW/m^2) of induced flow can vary (Mohammed et al., 2008). The maximum time scale of experiments to capture the complete events of primary and reflected shock is 20 ms. In the subsequent discussions of calibration experiments, the probe needs exposure for similar nature of heat load within 20 ms duration. With this viewpoint, the intended exercise is to study response behavior and effects of the insulation layer on the transient characteristics of the CTP through numerical simulation.

Essentially, one can arrive at suitable dimensions for each thermo-element along with insulating material for an E-type probe towards its precise fabrication.

The thermal properties values between the thermo-elements (Chromel and Constantan) of an E-type CTP are very close that helps in minimizing lateral heat conduction. The geometrical configuration of CTP is shown in **Fig. 2.1**. It consists of an inner constantan wire of 0.91 mm diameter placed in the chromel annulus of outer diameter 3.25 mm, which are electrically insulated from each other by epoxy in the axial direction (along the length). The insulation gap or the thickness of epoxy is approximately 20 μm. During the preparation of the sensing surface, a bridging junction between the two thermo-elements is often created externally to the thermo-elements of the CTP. In this formation process, the junction is located in the vicinity of the insulation layer and sometimes on the insulation layer. The importance of the junction location can be attributed to the point of heat dislocation, i.e., with the application of heat load on the sensing surface, lateral heat conduction will certainly take place near the junction due to huge differences in the thermal properties of the epoxy and the thermo-elements. However, the structure of the junction is uncertain and uncontrollable. Therefore, simplified assumptions are usually made for the simulation where a uniform sensing surface external to CTP is shown as the top surface (**Fig. 2.1**).

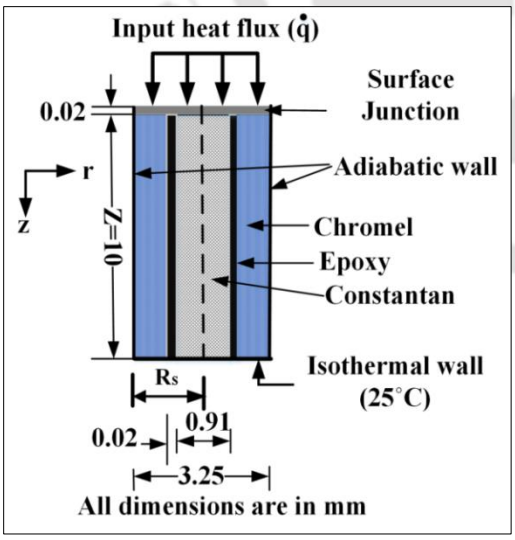

Fig. 2.1: Computational domain of CTP for numerical simulation with heat flux as step load on the sensing surface

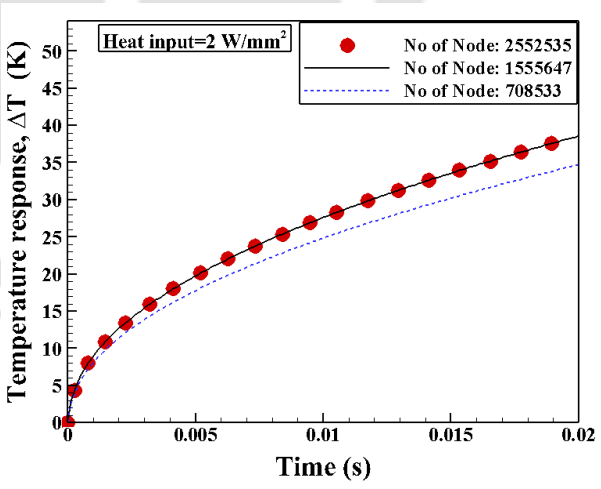

Fig. 2.2: Grid independent study through transient response.

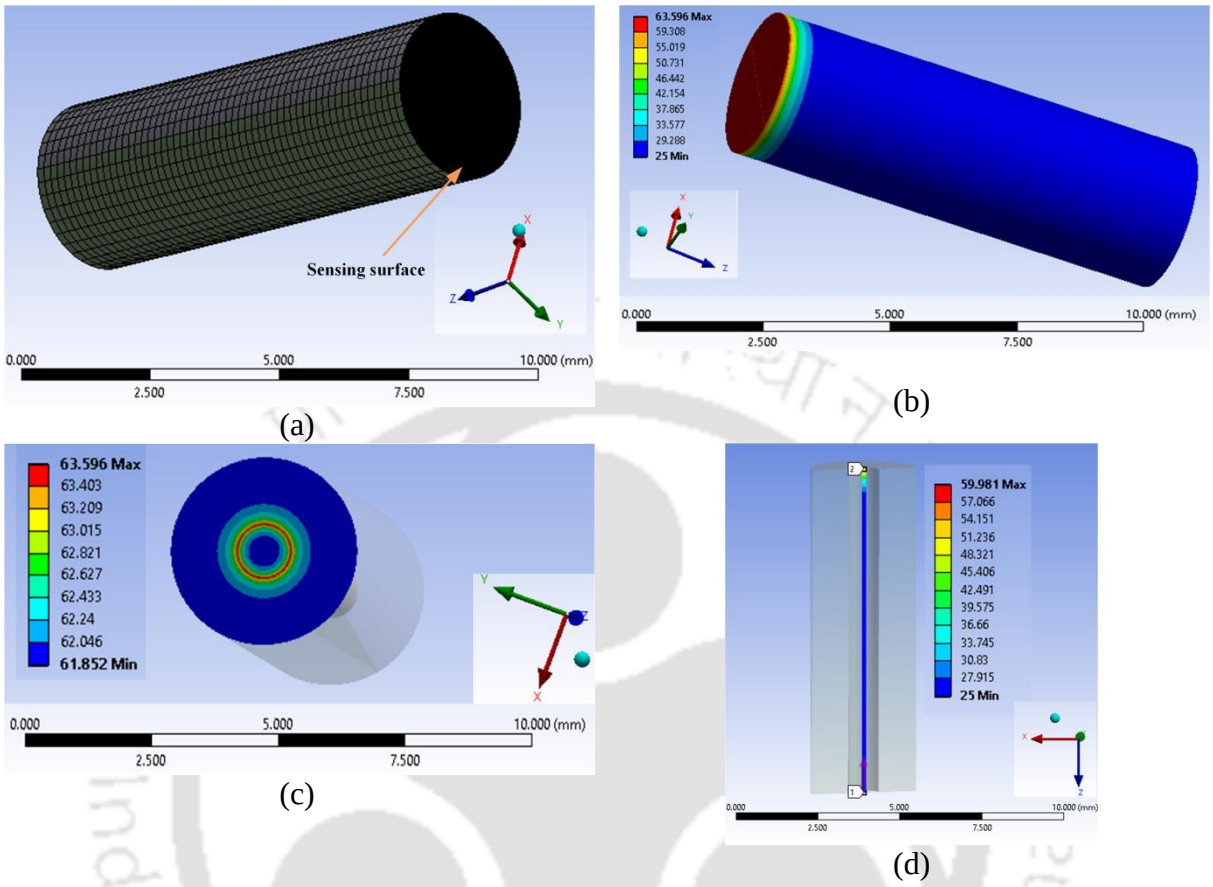

Fig. 2.3: Computational Results for 20ms simulation with 2W step heat load; (a) computational domain mesh structure, (b) Body temperature contour, (c) Sensing surface temperature contour, (d) temperature distribution along the depth

The computational domain for numerical simulation (**Fig. 2.1**) has the schematic of the sensor along with boundary conditions. The thermal properties of materials of (chromel, constantan, and epoxy) are mentioned in **Table 2.1**. The domain has an additional thin layer of material (0.02 mm) that pretends to be the sensing surface for exposure of heat load. The modeling of this surface bears the average property of chromel and constantan by neglecting the effect of epoxy material, as its thickness is minimal compared to thermo-elements. The transient thermal module of the ANSYS solver is used for the entire simulation for a period of 20 ms. A grid independent study has been carried out to check the mesh dependency using three different combinations of nodes (708533, 1555647 and 2552535). The surface temperature history obtained for an arbitrary step heat load of 2 MW/m^2 shows consistent

results for later two combinations of nodes (**Fig. 2.2**). In order to minimize computational time, less no of nodes are selected for the simulation for all subsequent computational studies (Anderson and Wendt, 1995). The simulation results are presented with the help of contour plots (**Fig. 2.3**).

Influence of insulation thickness

The results obtained from the numerical simulations of CTP for a constant heat flux input imply the critical heat conduction process on the sensing surface. It is essential to have negligible heat penetration into the substrate during test duration so that measured data on the sensing surface replicate exactly the surface temperature. Considering the construction feature of the CTP, it may be noted that the insulation material is below the sensing junction. In this context, the transient heat conduction, governed by a non-dimensional parameter, i.e., Fourier number, (F_o) is introduced to evaluate the response behavior of CTP and heat penetration effect during test time (t) (Li et al., 2017). Defining average thermal diffusivity of thermo-elements (chromel and constantan) as α_{av} and insulation thickness as characteristics length (b), the F_o can be expressed by Eq. (2.1).

$$F_o = \frac{t\,\alpha_{av}}{b^2} \tag{2.1}$$

The simulation results for different time scales (in the range of 0.1 ms to 20 ms) are presented in terms of Fourier number in **Fig. 2.4**. The highlighting features are the temperature distribution near the junction on the top surface of the CTP and temperature distribution inside the probe. The result of isotherms along the lateral direction is almost uniform except at the sensing junction which is created above the insulation so that heat does not penetrate into the substrate. During the test time period of 0.1 ms to 20 ms, there is a significant deviation of temperature across the sensing junction with respect to other locations on the surface. This deviation in surface temperature is observed to be increasing for a higher time scale. Quantitatively, at $F_0 = 1.37$ (test time of 0.1 ms), the maximum rise in

temperature (ΔT) across the insulation thickness is about 0.14 K, while at $F_0 = 274$ (test time 20 ms), the rise in ΔT is about 1.64 K. In other words, for a given insulation thickness (20 µm in this case), the temperature gradient $\left(\frac{\Delta T}{\Delta t}\right)$ across the insulation decreases continuously for an increase in simulation time and Fourier number. The reason for this phenomenon is the low thermal conductivity of the insulation layer and the heat penetration along the depth of CTP. In the small time scale (0.1 ms - 20 ms) study, the penetration of heat into the CTP is lower, thus allowing more heat from the free stream flows to be concentrated near the sensing surface. These facts imply that during small time scales of the experiment (0.1 ms to 20 ms), there will be the presence of significant lateral temperature gradient and the occurrence of lateral heat conduction around the junction (**Fig. 2.4**). Therefore, the insulation thickness has a great influence on the heat transfer process in the case of short duration studies; small insulation thickness is preferred to capture accurate surface temperature rate and hence subsequent computation of heat flux histories. Based on the above-mentioned facts, insulation thickness of 20 µm is preferred considering a laboratory-scale fabrication approach for CTP. The heat transfer effect is elaborately studied for a time scale of 20 ms $(F_o = 274)$ duration by considering the practical experimental usage of the probe in a shock tube. However, the actual sensing time by the CTP in the real flow event is even less than 1 ms. Nevertheless, the experimental challenge of in the shock tube is to capture flow phenomena involving incident and reflected shock through CTP.

Like insulation thickness, the penetration of heat inside the CTP also affects the sensing surface response parameters, especially during short-duration surface heat flux studies. For this purpose, the simulation time of 20 ms $(F_o = 274)$ is considered to study the heat penetration effects. It may be noted that the heating effect is felt up to 1.4 mm depth from the sensing surface, measured at the center of the probe (**Fig. 2.5**) beyond which there is no thermal penetration is observed. The probable reasons for these phenomena are different values of thermal diffusivities of the three materials (chromel, constantan and epoxy). The low thermal conductivity restricts the heat penetration along the depth of the probe, and different thermal diffusivities of the materials impart localized conduction speed to the

thermal probe. Therefore, thermo-element materials with nearly similar properties are the ideal choice as they can provide a better response to CTP. In short, these types of complex heat conduction processes within the thermal probe certainly influence the temporal changes of the junction temperature which ultimately have an impact on the surface heat flux values.

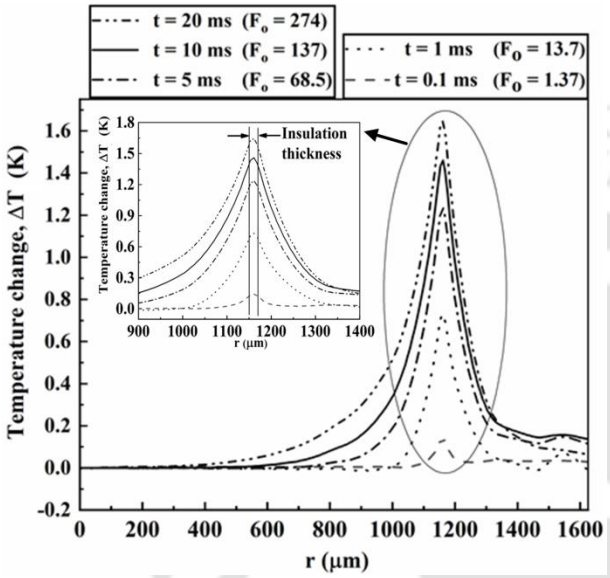

Fig. 2.4: Temperature change across the radial direction of the probe at a different time scale of the simulation.

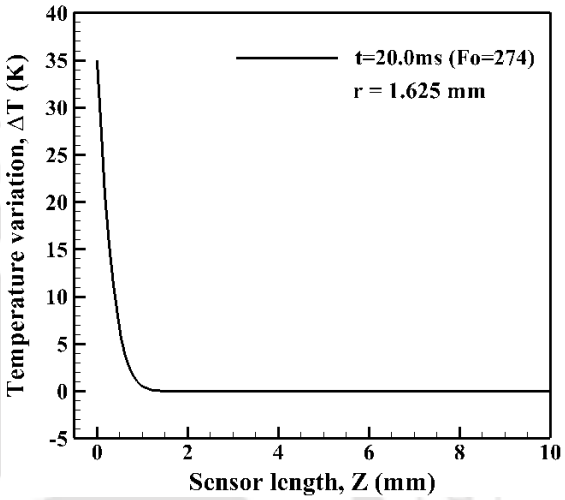

Fig. 2.5: Heat penetration along the depth of the probe.

2.3 Heat flux modeling for CTP

The present discussion about the analytical method primarily focuses on the one-dimensional analysis of heat transfer gauges under consideration, i.e., thin-film gauges and coaxial thermal probes. As mentioned previously, most of the short duration measurements rely on surface temperature histories for the heat flux assessment. They are obtained either directly from experimental measurements or from numerical methods. Subsequently, the surface heat flux is obtained through appropriate one-dimensional modeling of the sensor using the basic concept such as semi-infinite principle, thin-film, or thick film gages (Taler, 1996).

For a thin-film gauge, the sensor is a platinum, nickel, silver, or palladium film, and the substrate is a thermally insulative material such as Macor or Quartz. For a coaxial thermal probe, the sensing element is a thin junction joining the two constituting thermo-elements of

thermocouple (such as chromel and constantan), while the substrate is the body of the thermocouple. In both cases, the sensor is typically designed so that the thickness of the sensing element is much less than that of the substrate (Hollis, 1995). Therefore, the sensing element has a negligible effect on the heat transfer to the substrate, and the temperature measured by the sensing element is identical to the temperature at the surface of the substrate. It is also assumed that there is negligible conduction in the lateral direction of the substrate rather; heat is conducted only in the direction normal to the sensing surface. The final assumptions are that the substrate has an infinite depth and that the temperature rise at infinity is zero. These combined assumptions are referred to as the "one-dimensional, semi-infinite solid model." Using this model, the temperature distribution in the substrate can be given by the partial differential equation as in Eq. 2.2.

$$\frac{\partial}{\partial x}\left(k\frac{dT}{dx}\right)=\rho c_p\frac{\partial T}{\partial t} \tag{2.2}$$

The thermal properties (thermal conductivity, specific heat, and density) are all functions of temperature. For some materials, such as the metals in a coaxial thermocouple, the thermal conductivity increases rapidly with temperature, but the thermal diffusivity increases only slightly. For insulative materials such as Macor and quartz, which are used as substrates for thin-film gages, the temperature has a strong effect on both the thermal conductivity and the thermal diffusivity. However, for a small test time duration, these properties can be assumed to be invariant. A common simplification is the assumption of constant thermal properties, in which case the temperature distribution is given in Eq. 2.3 (Hollis, 1995; Schultz and Jones, 1973).

$$\frac{\partial^2 T}{\partial z^2}=\frac{1}{\alpha}\frac{\partial T}{\partial t} \tag{2.3}$$

Here, $T(t)$ is the measured transient temperature, z is co-ordinate along the depth the substrate and α is thermal diffusivity of the substrate. It may be noted here that, in the case of thin-film gauges, a thin metallic film (medium-I) is deposited on the surface of an insulating substrate (medium-II).

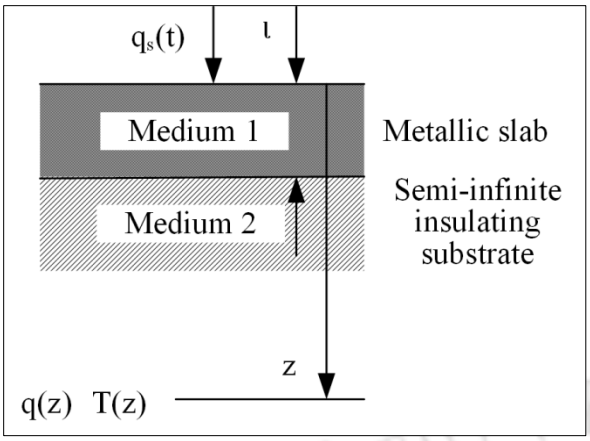

Fig. 2. 6: Schematic of one-dimensional heat conduction model for TFG

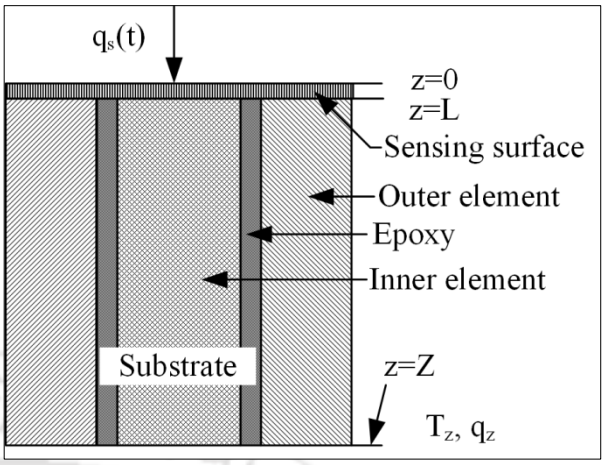

Fig. 2. 7: Schematic of one-dimensional heat conduction model for CTP.

For a particular step function heat transfer as input the differential equation for the two media can be represented as

$$\frac{\partial^2 T_1}{\partial z^2} = \left(\frac{\rho_1 c_1}{k_1}\right)\frac{\partial T_1}{\partial t} \tag{2.4}$$

$$\frac{\partial^2 T_2}{\partial z^2} = \left(\frac{\rho_2 c_2}{k_2}\right)\frac{\partial T_2}{\partial t} \tag{2.5}$$

The suffix 1 and 2 in Eq. (2.4) and Eq. (2.5) depicts the sensing surface and the substrate material of the heat flux gauges. Temperature is T at a distance z from the surface at a time "t". If a heat load $q_S(t)$ is applied instantly, the transient temperature of the CTP will be $T_S(t)$. Therefore, referring to **Fig. 2. 6** and **Fig. 2. 7**, initial and boundary conditions can be written as follows:

Initial conditions: $T(z,0) = T_o$

At $z = 0$: $\dot{q}(0,t) = \dot{q}_S(t)$

At the interface between region 1 and 2 (i.e., at $z = Z_1$) $\dot{q}_{s1} = \dot{q}_{s2}$ *and* $T_1 = T_2 = T_s(t)$ (2.6)

$$\text{At } z = Z_2 \ : T_2 = T_o$$

Applying the boundary conditions to Eq. 2.4 and 2.5 and incorporating a few assumptions ($Z_1 \to 0$ and constant thermal properties of the substrate), the heat flux $\dot{q}_S(t)$ can be obtained in a combined form using Duhamel's superposition integral as given in Eq. 2.7 (Schultz and Jones, 1973; Taler, 1996).

$$\dot{q}_S(t) = \frac{\beta}{\sqrt{\pi}} \int_0^t \frac{1}{\sqrt{t-\tau}} \frac{d\{T_s(\tau)\}}{dt} d\tau \ ; \ \beta = \sqrt{\rho c k} \tag{2.7}$$

This is the general solution to this type of heat conduction problem. Various methodologies have been adopted by different researchers for data reduction from this equation. For further analysis to obtain a closed-form solution numerically as well as using some conventional techniques this equation is not a suitable form (Schultz and Jones, 1973). Because, in this form, the differential of the surface temperature and the presence of noise will make it difficult to execute. This form is then simplified by integrating it with the help of by parts technique to arrive at a form as given in Eq.2.8 (Mohammed et al., 2008).

$$\dot{q}_s(t) = \frac{\beta}{\sqrt{\pi}} \left[\frac{T_s(t) - T_o}{\sqrt{t}} + \frac{1}{2} \int_0^t \frac{T_s(t) - T(\tau)}{(t-\tau)^{0.5}} d\tau \right]; \beta = \sqrt{\rho c k} \tag{2.8}$$

2.3.1 Test time and semi-infinite assumption

The semi-infinite substrate assumption, which is required for an analytical solution of Eq. 2.2 is only approximately correct during an actual experiment. The accuracy of the assumption is a function of material depth, diffusivity, and test duration and can be measured in terms of the increase in the temperature or heat transfer rate at the back of the substrate. The effect of penetration depth is widely elaborated by taking a dimensionless penetration depth $Z^* = \frac{Z}{\sqrt{4\alpha t}}$. Expression for the back face heat transfer and temperature for a constant heating

rate was also derived in the literature (Schultz and Jones, 1973). The period of semi-infinite test time can be estimated as a function of the thickness of the substrate. Ideally, the substrate should be thick enough that the ratio $\left(\frac{\dot{q}_Z}{\dot{q}_s}\right)$ at the back face of the substrate be no more than a few percent for the desired test time. As an estimate, considering a 1% change, some standard value can be obtained, i.e., when the ratio of $\frac{T_Z}{T_s} = 0.01, Z^* = 1.58$ and when the ratio of $\frac{\dot{q}_Z}{\dot{q}_s} = 0.01, Z^* = 1.87$. Because the penetration depth is inversely proportional to the square root of diffusivity, a material with lower diffusivity (such as ceramics) has a longer semi-infinite test time, whereas high diffusivity materials (such as metals) have shorter test time. It may be noted that the penetration depth is often interpreted as $\sqrt{\alpha t}$ which corresponds to $Z^* = 0.5$. But, it can be observed that at this depth, the heat transfer rate is 50% of the surface value, and the temperature is 35% of the surface value when gauges designed on the basis of $Z^* = 0.5$ will ultimately end up losing a huge amount of heat from the rear of the sensitive element. Therefore, to get the temperature and heat flux as 1% of the surface value, the condition should be $Z = 3.16\sqrt{\alpha t}$ and $Z = 3.74\sqrt{\alpha t}$, respectively. After evaluating these criteria for many materials, it has been observed to obey a thumb rule considering heat flux as well as temperature as $Z = 4\sqrt{\alpha t}$. For most metals, this yields $Z\ (cm) = 4\sqrt{t(\sec)}$ and for insulators $Z\ (cm) = 0.3\sqrt{t(\sec)}$ (Schultz and Jones, 1973).

2.3.2 Temperature discretization and heat flux predictions.

The equation of the form as given in Eq. 2.8 is widely used by many researchers as it is more convenient for data analysis. Numerical integration of the second part of the expression will lead to the determination of heat flux values when the heat transfer rate is not constant. However, this form of the equation contains a singularity in the integral term at $t = \tau$ which will induce error in the heat flux estimation. In fact, these errors are larger for a smaller magnitude of $'t'$. Different numerical techniques have been adopted and recommended by many researchers for the minimization or omission of this error. The most popular method

assumes a piecewise linear function for the discretization. The form of equation in which this approximation is applied was in terms of "voltage," not "temperature." If the surface temperature between successive times is assumed to vary linearly with time, then a piece-wise linear function can be assumed for temperature data (Cook and Felderman, 1966).

$$\{T(t)\}_{\text{linear}} = T(t_{i-1}) + \frac{T(t_i) - T(t_{i-1})}{\Delta t}(\tau - t_{i-1}) \qquad (2.9)$$
$$\text{where, } \tau = t_i = i(t/n) = i\,\Delta t; \quad i = 1, 2, 3, \ldots\ldots\ldots, n$$

Here n is the number of temperature data points recorded by the acquisition system during the experiment. The simplified expression for Eq. (2.8) is given as below;

$$\{\dot{q}_s(t)\}_{\text{linear}} = 2\sqrt{\frac{\rho c_p k}{\pi}} \sum_{i=1}^{n} \frac{T(t_i) - T(t_{i-1})}{(t_n - t_i)^{1/2} + (t_n - t_{i-1})^{1/2}} \qquad (2.10)$$

With the advancement of the computational techniques, the polynomial curve fitting came into the limelight, and a polynomial curve fitting approach for this problem was proposed in the literature (Taler, 1996) where the Eq. 2.7 can be directly addressed. As mentioned by previous researchers, amongst various curve fittings, the cubic spline fits the best for the present problem. Polynomial regression data fitting technique can also be applied for transient surface temperature response and is given by the expression,

$$\{T(t)\}_{\text{poly}} = B_0 + B_1 t + B_2 t^2 + B_3 t^3 + B_4 t^4 + .. + B_m t^m = \sum_{i=0}^{m} B_i t^i \qquad (2.11)$$

Here m is the degree of the polynomial considered for constructing the temperature signal. The corresponding surface heat flux obtained from Eq. (2.8) is given by Eq. 2.12 (Sahoo and Peetala, 2010; Sahoo and Peetala, 2011; Taler, 1996). The coefficients $B_0, B_1, B_2 ..... B_m$ for Eq. (2.11) are obtained by regression analysis.

$$\{\dot{q}_s(t)\}_{\text{poly}} = 2\sqrt{\frac{\rho c_p k}{\pi}} \left(\left[B_1 \sqrt{t} + \sum_{i=2}^{m} i B_i t^{(2i-1)/2} \right] \left[1 + (i-1)! \sum_{n=1}^{i-1} \frac{(-1)^n}{(2n+1)n!(i-1-n)!} \right] \right) \qquad (2.12)$$

The polynomial smoothing of temperature data allows the calculation of high-order derivatives but may not reproduce real data points, especially when the time spread of the fitted data is large. However, it can be avoided by using another smoothing technique based on a spline. A third-order spline method is used here to discretize the temperature data (**Fig. 2. 8**). These techniques are used here to obtain the closed form solution of temperature history. Subsequently, transient heat transfer rates are predicted by analytical expressions from Eq. 2.13.

$$\{T(\tau)\}_{\text{spline}} = d_{1,i} + d_{2,i}(\tau-\tau_i) + \frac{1}{2}d_{3,i}(\tau-\tau_i)^2 + \frac{1}{6}d_{4,i}(\tau-\tau_i)^3 \left(\text{For } \tau_i \le \tau \le \tau_{i+1}, i = 1,2,..,J\right) \quad (2.13)$$

The constants appearing in this equation can be determined by the following expressions.

$$d_{1,i} = T_2(\tau_i);\ \ d_{2,i} = T_2{}'(\tau_i);\ \ d_{3,i} = T_2{}''(\tau_i);\ \ d_{4,i} = T_2{}'''(\tau_i); \quad (2.14)$$

The surface heat flux is then estimated for $M = 1,2,....(n-1)$ as,

$$\{\dot{q}_s(t)\}_{\text{spline}} = \left[\begin{array}{l} 2\sqrt{\frac{\rho c_p k}{\pi}}\sum_{i=1}^{J-1}\left\{U_i\left(P_i^{1/2} - R_i^{1/2}\right) - \frac{W_i}{3}\left(X_i{}^{3/2} - Y_i^{3/2}\right) + \frac{a_{4,i}}{10}\left(X_i{}^{5/2} - Y_i^{5/2}\right)\right\} \\ +2\sqrt{\frac{\rho_2 c_2 k_2}{\pi}}\left(U_J X_J{}^{1/2} - \frac{W_J}{3}X_J{}^{3/2} + \frac{a_{4,J}}{10}X_J{}^{5/2}\right) \end{array}\right] \quad (2.15)$$

where,

$$X_i = \tau_{J+1} - \tau_i;\ Y_i = \tau_{J+1} - \tau_{i+1};\ F_i = a_{1,i} + a_{2,i}P_i + \frac{a_{3,i}}{2}P_i^2 + \frac{a_{4,i}}{6}P_i^3$$
$$U_i = \frac{dF_i}{d\tau_{J+1}};\ W_i = \frac{d^2F_i}{d\tau^2{}_{J+1}} \quad (i = 1,2,.....,J) \quad (2.16)$$

As observed from Eq. 2.15, the magnitude of the thermal product is an inherent requirement for heat flux estimation. For TFG, this value is usually considered as the thermal product of the substrate material on which the sensor is placed. However, there is a certain difference in the characteristic feature of the substrates for TFG and CTP. In TFG, the substrate is an insulator whose thermal product value remains almost constant throughout the experiment. Whereas the substrate material for CTP is a conductor; consisting of two thermo-elements clubbed by an insulator. Therefore, in the case of CTP, this value varies for the different time

scales of experimentation owing to the conductive nature of the substrate. In fact, some authors have claimed a variation of 30% in the value of "β"for microsecond experimental scale. Therefore, some authors have considered"β" being the average value of both the thermo-elements (e.g., Chromel and constantan). Sometimes, a calibration experiment is performed to find the range of thermal product values. The simulated temperature signal is processed through analytical approach to find the heat flux value considering the average thermal product value (**Fig. 2.** 9). The result indicates an initial peak, then gradual decay, and a near step response.

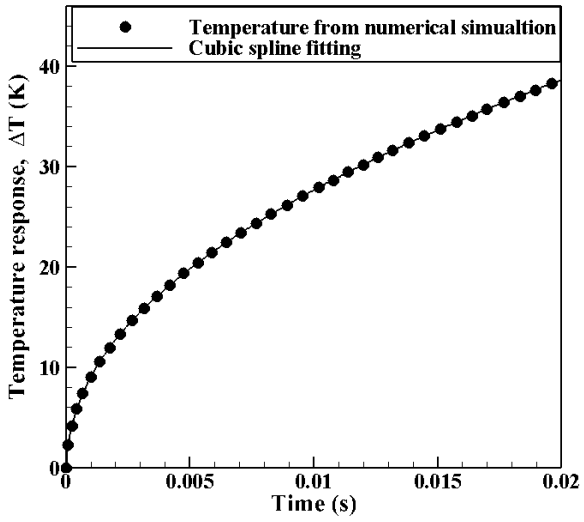

Fig. 2. 8: Cubic spline fitting for the discrete temperature data obtained during experiments.

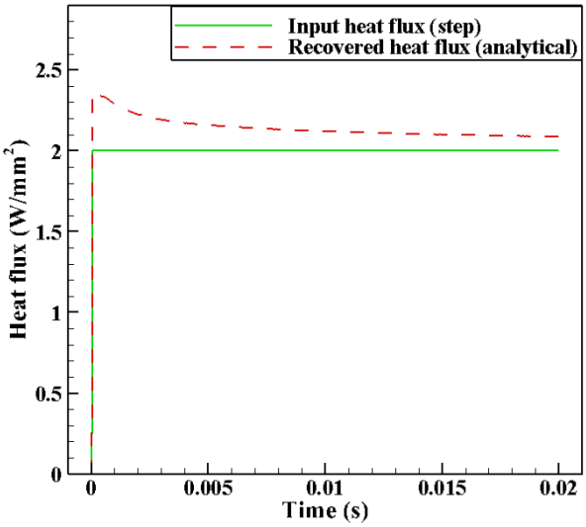

Fig. 2. 9: Analytically heat flux recovery from numerical temperature signal.

2.4 Design of coaxial thermal probe

The design features of CTPs are based on the "calorimetric principle," for which suitable materials are selected with similar thermal properties. Pertaining to current application for its employment, the gauge needs to withstand the hostile environment of shock tube flow. At the same time, it has to capture the transient phenomena across primary and reflected shocks within milliseconds or less. Unlike insulating substrate (as in the case of thin-film gauges), the thermo-elements in CTP are metallic in nature. Hence, it is likely to have heat penetration during the time scale of the experiment. From the representative numerical study (Section 2.2), it is understood that the choice of insulation thickness (20 μm) seems to be appropriate.

Due to the robustness of the sensing element, the CTP will be capable of tolerating a larger transient heat flux (Mohammed et al., 2011). Based on the previous analysis for semi-infinite substrate and considering the data in the literature (Tropea et al., 2007), the time required for complete penetration of heat is about 3 s for a 10 mm long E-type thermal probe. Hence, for the current time scale of the study, the depth of the probe of 10 mm, is sufficient to assume the process of heat conduction as on a semi-infinite substrate. Considering the response characteristics requirement of CTP as discussed in "Section 2.3" and based on the local resource availability, a suitable size of the material is chosen (i.e., chromel wire of 3.25 mm diameter as outer element and constantan wire of 0.91 mm as an inner element) for gauge construction.

2.5 Working principle of CTP

The CTPs work on the basic principle of the Seebeck effect as obeyed by conventional thermocouples, i.e., "flow of current in a metal accompanies the flow of heat." In some metals, the flow of current is in the direction of heat flow (e.g., copper, platinum, Iron, Chromel), whereas, in some other metals, the flow of current is in the opposite direction of heat flow (e.g., constantan, rhodium, alumel). Therefore these two different groups of metals are called dissimilar metals (Warnes, 1994).

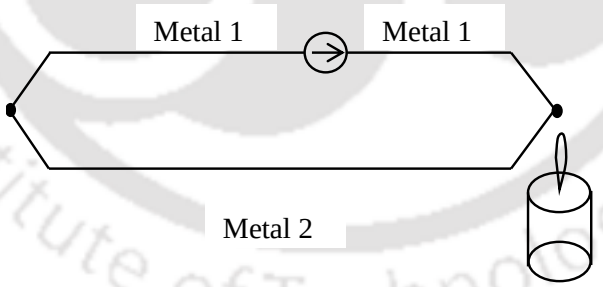

Fig. 2. 10: Basic thermocouple circuit

So, when these dissimilar metals are connected to each other thermocouple is formed (**Fig. 2. 10**). Thermocouples consist of two dissimilar metals joined together at two points, one point being placed where the temperature is to be measured and the other in a known temperature termed as reference junction. When two dissimilar metal wires are joined at both ends, and one end is heated, there is a generation of Electromotive force (EMF). For small changes in

temperature, the Seebeck voltage is linearly proportional to the temperature. Therefore, by measuring the emf, the corresponding temperature can be known. The details about the fabrication process of the probe has been explained in the next chapter.

Table 2.1: Properties of thermocouple materials

Material	Density (kg/m^3)	Specific heat (J/kg/K)	Thermal conductivity (W/m-K)
Chromel	8730	448	19.26
Constantan	8860	393	21.20
Teflon	2250	1400	0.25
Pyrex	2220	775	1.36
Silver	10,490	233	429

CHAPTER 3

Fabrication and mechanical characterization of the coaxial thermal probe

Overview

The detailed modeling of the sensor has been discussed in the previous chapter, that includes the analytical modeling and numerical simulations of the sensor. After getting insight into the sensor and dimensional requirements, it is required to fabricate the sensor, which is one of the primary requirements before conducting any experiment. Therefore, the present chapter is dedicated towards the in-house fabrication of the coaxial thermal probe (CTP) in a laboratory scale and its characterization. The fabrication process deals with the preparation of the outer element, inner element, selection of insulation, and finally clubbing all together to provide a final shape to the probe. The chromel (10mm length and 3.25mm diameter) is taken as the outer element, and a through-hole of 0.95mm diameter is made in it. The constantan (15mm length and 0.91mm diameter) is inserted in the hole coaxially and concentrically with an insulation thickness of 20μm. The insulating material does the combined job of "electrical insulator,"; separating chromel and constantan as well as "binder" for holding both the thermo-elements together. The junction has been created using the abrasion technique, which forms a connection between the thermo-elements through the cold weld and micro scratches. The junction structure is important for the fast response characteristics of the probe. Therefore, the inside and outside surface topography is studied using field emission scanning electron microscope (FESEM), which provides a clear image of the surface. Through this, the conformance about the dimensions considered for fabrication is obtained. Similarly, the composition of the alloys used as thermo-elements plays a major role in the thermal properties of the probe. Therefore, the material constituents are obtained using energy dispersive x-ray spectroscopy (EDX) technique and compared with the ideal material compositions and the material compositions reported by different researchers.

3.1 Introduction

To estimate the surface heat flux, there is a requirement of transient temperature, and to get the transient temperature, an appropriate thermal sensor is required. For the application in shock tube, the coaxial thermal probe has been found suitable for the present case. The method of heat flux recovery has been explained in the previous chapter through analytical modeling by considering the sensor as a semi-infinite body with one-dimensional heat conduction. An independent numerical simulation has also been discussed in the previous chapter, with a special emphasis on insulation thickness, penetration depth, and heat transfer in the lateral direction. The dimensions are selected considering overall sensor design, with an emphasis to fabrication in a laboratory scale from the locally available materials. Chromel being the positive element of an E-type CTP is chosen to serve as an outer element, whereas constantan serves as the inner element with negative polarity. Therefore, the present chapter is devoted to explain the in-house fabrication technique for the fabrication of CTP. A low-cost fabrication method has been adopted here with the help of simple laboratory tools along with abrasion process junction formation. The junction configuration has a direct impact on the response time of the sensor. Therefore, the surface topography is examined using the principle of field emission scanning electron microscopy to get an idea about the actual dimensions. The insulation thickness also has a huge influence on the performance of the sensor, which has to be well within limits (typically less than 30μ) to have a proper junction formation and also fast response. These studies help in confirming the dimensions considered for actual fabrication. Similarly, thermo-element materials are alloys of different elements. If there is a huge deviation in the properties as compared to the ideal composition, then the sensitivity values may be affected along with the differential heat conduction through the sensor. Therefore, the material constituents are obtained using energy dispersive x-ray spectroscopy (EDX) technique and compared with the ideal material compositions and also with the compositions reported in the literature by different researchers. The detailed procedure of fabrication and material characterization using the FESEM and EDX technique is explained in the subsequent sections of this chapter.

3.2. Materials properties of thermo-elements

Before proceeding with the actual fabrication process, it is wise to measure the material composition of the constituent thermo-elements chosen for the fabrication process. This will help in getting an idea about the deviation percentage from the ideal alloy. It may be noted that the thermal diffusivity and thermal conductivity of an alloy depend on the purity of the constituent material in its composition. The E-type thermal probe is a combination of two thermo-elements (chromel and constantan) which are not pure metals rather alloys of two or more elements with varying percentage compositions. The thermal properties e.g., thermal diffusivity thermal conductivity, is the function of the percentage composition of alloying elements. Nickel is the common alloying element for two thermo-elements. Its combination with chromium results in 'chromel' and with copper produces 'constantan'(Roeser and Dahl, 1938). Though nickel is the common alloying element, its percentage varies for both elements. The idealistic composition of these elements does not valid for all the samples produced during the manufacturing process due to the presence of impurities and tracer elements. Therefore, it is necessary to evaluate the composition percentages of alloying elements present in the thermo-elements.

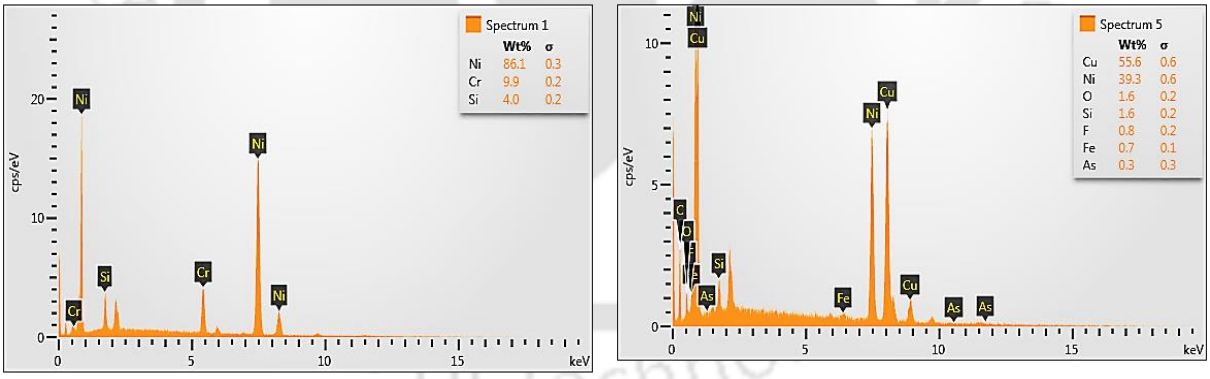

(a) (b)

Fig. 3. 1: EDX spectra of thermo elements for CTP: (a) Chromel: (b) Constantan.

An EDX analysis method is used for the present study, which works on the basic fundamental principle of spectroscopy. Energy dispersive *x*-ray analysis (EDX), referred to as EDS or EDAX; an x-ray technique used to identify the elemental composition of materials. EDX systems are attachments to electron microscopy instruments (e.g., Scanning

electron microscopy (SEM) or transmission electron microscopy (TEM)) instruments where the imaging capability of the microscope identifies the specimen of interest. The data generated by EDX analysis consists of spectra showing peaks corresponding to the elements making up the true composition of the sample being analyzed. The technique can be qualitative, semi-quantitative and also provide the spatial distribution of elements through mapping. The EDX technique is non-destructive, and specimens of interest can be examined in situ with little or no sample preparation.

Table 3.1: EDX spectra and composition of thermo-elements of E-type thermocouple materials.

Thermo elements	Ni %	Cr %	Cu %	Remarks
Chromel	86.1	9.9	----	Based on the data from **Fig. 3. 1**.
Constantan	39.3	----	55.6	
Chromel	90	9.5	----	Reference data (Caldwell, 1962; Touloakian, 1970)
Constantan	45	----	55	
Chromel	90	10	----	Reference data (Mohammed et al., 2008)
Constantan	50	----	50	
Chromel	88	12	----	Reference data (Lawton et al., 1996; Mohammed et al., 2010)
Constantan	55	----	45	

Each element in a material has a unique inter-atomic configuration, which generates a fixed set of peaks on its electromagnetic spectrum. So, by measuring the released energy from these peaks, the element can be identified. The EDX spectra acquired for the thermo-elements (chromel and constantan) are presented in **Fig. 3.** 1. The material composition for chromel and constantan are summarized in **Table 3.1**. The chromel element is composed of nickel (86.1%) as the major contributor, along with chromium (9.9%) and a small amount of

silicon (4%). However, constantan contains nickel (39.3%), copper (55.6) as key alloying element with few trace elements in very less percentage such as Si (1.6%), O_2 (1.6%), F (0.8%), Fe (0.7%) and As (0.3%). Hence, the material used for CTP preparation resembles to have a nearly similar composition with the ideal materials and also have similarity as used by other researchers (Caldwell, 1962; Lawton et al., 1996; Mohammed et al., 2008; Touloakian, 1970).

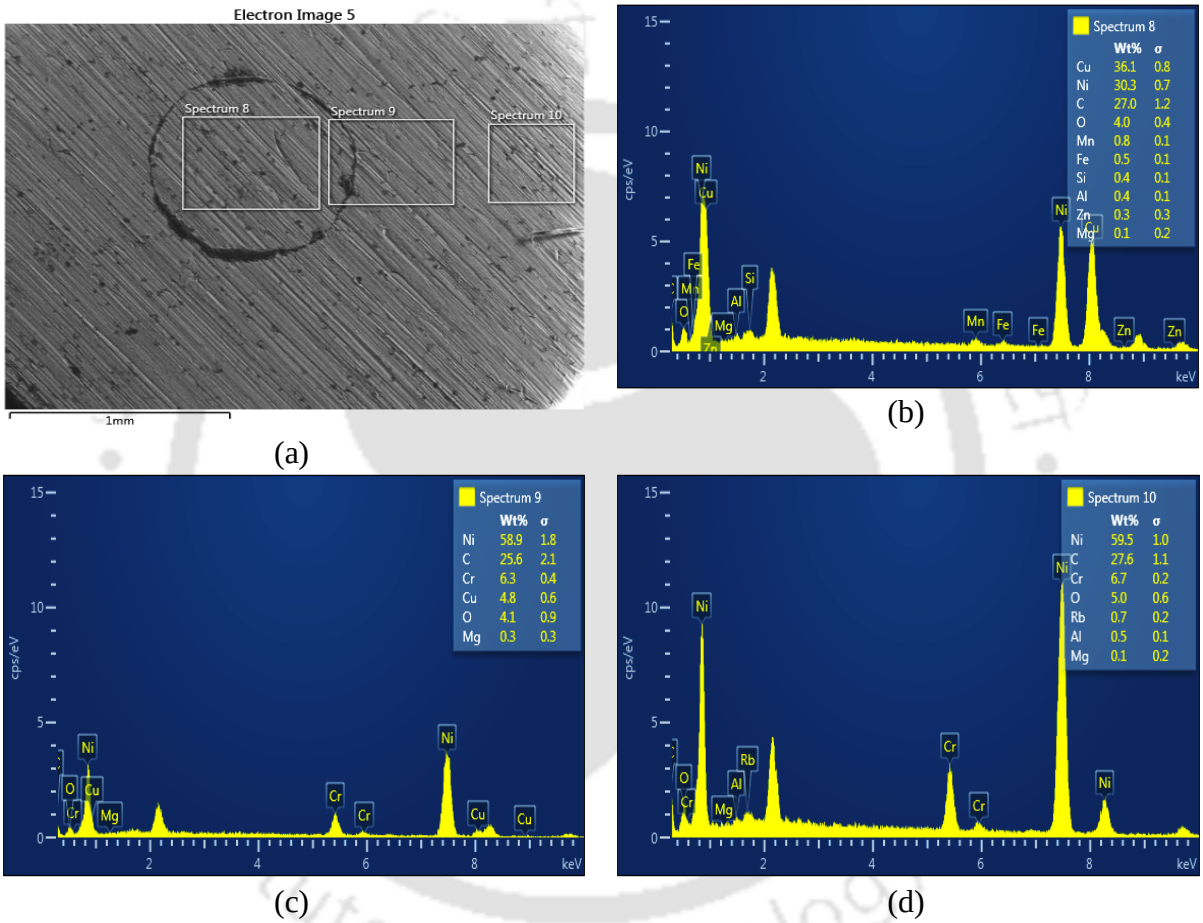

Fig. 3. 2: EDX analysis of E-type sensor at different locations on the sensing surface; (a) locations under study, (b) Spectrum at the inner material location, (c) Spectrum at the junction location, (d) Spectrum at the outer material location.

Similarly, the composition of the sensing surface of the fabricated probe is also obtained using the same method at different locations, viz. on the outer element location, on the inner element location, and on the junction location, to get an estimate about the distributed material composition. As inferred from **Fig. 3.** 2, the material composition on the location of inner material (constantan) is presented in the name as "spectrum 8" has varying material

percentages in comparison to the ideal composition for constantan as given in **Fig. 3.** 1**(b)**. Similarly, the composition at the junction location and on the outer element (chromel) are presented as "spectrum 9" and "spectrum 10" in **Fig. 3.** 2 **(c) & Fig. 3.** 2 **(d),** respectively. The compositions of the elements are not as per the constituent elements. During junction formation, these materials are intermixed and distributed unevenly over the sensor surface. Therefore, it is pretty justified to assume average thermal properties for the thermal product value for the numerical simulations as assumed in Section 2.2.

3.3 Fabrication of coaxial thermal probe

The pre-fabrication process of CTP starts with the selection of materials (thermoelements), the choice of epoxy (insulating material), and the selection of junction formation method. The operating temperature range is predefined for the thermo-elements based on their gauge size, whereas; the actual working temperature for the CTP will depend on the type of insulation used. For example, an E-type thermal probe (chromel-constantan) conveniently measures temperature up to 700ºC. However, if the insulating material (epoxy) has a temperature limit of 200ºC then, the probe can be used for an assured limit of 200ºC; otherwise, there will be a possibility of multiple junctions providing erratic results. Therefore, the selection of epoxy helps to get maximum working temperature decision which is, however, cannot surpass the material temperature limits even if the insulation can resist a higher temperature. For the present case, an E- type (chromel-constantan) thermocouple (CTP) is preferred for transient temperature measurements due to its high sensitivity, called a "thermo-power" sensor. Additionally, due to nearly similar properties of both the thermo-elements, the possibility of lateral deviation is minimized.

The complete fabrication process involves the preparation of outer element, preparation of inner element, assembly of both the element, and junction formation. Bare constantan wire (0.91 mm diameter, 15 mm length) and chromel wire (3.25 mm diameter, 10 mm length) are considered for fabrication of E-type CTP probe (**Fig. 3.** 3 **(a)**). For this probe, the chromel being the outer element, a cylindrical hole (0.95 mm diameter) is drawn by using a micro-drilling machine. The inner element (constantan wire) is inserted into the outer element

concentrically and symmetrically, along with a small insulation thickness in between them. An adequate thickness of epoxy is maintained across its length, leaving the sensing surface unaffected. The epoxy acts as both an electrical insulator and a binder for both the thermo-elements providing strength to the sensor. Due to the small dimensions of the sensor and thermoelements, the fabrication process requires a very precise and careful action, especially during the preparation of the hole and the straightness of the inner element. If not, there is a certain chance of an inner connection between the thermoelements creating multiple junctions. Proper care has been taken to make sure that the inner element is straight, co-axial and there is no connection between the two thermo-elements throughout the length to avoid any possibility of multiple connections. An adequate length of 10 mm of the probe is chosen, which is long enough to become eligible for the assumption of semi-infinite one-dimensional heat conduction modeling (**Fig. 3.** 3 **(b)**).

Formation of sensing junction

The method of junction formation is often carried out with deposition/sputtering techniques which demand high-end equipment. As this work deals with low cost laboratory scale fabrication techniques, an abrasive technique is used here for junction formation. The formation of sensing surface with bondage between these two metallic elements requires precise and skilled operation (Mohammed et al., 2011). A careful and sincere action is essential because of its dimensional constraint, welding requirements, and the need to maintain the required gap for insulation in between the sensor elements. The junction is prepared at the sensing surface with the help of sandpaper (grit size: 180) which creates bondage between the two thermo-elements through micro-scratches and cold welds. The sand-papers of different grit sizes offer additional advantages to provide a smooth and flat sensing surface (Li et al., 2017). The junction is located in the vicinity of the insulation layer and sometimes on the insulation layer. But, the structure of the junction is uncertain and uncontrollable because it appears as an irreversible operation through plastic deformation between thermo-elements. During the process of roughening, the sensing surface contains combined materials from chromel, constantan, and epoxy non-uniformly or in patches. The importance of the junction location can be realized as the point of heat dislocation across

which there is significant temperature gradient during experimental time scale. The junction formed through this abrasion process leads to formation of cold welds between the thermo-elements. For subsequent data recording, similar materials of chromel and constantan wire of (0.25 mm diameter and 2 m long) are spot welded to the sensor that serves as lead wire for measurement. The sensor is packaged in a suitable mounting (threaded with BS4 standards) as shown in (**Fig. 3.** 3 **(c)**).

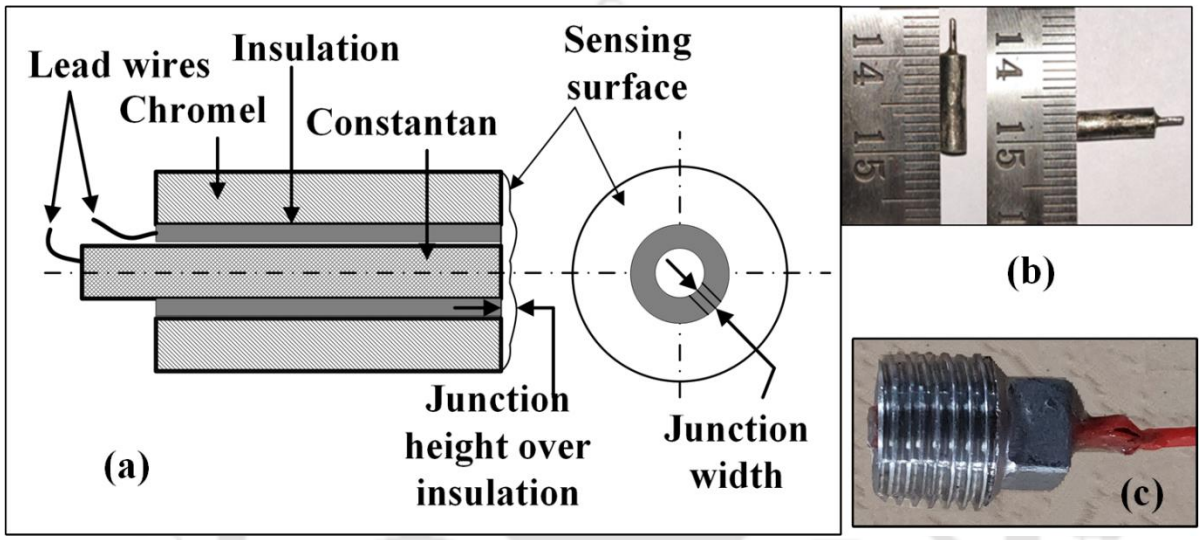

Fig. 3. 3: Realization of CTP: (a) Schematic representation; (b) In-house fabricated sensor; (c) Packaged probe.

3.4 Microstructural analysis

In the process of calorimetric gauge design, the junction thickness plays an important role as the quality of the junction has an impact on the response behavior of the sensor. The insulation thickness, the coaxial quality between thermo-elements, and the thickness of the junction formed at the sensing surface for a CTP are important factors for the fast response characteristics of the sensor. Therefore, the study of overall sensor morphology and anatomy (microstructural analysis and chemical characterization) is very much essential to quantify actual sensing surface thickness during its construction. The microstructural analysis has been carried out to visualize topographic details on the sensing surface under a zoomed environment, which will help to confirm matching between two thermo-elements. In order to study the sensing area topography, the surface is put under an optically zoomed environment created through a high-quality microscope, i.e., Field Emission Scanning Electron

Microscope (FESEM - Make: Zeiss, Germany; Model: Sigma). As the electron beam produced by the field emission source (mostly tungsten needle) is about 1000 times smaller than that in a standard microscope, the image quality produced is quite better. It is very efficient in delivering high-resolution pictures even under extensive magnification.

A FESEM is a microscope that works with electrons. These electrons are liberated by a field emission source. The object is scanned by electrons according to a zig-zag pattern. Electrons are liberated from a field emission source and accelerated in a high electrical field gradient. Within the high vacuum column, these so-called primary electrons are focussed and deflected by electronic lenses to produce a narrow scan beam that bombards the object. As a result, secondary electrons are emitted from each spot on the object. The angle and velocity of these secondary electrons relate to the surface structure of the object. A detector catches the secondary electrons and produces an electronic signal. This signal is amplified and transformed to a video scan-image that can be seen on a monitor or to a digital image that can be saved and processed further.

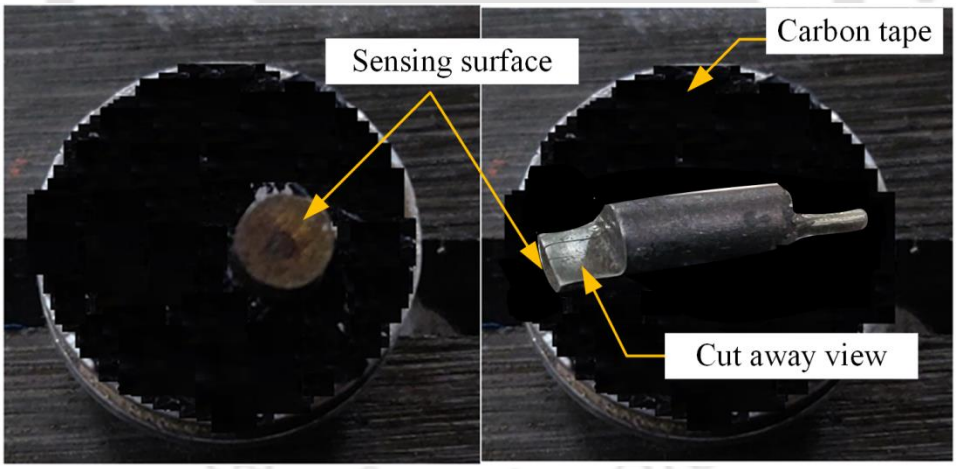

Fig. 3. 4: Sensor arrangements for study under scanning electron microscope; (a) Top view, (b) cut away view.

Preparation

In order to be observed with an SEM, objects are first made conductive for current. This is done by coating them with an extremely thin layer (1.5 - 3.0 nm) of gold or gold palladium. Further on, objects must be able to sustain the high vacuum and should not alter the vacuum,

for example, by losing water molecules or gasses. Metals, polymers, and crystals are usually a little problematic and keep their structure in the SEM.

In standard electron microscopes, electrons are mostly generated by heating a tungsten filament by means of a current to a temperature of about 2800°C. Sometimes electrons are produced by a crystal of lanthanum hexaboride (LaB6) that is mounted on a tungsten filament. This modification results in a higher electron density in the beam and a better resolution than with the conventional device. In a field emission (FE) scanning electron microscope, no heating but a so-called "cold" source is employed. An extremely thin and sharp tungsten needle (tip diameter 10^{-7} –10^{-8} m) functions as a cathode in front of a primary and secondary anode. The voltage between cathode and anode is in the order of magnitude of 0.5 to 30 kV. Because the electron beam produced by the FE source is about 1000 times smaller than in a standard microscope, the image quality is markedly better. As field emission necessitates an extreme vacuum (10^{-8} Torr) in the column of the microscope, a device is present that regularly decontaminates the electron source by a current flash. In contrast to a conventional tungsten filament, a FE tip lasts theoretically for a lifetime, provided the vacuum is maintained stable. Samples need to be mounted on a holder through a conducting material for which carbon tapes are used which are highly conductive in nature. A proper junction at the sensing surface of CTP can give a fast response. Hence, the structure and condition of the junction can be analyzed by FESEM. Different sensors have been checked by FESEM, and the bridging junction thickness over the insulation has been measured.

Fig. 3. 4 presents the top view to see the junction characteristics and to measure the bridging thickness over the junction. Along with that, a cutaway view is presented to measure the thickness of the bridging junction over the insulation. For short time applications, insulation thickness and junction thickness have fair importance. The lesser the value of the thickness, the faster the response, which helps in the accurate prediction of heat flux values.

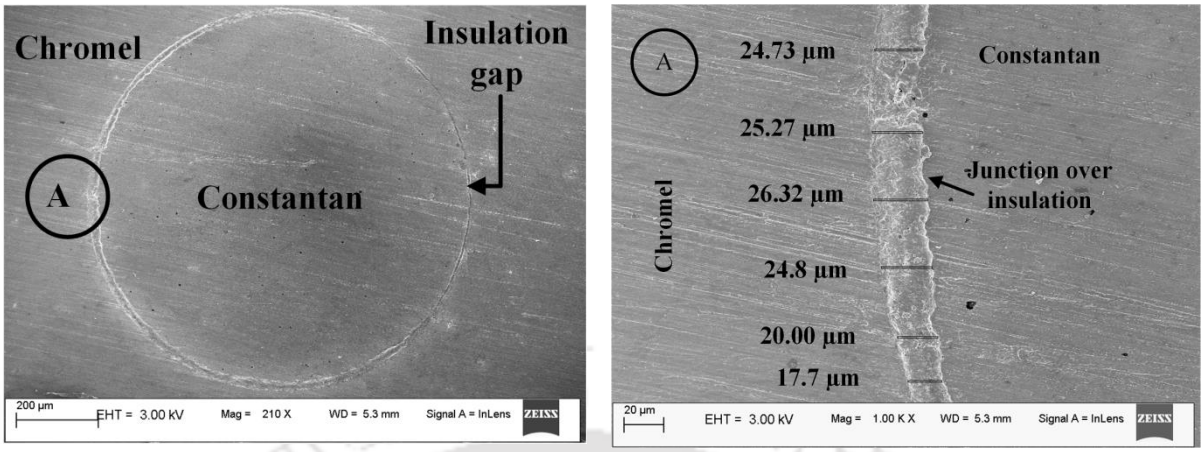

Fig. 3.5: FESEM images for the thermal probe: (a) Polished sensing surface of thermocouple; (b) Thickness of insulating layer between the thermo-elements.

In this microscopic study, the connection between two thermo-elements can be visualized, and the junction thickness over the insulation can be estimated. Referring to **Fig. 3.5 (a)**, the junction width is seen to be visible, which confirms the bridging between thermo-elements obtained through plastic deformation. In the enlarged view **(Fig. 3.5 (b)),** the junction width created over the electrical insulation is measured at a few arbitrary locations, and the average values of width are estimated in the range of 20-22 µm. The study is further extended to explore the internal anatomical features where the sensor is cut along the axis symmetrically up to a reasonable length with the help of a wire electron discharge machine (Make: Fostex, Model: FDK 7736, India). Half portion of it is used for the study under FESEM (**Fig. 3.6 (a)).** The junction height over the insulation as measured in the cut away view varies the range of 6-18.5 µm **(Fig. 3.6(b) & Fig. 3.6 (c))** while the average insulation thickness at various arbitrary locations in the cut away view section is found in the range of 20-23 µm (**Fig. 3.6 (d)**). These parameters provide an insight into the dimensional accuracy for the claim of sensing surface thickness (~20µm) during the fabrication process. Also, the image of the sensing surface confirms that both the thermo-elements are bridged and the junction is formed over the insulation.

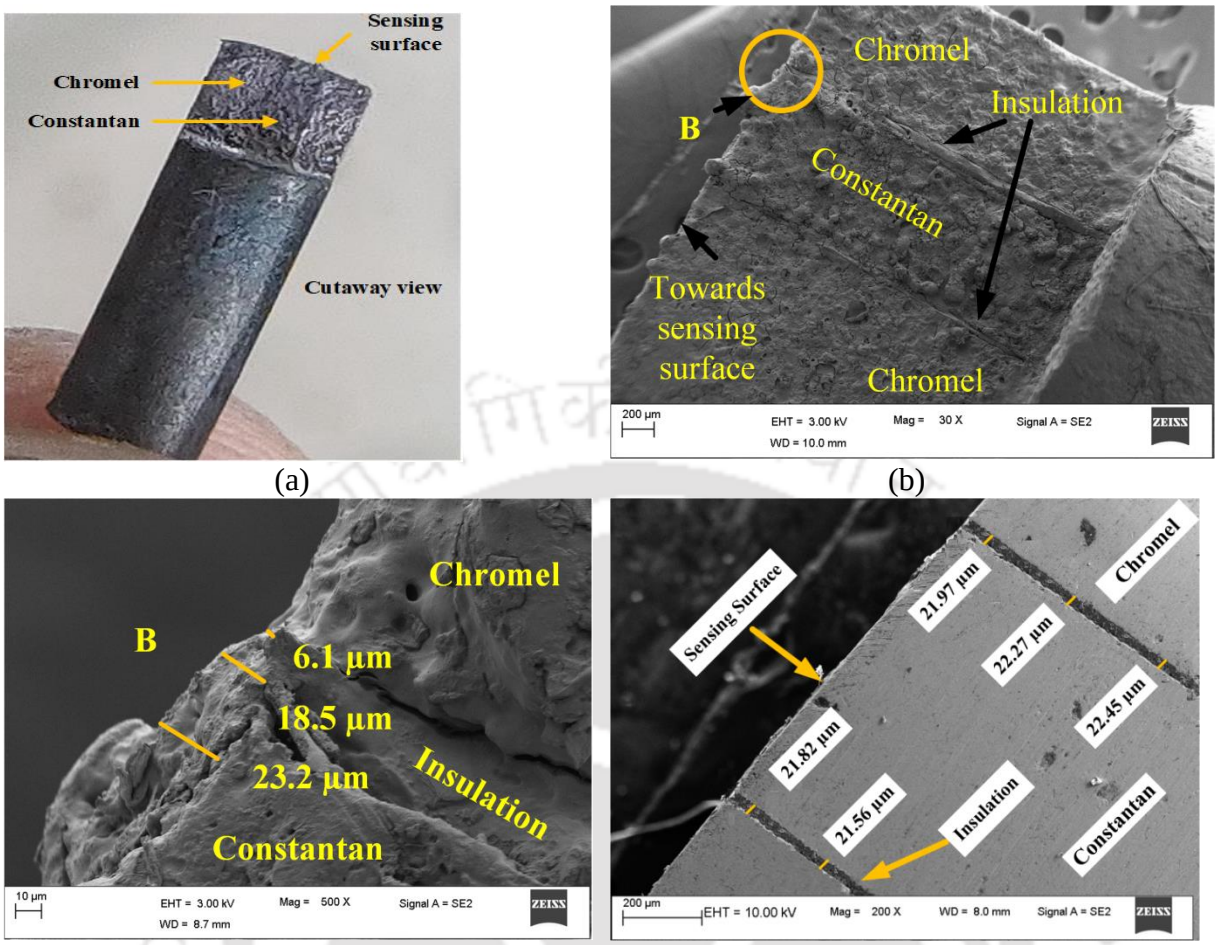

Fig. 3.6: Internal constructional features of CTP: (a) Cut way view from sensing surface; (b) Visualization of thermo-elements under FESEM for the cutaway view; (c) Junction height over insulation; (d) Thickness of insulation after polishing the cutaway view

3.5 Summary

The composition of constituent elements of the thermo-elements of the coaxial thermal probe is studied successfully using the EDX technique. The compositions are nearly similar to the materials used by other researchers. Therefore, using these materials, the sensor has been fabricated with appropriate dimensions in the laboratory scale. Along with this, the inner and outer surface dimensions such as insulation thickness, junction height, and junction depth have been studied with the help of a field emission scanning electron microscope. The dimensions are well within the acceptable range as proposed before fabrication of the probe, which indicates the dimensional accuracy of the fabrication process.

CHAPTER 4

Thermal calibration of the coaxial probe

Overview

The fabrication of the thermal probe is one of the basic requirements to proceed with the actual measurement process. The comprehensive process of in-house fabrication of the coaxial thermal probe has been explained in the previous chapter. Though these probes are meant to capture transient temperature in real-time experiments, the actual output is in terms of voltage obeying the Seebeck principle. Therefore, a relation between the voltage and temperature need to be established through a calibration process. A heated glycerine bath is used for this purpose to supply a temperature medium. The voltage is recorded for a constant increment in temperature value where the slope of the voltage-temperature plot gives the sensitivity of the probe. Apart from this, the magnitude of the thermal product of the probe is an inherent requirement for the heat flux calculation using the analytical method. Therefore, the range of thermal product values is obtained experimentally using water plunging and the water droplet technique. These experimental values are used for the estimation of heat flux. Prior to justifying the correctness of this analytical heat flux, the heat flux calibration needs to be carried out with a known value. Therefore, an experiment is carried out using laser light as a source for constant heat load. The magnitude of experimental heat flux is calculated by modeling the laser beam using the Gaussian mode analysis. The step nature of heat load from the laser imparts a temperature response to the sensor, which is recorded through a data acquisition system. These temperature signals are used to assess analytical heat flux. An independent exercise is carried out using numerical simulation with step heat load, and the results are compared with both the analytical and experimental heat flux. Therefore, this chapter mainly focuses on the calibration activities to quantify the sensitivity value, and the thermal product magnitude. The closeness of the experimental heat flux with analytical and numerical heat flux is also checked to get an idea about the deviation percentage.

4.1 Introduction

Before using the in-house fabricated thermal probe in real-time experiments, it is to pass through multiple tests for the determination of various sensor parameters. As explained in the previous chapters, the output of the CTPs is neither temperature nor heat flux; rather, it is measured in terms of voltage. Therefore, the linkage between the temperature and voltage is obtained through the sensitivity (S) of the probe. It may be noted that the magnitude of sensitivity depends on the constituent materials of the thermo-elements, and its range is defined for specific thermocouple types. However, these ideal values are not applicable for all temperature ranges and are also not valid for varying material compositions. Therefore, it is desired to determine the sensitivity value experimentally for the fabricated probe. Similarly, for the transient heat flux assessment using Duhamel's superposition integral method (Eq. 2.7), the thermal product (β) is an important requirement. The value of the thermal product is usually considered as $\beta = \sqrt{\rho c k}$ where, ρ, c, k are the density, specific heat, and thermal conductivity, respectively, of the substrate. Being an insulator, this value is taken as constant for thin-film gauges; however, it is not justified to assume constant for conducting substrate like as in CTP. It may be highlighted here that during the formation of bridging junction between the two thermo-elements at the sensing surface through the abrasion technique, the surface encounters a plastic deformation change through a combination of three different elements (two thermo-elements and insulation). Therefore, it is quite difficult to access the actual percentage of each element present on the sensing surface. Therefore, many researchers have calculated the thermal product by assuming a 50% share from each thermo-element of the CTP. The thermal product value also has an impact on the time scale of application. According to some researchers, the magnitude of thermal product value may have a deviation of ± 30% when the time scale of application changes from millisecond to microsecond (Buttsworth, 2001; Mohammed et al., 2010a; Mohammed et al., 2011). In line with the deliberation of insulating thickness in the previous chapters, the role of sensing surface is very crucial for accurate prediction of "β". With this philosophy,

few classical calibration studies (water plunging and droplet technique) have been carried out with the present CTP for experimental determination of thermal product value (β).

As explained previously, the aim of the thesis work is to assess the applicability of the CTP as a heat flux probe. Before using the probe for transient temperature measurement, it is necessary to calibrate the probe against a known heat flux source, i.e., the assessment of surface heat flux recovery from transient temperature data. The effectiveness can be predicted in the laboratory scale by divulging the sensor to a similar flow environment (step heat load) as experienced in ground-based aerodynamic test facilities such as shock tubes or shock tunnels. Laser being a monochromatic light can be effectively controlled, and the step nature of known heat load can be properly replicated. Therefore, the radiation mode of the heat transfer concept is used with the help of a laser, as it can generate a constant light source of known wattage (Kumar et al., 2011). In fact, the variations in the magnitude of such heat loads can be effectively controlled for desired time duration. Therefore, the aim of this chapter is to find out the sensor parameters through calibration processes. The calibration tasks have been discussed in the subsequent sections for the determination of sensitivity and thermal product of the probe, along with heat flux verification.

4.2 Determination of the sensitivity of coaxial thermal probe

One of the basic requirements for heat flux estimation through Eq. 2.7 is the measured transient temperature. In general, the surface junction thermocouples are active temperature detectors that generate a voltage change by obeying the principle of the "Seebeck effect." Therefore, the output from CTP is recorded in the form of voltage (ΔV) with respect to temperatures (ΔT) in the flow field.

$$S = \frac{\Delta V}{\Delta T} \tag{4.1}$$

Therefore, the conversion factor from voltage to temperature is essential as a calibration parameter of the thermal probe. The conversion factor is popularly called "sensitivity(S)"

obtained through Eq. 4.1. If the thermo-elements are pure metals, it is desired to have linear change in voltage during operating ranges of temperature. The basic calibration circuit is as given in **Fig. 4.** 1.

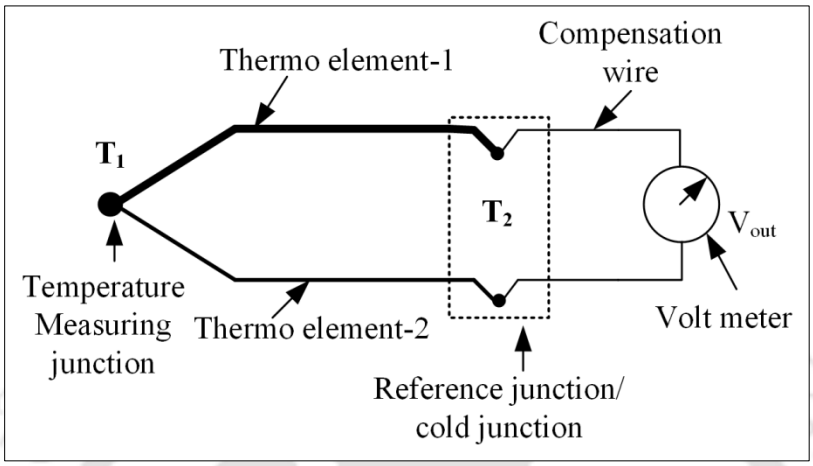

Fig. 4. 1: Calibration circuit of thermocouple

A glycerin bath experimental setup is proposed to obtain the "temperature-voltage" relationship. The setup consists of glycerin in a container, a scientific thermometer, a heater, and a data acquisition system, as shown in **Fig. 4.2 (a)**. The probe and the thermometer are placed inside the glycerin bath up to the same depth under a similar temperature environment. The container (with glycerin) is heated (magnetic stirrer-based heating element) from room temperature (25ºC) with an increment of 5ºC up to 140ºC, followed by cooling in the same sequence. The pre-calibrated scientific thermometer is used to note these temperatures. An ice bath is integrated with the thermocouple calibration circuit for cold junction compensation for the CTP. The voltage data is recorded through a data acquisition system - DAS (Make: Keysight, Malaysia; Model: 34972A/34901A). The plot between voltage and temperature for three sets of experiments shows a linear trend during the rising and trailing phase of temperature. The outcome of the calibration experiment is the determination of the "sensitivity$\left(S = 59\ \mu V/^{0}C\right)$" of the probe from the slope of the plot **Fig. 4.2(b)** , with an uncertainty band of ± 1%.

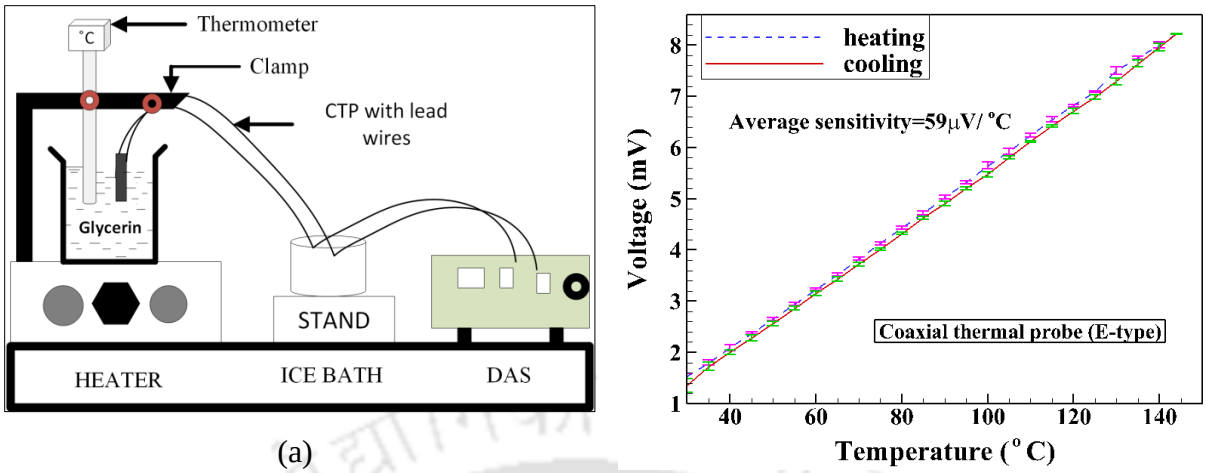

(a) (b)

Fig. 4.2: Temperature calibration of CTP: (a) Glycerine bath experimental setup; (b) Voltage-temperature relationship.

4.3 Determination of thermal product of the coaxial thermal probe

The heat flux prediction from Eq. 2.7 requires a unique thermal property parameter of the substrate in the form of a "thermal product (β)" since the formation of sensing surface is a result of irreversible plastic deformation of the thermo-elements. Hence, experimental determination of "β" is crucial since the sensing surface has mixed properties involving insulation material. Conventionally, it refers to the property of the substrate, and its value is calculated based on the materials on which the sensing surface is embedded. For thermal sensors such as TFGs, the substrate is an insulator, and it has a fixed value of "β"that can be easily calculated from the property of the materials. In contrast, the surface junction probes have metallic substrates (i.e., thermo-elements), and the sensing junction is formed only on the surface. There is continuity in-between the sensing material as well as substrate material due to the conducting nature of the substrate. Additionally, the analogical substrate material in the case of CTP is a combination of two thermo-elements. Ideally, the effective thermal product value 8650 $J/m^2s^{0.5}K$ is reported in which researchers have considered with 50 % share from each thermo-element by neglecting the properties of insulating materials (Desikan et al., 2016). In a realistic sense, the formation of the sensing surface is a consequence of thermo-elements and the insulating layer, which makes a significant

difference in thermal properties with respect to thermo-element properties. Therefore, experimental determination of this thermal product value can provide a magnitude of the thermal product along with its uncertainty range.

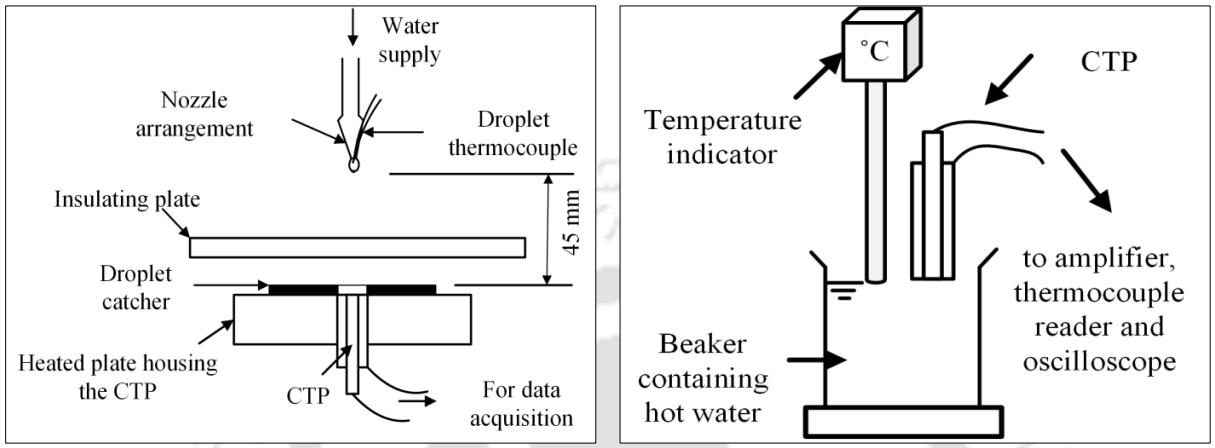

(a) (b)

Fig. 4.3: Experimental setup for determination of thermal product: (a) Water droplet method; (b) Water plunging technique.

The "droplet and plunging" methods are two simple and effective techniques often adopted by researchers for experimental determination "β" in the laboratory scale (Agarwal et al., 2016). In the droplet technique, a fluid droplet is allowed to fall on the heated sensor, and in other case, the sensor is exposed to a heated fluid ambiance. Hence, there is an instantaneous transfer of heat for which the contact temperature at the interface of the sensing surface can be recorded due to the fast response characteristics of CTP. The same procedure has been adopted here as schematically shown in **Fig. 4.3 (a),** where "water" is used as the fluid. The sensing surface of the probe is heated to a temperature of T_s and remained stationary. A tiny droplet of water at ambient temperature (T_w) accelerated from rest under gravity and impacted on the sensing surface. The height is adjusted so that the droplet almost covers the sensing surface. In another independent thermal loading, i.e., "water-plunging" test, the sensing surface (T_s) of the probe is suddenly exposed to an environment of hot water at T_w **(Fig. 4.3 (b)).** This is quite similar to the droplet method, but the operation is different, and the time scale of plunging can be varied. The sensor element of the probe is suddenly placed inside the hot water bath and taken out immediately depending on the time duration of the

study. The experiments for both methods are conducted for different values of T_w and T_s . The typical temperature response detected through voltage signals acquired through the data acquisition system (DAS) is shown in **Fig. 4.4**. Ideally, there is a step change at the interface of the probe, when the water droplet at temperature T_w comes in contact with the heated probe at temperature T_s (water droplet test) or the probe at room temperature T_s comes in contact with hot water at T_w. The contact temperature $\left(T_{ct}\right)$ at the surface of CTP can be related to known thermal product value of water $\left(\beta_w\right)$ for determination β through in Eq. 4.2. More details of the methodical approach may be found from references (Agarwal et al., 2016).

$$\frac{T_{ct}-T_s}{T_w-T_s}=\frac{\beta_w}{\beta_w+\beta};\ \ \beta_w=1643\ \mathrm{J/m^2Ks^{0.5}} \tag{4.2}$$

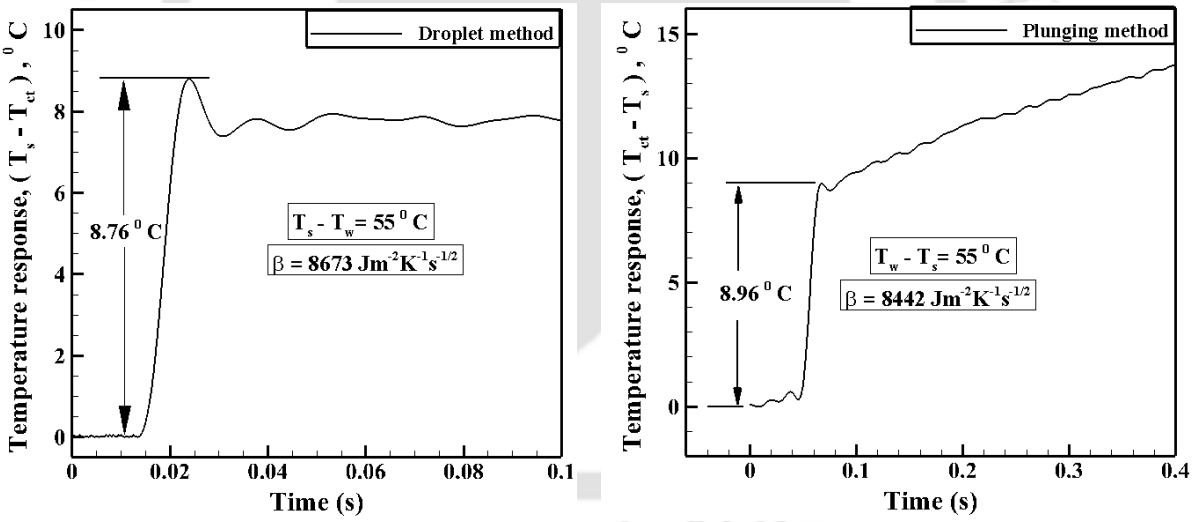

(a) (b)

Fig. 4.4: Temperature response from CTP for determination of thermal product: (a) water plunging method; (b) water droplet test.

The calculated thermal product values from plunging and droplet methods obtained as are $8442\pm5\%\ \mathrm{J/m^2Ks^{0.5}}$ and $8673\pm5\%\ \mathrm{J/m^2Ks^{0.5}}$, respectively. It should be emphasized that the response time is quite slow during the plunging test, and there is a gradual stepping

function when the CTP is immersed in a hot bath (Desikan et al., 2016). The pre-sensing effect of CTP leads to the deviation of β value with respect to the water-droplet test. Hence, for all subsequent calculations, the experimental value of $\beta = 8673\ \mathrm{J/m^2 K s^{0.5}}$ is used for the computation of surface heat flux through Eq. 2.7.

4.4 Heat flux calibration for coaxial thermal probe

A continuous-wave **(**CW**)** direct diode laser system **(**Make**:** Coherent USA; Model: HL-FAP 30**)** assisted with thermal probe mountings, voltage amplifiers, and a PC integrated data acquisition system form the experimental setup **(Fig. 4.5)**. The instrumentation unit consists of an amplifier (with a gain of 500) and an oscilloscope (Make: Tektronix, USA; Model: MDO3024) to record the data from the thermal probe with a sampling rate of 50000 per second. The laser source is integrated with a focusing unit for restricting the beam within the working environment. The thermal probe (CTP) is fixed on a support stand at a distance of 120 mm for complete receipt of the heat load on the sensor surface of 3.25 mm diameter (**Fig. 4.6**). Laser light of known wattage (in the range 0.2 W-0.5 W) is allowed to fall on the sensor, and a laser power meter (an integral part of this unit) checks the accuracy of this wattage and is controlled through a software interface.

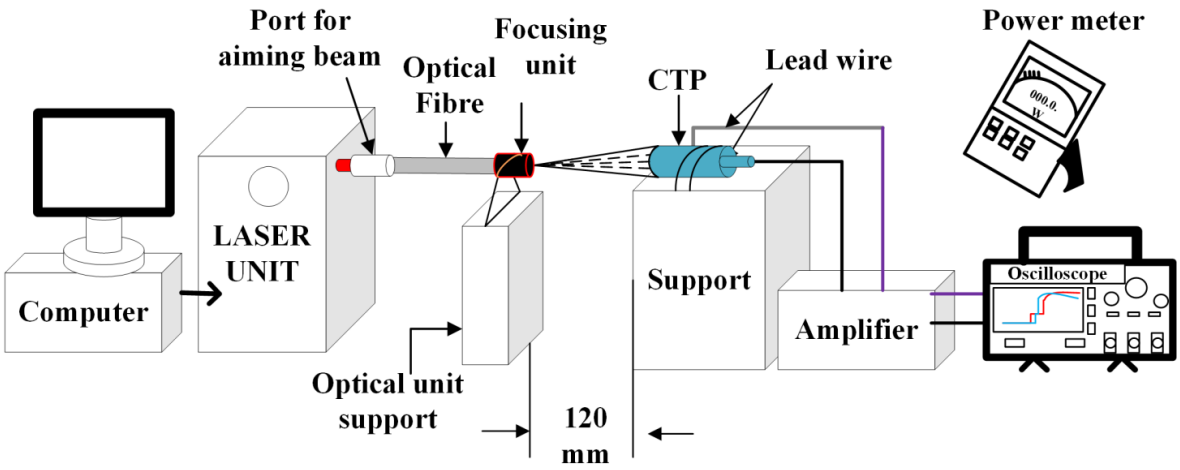

Fig. 4.5: Experimental arrangement for laser based heat load exposure for CTP.

During the experimentation, only laser wattage is varied by keeping other operating parameters fixed. The laser unit is instantaneously tuned so that the thermal probe receives a

short duration step heat load for 1.5 s. The detailed working procedure of this calibration procedure has been explained in **Fig. 4.7**. The voltage signals captured from the probe for different step heat loads of 1.5s duration are presented in **Fig. 4.8**. The temperature response corresponding to the voltage change is interpreted in **Fig. 4.9 (a-d)** with the knowledge of the sensitivity value of the probe. In line with the literature findings, a parabolic rise in the trends of temperature response seems to be characteristics of the surface junction probe when exposed to a step heat load (Bergman et al., 2011).

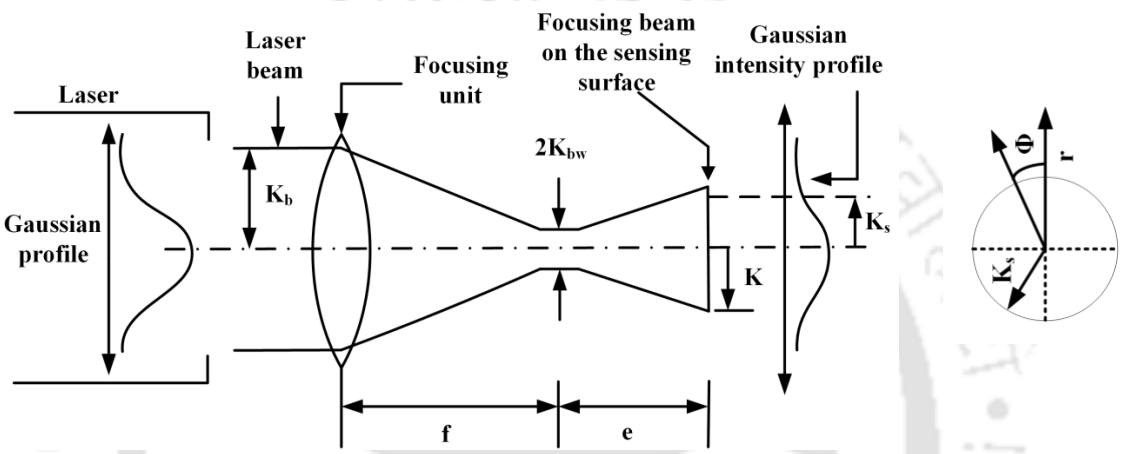

Fig. 4.6: Schematic of Gaussian profile of laser beam.

4.4.1 Estimation of surface heat flux values

In the present experiment, the CTP receives heat load from the laser source principally due to the radiation mode of heat transfer. Due to small experimentation time (1.5s), the view factor can be approximated nearly unity for which the losses due to radiation can be neglected. Hence, the popular analytical modeling of recovered heat flux $(\dot{q}_a)$ from transient surface temperatures is equivalent to one-dimensional heat conduction in a semi-infinite substrate. The other independent approach is to follow the temperature responses as an input for numerical simulation modeling and subsequently recover surface heat fluxes $(\dot{q}_{nu})$. The main intention of the heat flux calibration is to compare the time-average values of surface heat flux during the steady region and map it with supply input heat flux $(\dot{q}_{in})$ for different laser wattages.

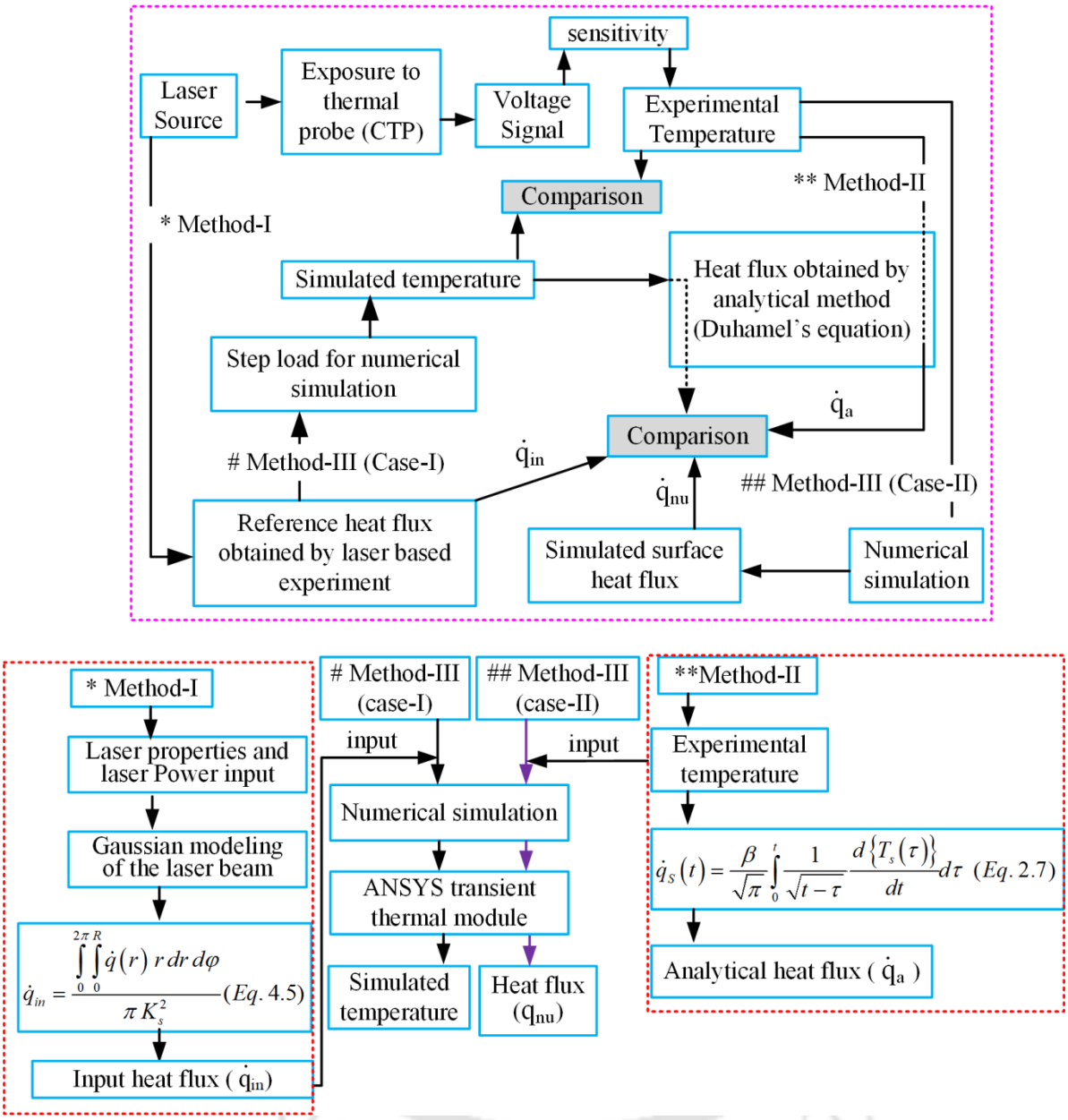

Fig. 4.7: Schematic of working methodology for laser-based heat flux calibration.

The laser beam generated through a diode is often approximated to follow a "Gaussian intensity distribution," as reported in the literature (Kant and Joshi, 2013; Sarma, 2017). Due to diverging nature of the laser beam, it is necessary to concentrate the beam with the help of a lens having a focal length, (f) as shown in **Fig. 4.6**. The laser light does not converge to a point obeying the basic laws of nature, which will make its power (wattage/area) infinity at that point; rather, it converges to a minimum possible spot size at

the focus of lens called as "beam-waist $(2K_{bw})$." Beyond this, the laser beam again diverges, and its diameter increases. The distance from the beam-waist to the sensing surface of the CTP is called "standoff distance (e)." For a comfortable working position **(Fig. 4.5),** the CTP can be placed at an appropriate location at a distance $(f+e=120\,\text{mm})$ where the laser beam diameter $(2K)$ can provide complete coverage to the diameter of the sensor surface $(2K_s)$. This beam radius can be calculated from the standard beam propagation equation (Eq. 4.3) available in reference.

$$K=K_{bw}\left[1+\left(\frac{Q\lambda e}{\pi K_{bw}{}^2}\right)^2\right]^{\frac{1}{2}};\quad K_{bw}=\frac{2Q\lambda f}{\pi D};\quad D=2K_b \tag{4.3}$$

Here, Q is a quality factor which is unity for a theoretically ideal Gaussian beam (Kant and Joshi, 2013; Sarma et al., 2016b). The wavelength $(\lambda=808\text{ nm})$ and focal length of the lens $(f=80\text{ mm})$ are taken from the manufacturer's specification, and the beam diameter value $(\text{D}=10\,\text{mm})$ before the lens is calculated by using an optical bench and beam diameter measurement device. By approximating the distribution of laser intensity on the surface following a Gaussian trend, the heat flux distribution $\{\dot{q}(r)\}$ at any radial location can be calculated from Eq. 4.4.

$$\dot{q}(r)=\frac{2\eta P}{\pi K^2}\exp\left(\frac{-2r^2}{K^2}\right) \tag{4.4}$$

Where, P is the laser power input and η is the absorption coefficient, which is a function of the material property on which the laser beam is focused. The total heat load imposed over the sensor surface can be calculated by integrating Eq. 4.4. Further, the time average values of actual heat flux received by the sensor surface can be calculated by averaging the heat load over the entire surface area of the sensor using Eq. 4.5.

$$\dot{q}_{in} = \frac{\int_0^{2\pi}\int_0^{R} \dot{q}(r)\, r\, dr\, d\varphi}{\pi K_s^2} \tag{4.5}$$

4.4.2 Data analysis for interpretation of surface heat flux

The exact quantification of experimental heat flux $(\dot{q}_{in})$ requires the knowledge of laser wattage as an input with an exposure area of the sensing surface of 3.25 mm diameter by considering Gaussian mode analysis (Method I). Consequently, the traces of experimental surface temperatures are obtained from the probe, as shown in **Fig. 4.9 (a-d).**

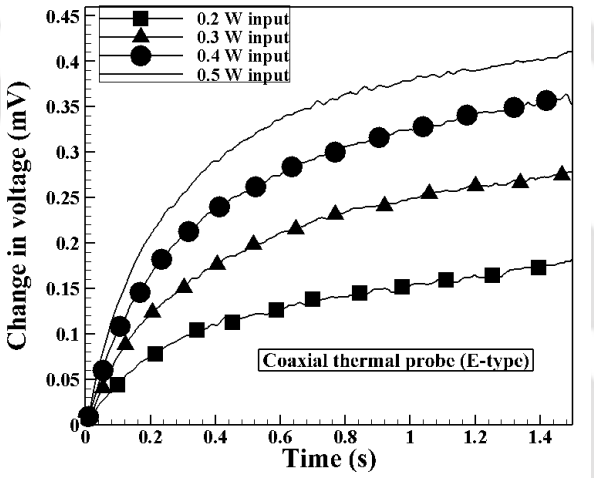

Fig. 4.8: Voltage signals obtained from the probe at different laser wattage.

During short time scale experiments, there is no direct method for estimation of surface heat flux $(\dot{q}_a)$ rather; they are predicted analytically from surface temperature histories (Method II) through Eq. 2.7 as an output. Side by side, it is also possible to perform computational investigations either for predicting surface temperatures through experimental heat flux inputs or for predicting heat flux $(\dot{q}_{nu})$ from the derived experimental temperature signals from the thermal probe (Method III).

Complete coverage of all possible comparisons of various temperature and heat flux histories is correlated in the flow chart shown in **Fig. 4.7**. The findings of experimental data and calculations by the above methods are analyzed in this section. The analytical method of heat

flux modeling is used to discretize the temperature signals, and with the help of spline fitting, the heat flux values are assessed.

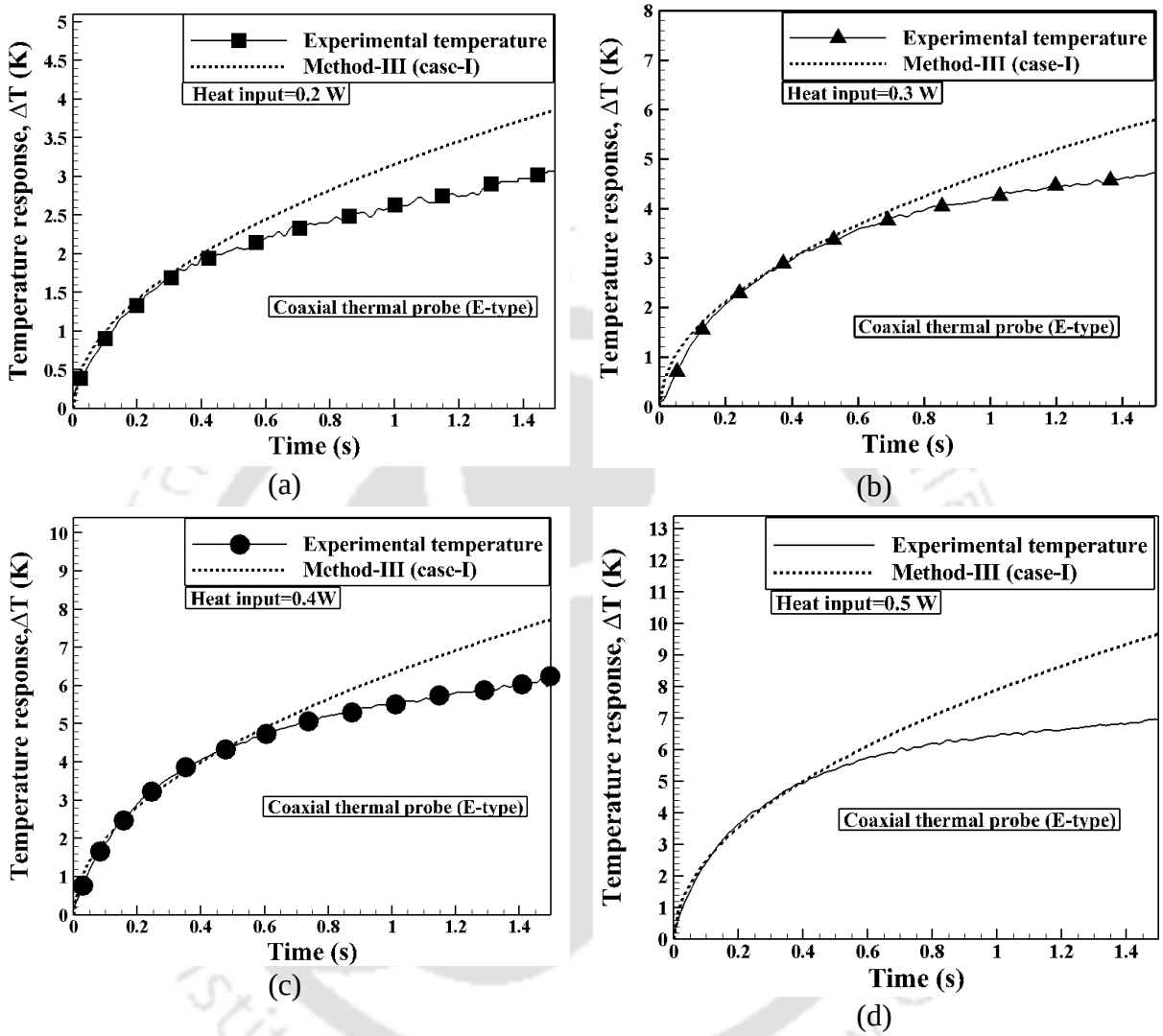

Fig. 4.9: Comparison of surface temperature histories from experiments and numerical simulations at different laser wattage: (a) 0.2 W; (b) 0.3 W; (c) 0.4 W and (d) 0.5 W.

4.4.3 Analytical method of heat flux determination

The prediction of surface heat flux from the temperature histories with appropriate one-dimensional heat conduction modeling is the theme of the investigation. The classical methods involve computations of heat flux by assuming the probe either as a semi-infinite/thin-wall/thick-wall calorimetric gauge (Sahoo and Kumar, 2016). In this case, the method for recovering heat transfer rates from transient temperature rise during the test time

(1.5 s) follows one-dimensional heat conduction modeling with a semi-infinite assumption (Taler, 1996).

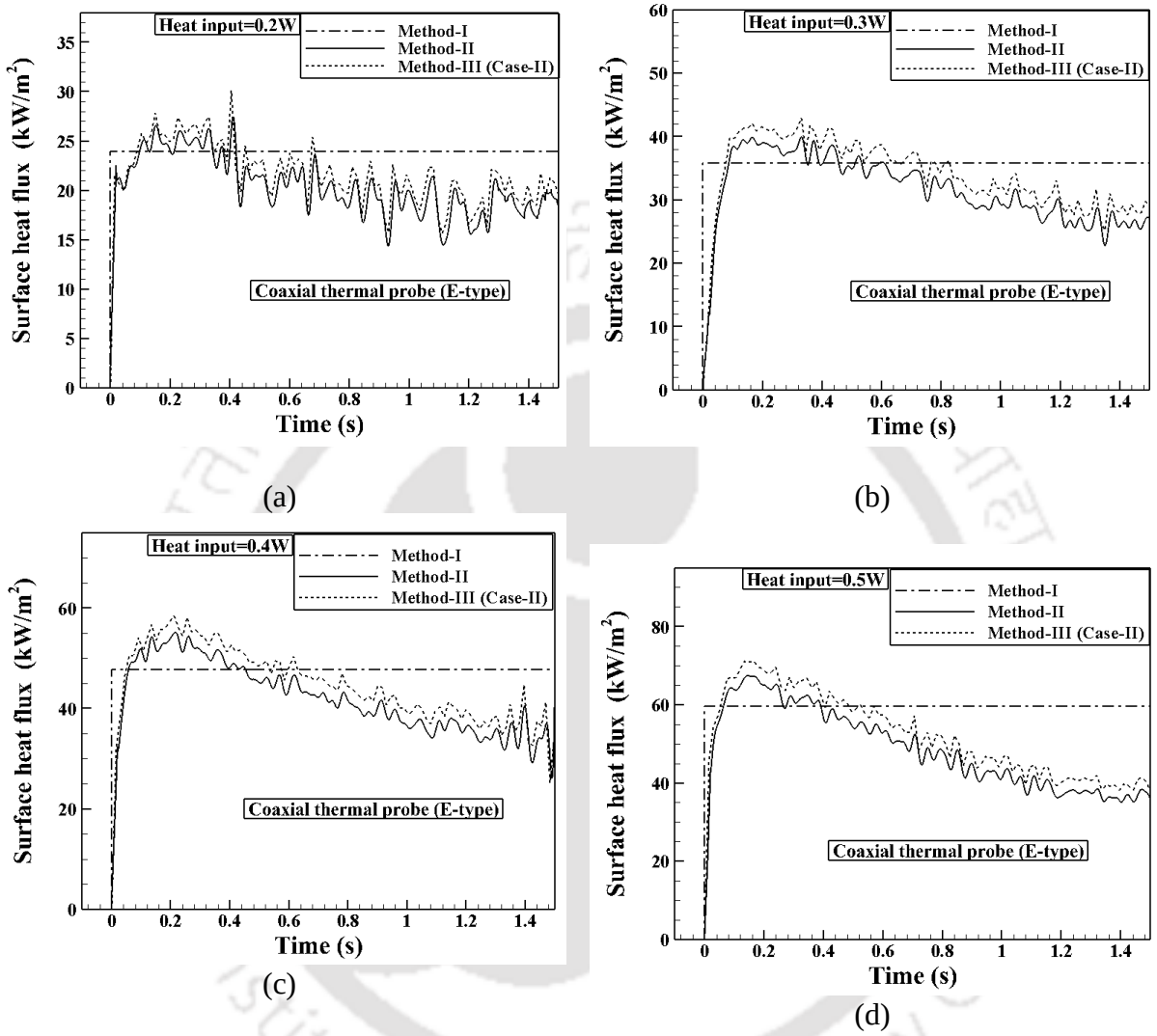

Fig. 4.10: Comparison of surface heat flux histories at different laser wattage: (a) 0.2 W; (b) 0.3 W; (c) 0.4 W and (d) 0.5 W.

The estimation of surface heat flux requires discretization of the temperature data, for which the cubic spline fitting technique (third-order spline) has been used to discretize the temperature signal data. The corresponding heat flux histories for all input heat loads are obtained from the discretized temperature signals. As seen from **Fig. 4.10**, the heat flux signals show a sudden rise in heat flux value resembling a step jump in the heat load followed by a gradual drop in heat flux values beyond 0.4 s. It may be emphasized here that

surface heat flux is obtained through a one-dimensional heat conduction assumption with a semi-infinite substrate. In the present sets of the experiment, the time scale of 0.4 s seems to be optimal for the acquisition of experimental data for which the surface heat flux can be predicted with reasonable accuracy ± 5 % between the evaluations (Method I & Method II). After this time, the heat flux signals show a gradual drop until the end of acquisition (i.e., 1.5 s), as noted from **Fig. 4.10**. When comparing with the experimental surface heat flux calculated by Method I (59.7 kW/m^2), the accuracy in the prediction of surface heat flux (from the temperature histories) is highly unreliable since the deviation could be as high up to 35 %. Since both the thermo-elements of the probe are metallic, the thermal inertia of the sensor is lost with the penetration of heat in the longitudinal direction through the probe. Moreover, the directionality effect becomes significant for longer time scale estimates during which there are chances of heat penetration in the lateral direction as well. These could be possible reasons for these deviations. Thus, in the real-time experimental acquisition of temperature response with a test duration of 0.4s, the usage of a thermal probe seems to be justified while predicting the surface heat flux through one-dimensional heat conduction with semi-infinite assumption.

4.4.4 Numerical simulation

In the previous section, it has been shown that heat flux predictions from the transient temperature data through one-dimensional modeling seem to be reasonably accurate if the experimental time scale is less than 0.4s. While justifying the practical usage of the probe in the realistic application, it is also felt to reassure this fact with a computational investigation. The simulation has been performed with the help of standard software package (ANSYS 14.5). Here, the problem definition for simulation of the thermal probe is divided in two parts: in the first case, the surface temperatures are recovered through experimental heat flux inputs from the laser wattage (Case I) and in the other case, the surface heat fluxes are recovered from the experimental temperature responses of the probe (Case II). For both cases, computational domains for numerical simulation are shown in **Fig. 4.11 (a&b),** which include a schematic of the sensor with boundary conditions. The dimensions of the sensor are

the same as that experimental probe, and the thermal properties of the material used in the simulation are given in **Table 2.1**.

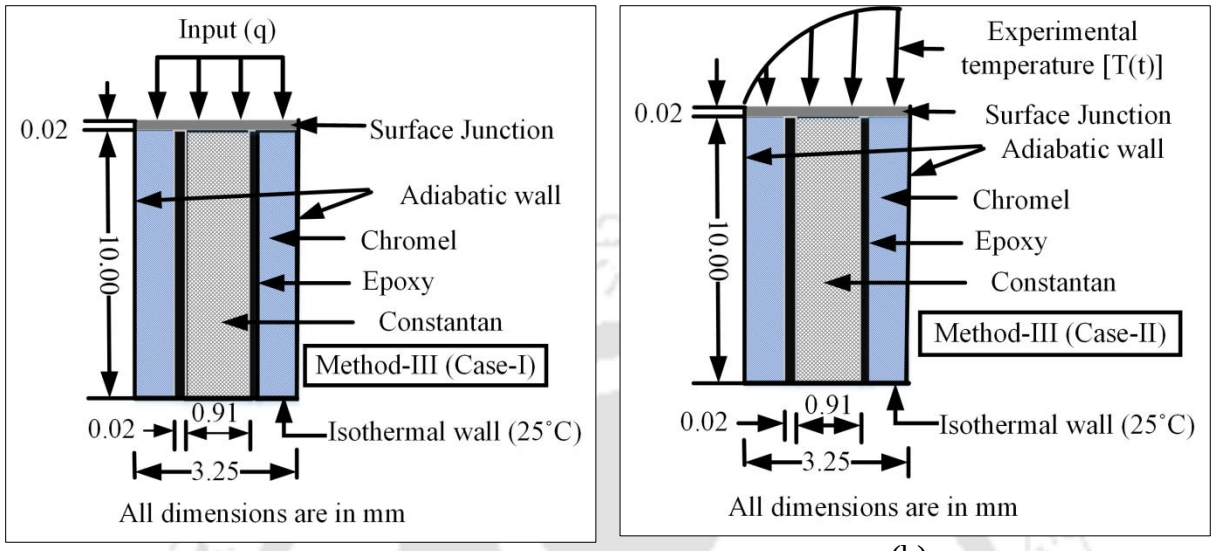

Fig. 4.11: Computational domain of CTP for numerical simulation: (a) Heat flux as step load on the sensing surface – Case I; (b) Temperature signal as input on the sensing surface – Case II.

The ANSYS transient thermal module flow solver is used for the entire simulation. A mesh independent study has been performed to check the dependency of the results on the mesh by adopting three different combinations of nodes (1555647, 1626896, and 1714609). The surface temperature history shows consistent results for all the three combinations of nodes for the input heat load of 0.3 W applied through the laser source **(Fig. 4.12 (a))**. In a similar manner, the grid independence study is repeated for input experimental temperature responses for another laser wattage of 0.5 W, and the surface heat flux histories shows consistent predictions as shown in **Fig. 4.12 (b)**. The consistent results are shown in **Fig. 4.12 (b)**, which assures the grid-independent studies in both cases of these numerical simulation methods as mentioned in **Fig. 4.11.** In order to minimize computational time, a lesser no of nodes are selected for the simulation for all subsequent computational studies.

In the first part of numerical simulation (Case I), the recovered surface temperatures obtained from various heat loads of laser wattage are superimposed in **Fig. 4.9 (a-d),** which exactly replicates the original temperature response from the probe till time domain of 0.4s.

The deviation in recovered surface temperature increases after this time, and the maximum value of this deviation is noticed as 35 % at 1.5s. The probable reason could be heat loss in the lateral direction due to loss in thermal inertia of the sensing surface for preserving heat only on the surface. This loss of heat is reflected as a drop in surface temperature acquired by the probe. This fact could not be assured due to limitations in numerical thermal modeling adopted in the present flow solver.

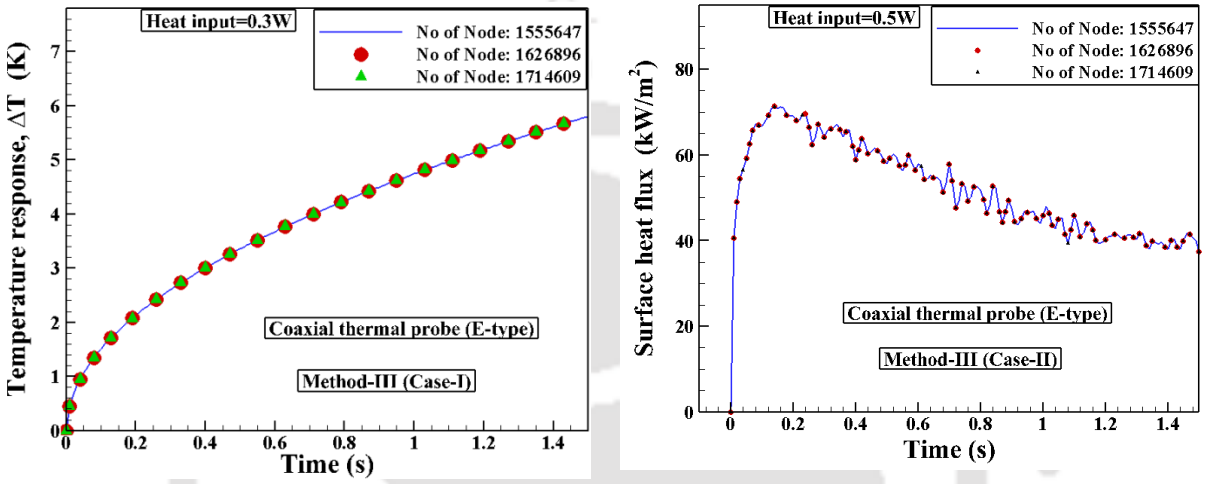

(a) (b)

Fig. 4.12: Grid independent study for numerical simulation: (a) Surface temperature recovered from experimental heat flux as input – Case I; (b) Surface heat flux recovered from the tempersture response of the thermal probe – Case II.

The recovered surface heat flux predicted from temperature response (Case II) for different laser wattages are compared in **Fig. 4.10 (a-d).** The nature of surface heat flux histories follows almost similar trends for all laser input wattage. As seen from **Fig. 4.10,** the heat flux signals show a sudden rise in heat flux value resembling a step jump in the heat load followed by a gradual drop in heat flux values beyond 0.4 s. This is exactly followed in a similar manner as predicted via convolution integral (Eq. 2.7) through Method II. The time-varying decrement in the heat flux happens due to a drop in temperature responses. It is also noted that beyond a time scale of 0.4 s, both the temperature and heat flux plots show deviation from the reference values. This may be due to the penetration of heat towards the distal end of the sensor. Thus, the time scale of 0.4 s seems to be appropriate, for which the surface heat flux can be predicted with reasonable accuracy (within 3 %). It may be noted

from **Fig. 4.10** that the heat flux signals show a gradual drop from 0.4 s till the end of the acquisition time scale (i.e., 1.5 s). During this period, deviation could increase as high up to 33 % when compared with the experimental surface heat flux calculated by Method I. The numerical prediction is based on the assumption of one-dimensional heat transfer and the isotopic nature of the material (i.e., constant thermal properties). However, the fabricated probe does not satisfy the mentioned assumptions completely because the sensor is a combination of three different materials and hence, three different thermal properties (two thermo-element materials and one insulation material). So, the sensor exhibit more complex behavior than what is predicted by the one-dimensional heat conduction model.

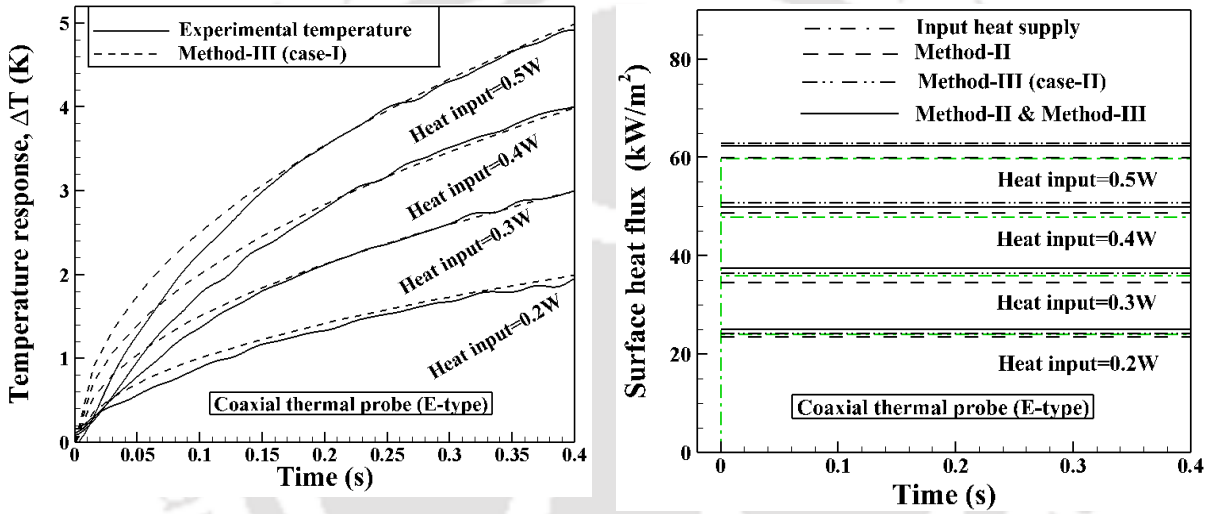

(a) (b)

Fig. 4.13: Comparison of simulated and experimental data in a test window of 0.4 s: (a) Surface temperature history; (b) Time average surface heat flux estimates.

4.4.5 Comparative assessment of surface heat flux

In this part of data analysis, the recovered surface heat fluxes are compared for a test window of 0.4 s by considering the validity of one-dimensional semi-infinite assumption for the probe, irrespective of the methods adopted for estimation. For this purpose, the transient temperature data are considered for all input heating loads, only for 0.4 s, during which the deviations are in a range of ± 5 % (**Table 4.1**). The average values of surface heat fluxes during this time are analyzed by considering direct experimental temperature response from the probe (Method II) inferred temperature response (Method III – Case I). The temperature

responses are parabolic in nature, as shown **Fig. 4.13 (a),** and the corresponding estimated heat loads **(Fig. 4.13 (b))** are a step in nature. It is essentially the transient response characteristic of calorimetric thermocouple gauges, as emphasized in the literature. In addition, the experimental heat flux estimations (Method I) are also superimposed in **Fig. 4.13(b)** with a similar range of accuracy. Hence, the extended validity of the time domain of the one-dimensional semi-infinite assumption for the fabricated temperature probe has been justified through this analysis. Thus, in the real-time experimental acquisition of temperature response with a test duration of 0.4s, the usage of a thermal probe as a "heat flux sensor" is deemed fit in all types of transient applications.

Table 4.1: Comparison of time average values of surface heat flux for Gaussian heat input and recovered output for 0.4s.

Input heat flux $\dot{q}_{in}$ (kW/m^2)	$\dot{q}_a$ (kW/m^2)	Deviation (%) $\left\|\left(\frac{\dot{q}_{in}-\dot{q}_a}{\dot{q}_{in}}\right)\times 100\right\|$	$\dot{q}_{nu}$ (kW/m^2)	Deviation (%) $\left\|\left(\frac{\dot{q}_{in}-\dot{q}_{nu}}{\dot{q}_{in}}\right)\times 100\right\|$
23.9 (input laser wattage: 0.2W)	23.4	2.0	24.1	0.83
35.85 (input laser wattage: 0.3W)	34.6	3.48	36.4	1.53
47.8 (input laser wattage: 0.4W)	48.7	1.88	50.5	5.64
59.7 (input laser wattage 0.5W)	59.9	0.33	62.7	5

4.5 Assessment of heat flux for a different experimental time scale

Following the previous approach, the heat flux values are compared for 20 ms duration as it is the common experimental time scale as followed in the case of shock tube experiments. Therefore, two higher wattage laser inputs (2W and 3W) as compared to the previous one are allowed to fall on the sensor, and the temperature response is recorded. This temperature response is used to access the heat flux values analytically and through numerical simulation, as explained in the previous sections. The temperature and heat flux response is plotted in **Fig. 4.14.** The time-averaged heat flux values calculated through this analysis for two

different wattages of laser are presented in **Table 4.2**. Within the overall test window of 20 ms, there is a sharp rise in surface heat flux values within 1.5 ms with subsequent steady region prevailing for the rest of the time **Fig. 4.14 (b)**. While comparing it with time average values of surface heat flux calculated through Eq. 3), only 0.5 % and 1.87% deviation is noted for 2W and 3W, respectively. Along with the heat flux assessment, it is quite justified to re-assure the behavior of the temperature signals through numerical simulation (**Fig. 4.7**). Therefore, another numerical simulation is carried out with Gaussian heat flux $(\dot{q}_{in})$ as step input for 20ms. The inferred temperature history is compared with the experimental temperature signal. The comparison of both the temperature signals is plotted in **Fig. 4.14 (a)** resembles exactly similar characteristics.

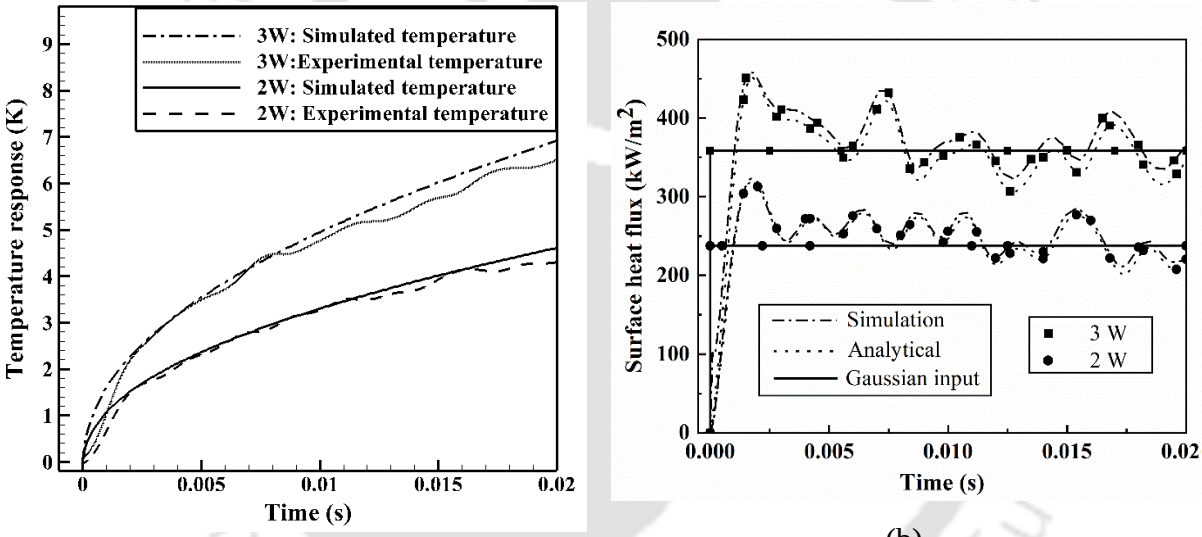

(a) (b)

Fig. 4.14: Laser-based calibration assessment of CTP for 20ms window: (a) Comparison of temperature responses; (b) Estimated surface heat fluxes.

Table 4.2: Comparison of time averaged values of surface heat flux for Gaussian heat input and recovered output for 20 ms.

$\dot{q}_{in}$ (kW/m^2)	$\dot{q}_a$ (kW/m^2)	Deviation (%) $\left(\frac{\dot{q}_{in}-\dot{q}_a}{\dot{q}_{in}}\right)\times 100$	$\dot{q}_{nu}$ (kW/m^2)	Deviation (%) $\left(\frac{\dot{q}_{in}-\dot{q}_{nu}}{\dot{q}_{in}}\right)\times 100$
239 (input laser wattage: 2W)	237.7	0.5	246.6	3.2
358.5 (input laser wattage: 3W)	351.7	1.9	364.6	1.7

4.6 Summary

Determination of the sensor constants (sensitivity and thermal product) and heat flux calibration of the coaxial thermal probe are the main focus of this chapter. The sensitivity of the probe is obtained using a glycerin bath set up, and the magnitude is obtained as 59µV/ºC. Similarly, the magnitude of thermal product is obtained experimentally using plunging and droplet technique, and the values are calculated as $8442 \pm 5\%\ \mathrm{J/m^2 K s^{0.5}}$ and $8673 \pm 5\%\ \mathrm{J/m^2 K s^{0.5}}$ for plunging and droplet, respectively. The recovered heat flux magnitude is compared with the experimental heat flux obtained from the laser-based experiment, and the heat flux matches pretty well within a time period of 0.4s. The heat flux magnitude is also obtained with the help of numerical simulation and validated with the analytical and experimental heat flux well within the acceptable error band. Therefore, it can be concluded that this in-house fabricated probe can be used for short-duration heat flux recovery within an acceptable error band.

CHAPTER 5

Real time application of coaxial thermal probe for step heat load

Overview

The modeling, fabrication, characterization, and calibration aspects of the CTP have been explained in the previous chapters. After successfully completing all these tasks, it is necessary to check its response in a ground-based aerodynamic testing facility. This is because the fast response characteristic is one of the reasons for the usage of these probes for transient temperature measurement in short-duration experiments. Therefore, the present chapter focuses on testing the sensor in a shock tube installed in the "Gas dynamics laboratory" of IIT Guwahati. The shock tube is a laboratory tool primarily used for the artificial generation of shock waves. It is a continuous hollow tube where the entire space is divided into two sections;"driver section" (high-pressure section) and "driven section" (low-pressure section) separated by a diaphragm. Shock wave is generated at the diaphragm location with the sudden bursting of the diaphragm due to the pressure difference. The in-house fabricated sensors are well packed and mounted at different locations of driven section of the shock tube and at the end flange. The probes are flush-mounted on the specified locations such that the flow remains undisturbed. The heat load imparted on the sensor is of step/impulsive in nature. The response to the shock flow is captured simultaneously by the CTP and a high frequency pressure transducer, mounted at the same circumferential location facing each other. Similarly, both the probes are mounted at the end flange facing the same flow conditions. The response is captured for both the conditions and compared. The response of CTP is also compared with a silver thin film gauge by mounting both at the end flange. The sensor responded well to the shock wave proving its fast response characteristics. As the central theme of the project work is to estimate the heat flux values, the temperature response is used to estimate the same. The temperature signals are evaluated analytically by modeling the sensor as a semi-infinite body with one-dimensional heat conduction. All the results are also validated through numerical simulations.

5.1 Introduction to shock tube

After the successful modeling, fabrication, and characterization of the thermal probe, it is proposed to check its response in a ground-based aerodynamic testing facility. Usually, ground-based tests are conducted using wind tunnels and impulse facilities such as shock tubes, free piston shock tunnels (Stalker, 1967), and expansion tunnels which are capable of imitating the actual flow condition experienced by the space vehicles. The shock waves generated inside the shock tubes and shock tunnels impart step/impulsive heat loads on the sensors mounted on the shock tube directly or through any aerodynamic model. Therefore, the main aim of the ground based facilities is to produce “shock waves” artificially.

The shock wave is a type of propagating disturbance that travels faster than the local speed of sound in the medium. When an object moves with a velocity greater than the velocity of sound in that particular medium (say air), then the existence of the object is not felt by the upcoming stream of air. This happens so due to the fact that; the information travels as a pressure wave (sound wave) which is lesser than the object speed for the present case. Therefore, the fluid particles get a head-on collision with the object and try to carry the information towards upstream and get again compressed by the upstream flow, making a very thin obstructive layer in front of the object. The modern concise definition of shock was was first proposed by G. Zemplen from the University of Budapest in year 1905. As defined by Zemplen and I quote “A shock wave is a surface of discontinuity propagating in a gas at which density and velocity experience abrupt changes (Jagadeesh, 2008). Depending on the shape of the shock wave, it is defined in various categories like normal shock, oblique shock, bow shock,etc. The order of thickness of the shock wave is nearly an order of 200nm. Though the thickness is very small, the flow properties (such as pressure, temperature, Mach number, etc.) change drastically across it. The deadliest shock wave is the normal shock being perpendicular to the flow field across which the Mach number decreases but, the temperature and pressure increase manyfold. Therefore, understanding the phenomena helps

in the design of modern aerospace vehicles. These waves are created in the labotaory scale in a popular device known as shock tube.

The “shock tube” is a laboratory tool used to generate shock waves. These are popularly referred to as the test tubes of gas dynamicists. It is a closed tube of circular cross-section (mostly preferred) or rectangular cross-section inside which two gases with high-pressure differences are separated by an obstruction (**Fig. 5.** 1). When the obstruction is released instantaneously, the high-pressure gas (present in the driver section; i.e., section 4) travels towards the driven section (driven section; i.e., section 1), generating a shock wave (mostly normal shock). The obstruction can be controlled electronically, mechanically, etc. In mechanically operated shock tubes, many a time a diaphragm is used to separate both the gases. When the diaphragm bursts suddenly due to high-pressure difference, a shock wave is generated, which travels towards the driven section (section 1), and an expansion wave travels in the opposite direction, i.e., towards the driver section (section 4). The propagation of the shock wave creates a high-pressure region behind it (section 2) and also induces a mass motion that follows the shock wave (**Fig. 5.** 1). A thin line of partition between the driver and driven gas happens to remain during the movement towards section 1, which is the interface between the driver gas and driven gas and is named as “contact surface.” Across the contact surface, the magnitude of velocity and pressure are equal, i.e., $p_3 = p_2$ and $u_3 = u_2$. On the other hand, the expansion wave propagates to the left, smoothly decreasing the pressure in section-4. Basically, the thickness of the diaphragm, properties of driver gas, and properties of driven gas determine the strength of the primary shock wave that travels into the driven tube. After reaching the end flange of the shock tube, the shock wave encounters a flat end wall (if the end is closed without any extra mountings) which reflects the shock which travels towards the driver section at a different velocity creating a stagnant gas region closed to the end wall (section 5). The velocity there is nearly zero, but the temperature of the gas increases manyfold. Therefore, this is one of the regions of interest inside the shock tube for many researchers as it can act as a momentary constant temperature reservoir (Anderson, 1990). To record the flow phenomena, the test facilities are equipped with high-frequency pressure transducers. However, to capture the heat flux parameter, the available sensors are

very limited. In fact, many of the sensors are dependent on the temperature signals for the estimation of heat flux.

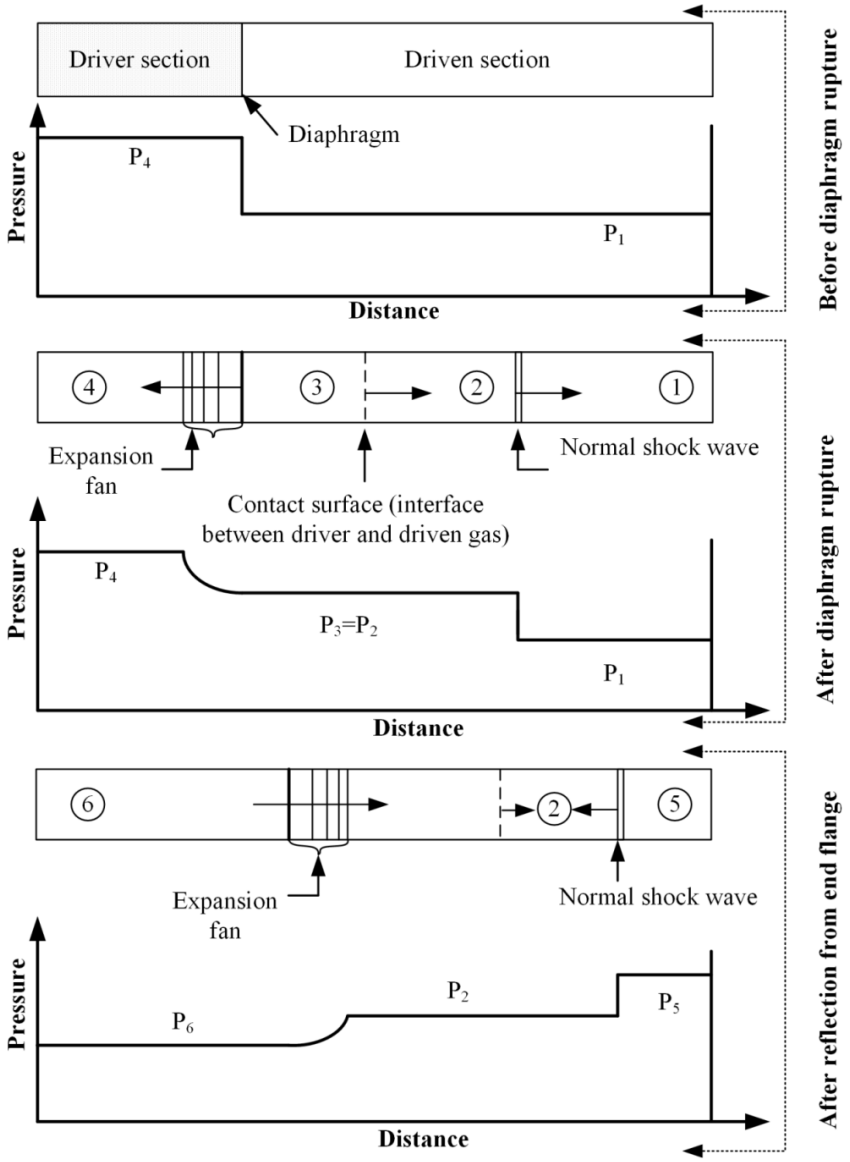

Fig. 5. 1: Pressure variations along the length of a shock tube

Like pressure transducers, these thermal probes also need to be very fast in responding to the high-speed flow phenomena, and very few sensors are capable of it. Amongst the available sensors, thin-film gauges (TFGs) are the widely used ones. Therefore, in the present experiment, the response characteristics of the in-house fabricated CTP is tested and compared with the pressure transducer and TFG in a shock tube. Therefore, it can be concluded that the shock tube is a handy device that has applications in different research

domains like high-temperature gas dynamics, fuel characterization, testing of supersonic entry vehicles, etc. It is very helpful in replicating high enthalpy, and high density flows for a short duration.

5.2 Shock tube facility at IIT Guwahati

The shock tube facility (at Indian Institute of Technology Guwahati – IITG) has a 2 m long driver section and 5 m long driven section made out of stainless steel tube with 77 mm outer diameter and 55 mm inner diameter. Total 7 tubes each tube is of 1m length are clubbed together to perform the task (**Fig. 5. 2**). Deliberately the driven section is made longer than the driver section to ensure the proper generation of the incident planar shock wave (**Fig. 5.3**). The driver and driven section is separated by an aluminum diaphragm of 1.2 mm thickness; however, grooving is done on 1/3rd of the diaphragm thickness for having controlled rupture (Kumar et al., 2014)(**Fig. 5. 4**).

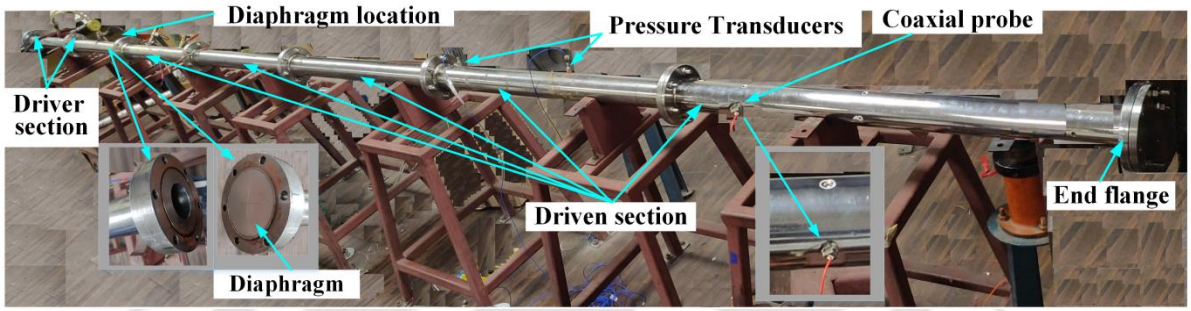

Fig. 5. 2: Photograph of the shock tube assembly at IIT Guwahati

During normal operation of the shock tube, the high-pressure section is continuously filled with nitrogen or helium until the diaphragm ruptures. A digital pressure gauge has been installed in this section to measure bursting pressure (p_4).There is a provision to maintain the driven section at a low pressure so that a substantial pressure difference can be created between "p_4" and "p_1". Rotary type vacuum pump (Make: HHV Pumps Private Ltd) is connected in the driven section to generate low pressure which is monitored by a vacuum gauge (**Fig. 5.3**). The driven section is filled with test gas viz. air maintained at low pressure (p_1). Due to pressure difference across the two sections, abrupt rupturing of the diaphragm occurs, resulting in the formation of compression waves which then coalesce to form a strong

shock front that propagates towards the driven section. As explained previously, it induces a slug of mass moving at high velocity and following the shock wave. As a result, a sudden rise in pressure and temperature is encountered by this induced mass.

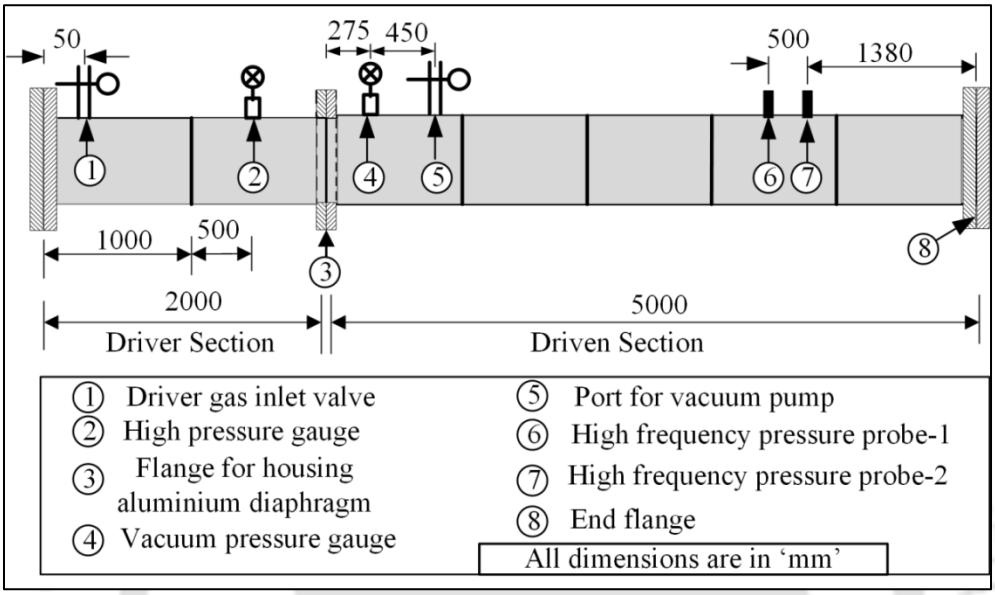

Fig. 5.3: Instrumentation of shock tube facility

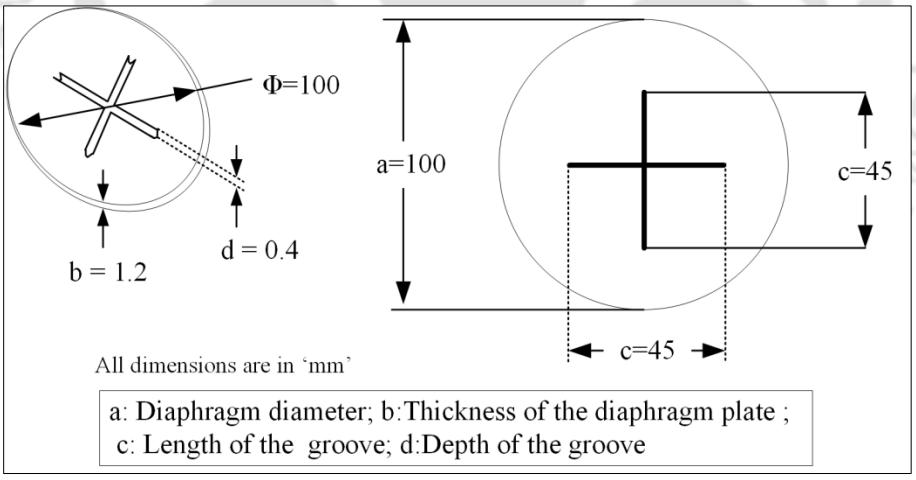

Fig. 5. 4: Metallic diaphragm design for shock tube operation

After reflection from the end flange, the backward motion of the shock wave further increases the pressure (p_5) and temperature of the induced mass. During reversal of shock wave at the end flange, the induced mass happens to stationary for a very short time and can be considered as "temporary high-temperature source" of stagnation mass of very high

density. The entire flow phenomena are complete within a test time window of 2 ms. Under this flow environment, it is proposed to evaluate the performance characteristics of the CTP. Before doing the experiments, the shock tube is calibrated, and the shock Mach number value is calculated analytically as well as from the experiment. These experimentally obtained parameters can be further validated by comparing the flow properties with 1-D theoretical relation, based on multiple gas dynamics, namely "Rankine-Hugoniot relation"(Anderson, 1990). Further, incident shock Mach number (M_{sh}) is calculated from a known distance (l) between pressure transducers PP-1 and PP-2 and time taken by the shock wave (Δt) to travel the same distance using Eq. 5.1.

$$u_{sh} = \frac{l}{\Delta t}; \quad a_1 = \sqrt{\gamma G T_1}; \quad M_{sh} = \frac{u_{sh}}{a_1} \tag{5.1}$$

Where, $u_{sh}, a_1, \gamma, G, T_1$ are the shock wave velocity, speed of sound, specific heat ratio, characteristic gas constant, temperature of the driven section, respectively. The detailed calibration procedure for the IITG shock tube is given in the literature (Nanda et al., 2017).

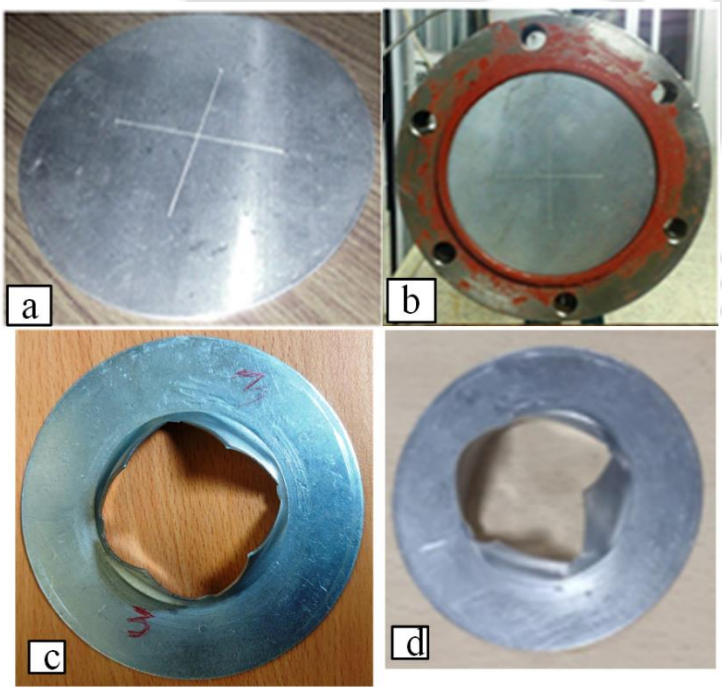

Fig. 5.5: Diaphragm rupture process

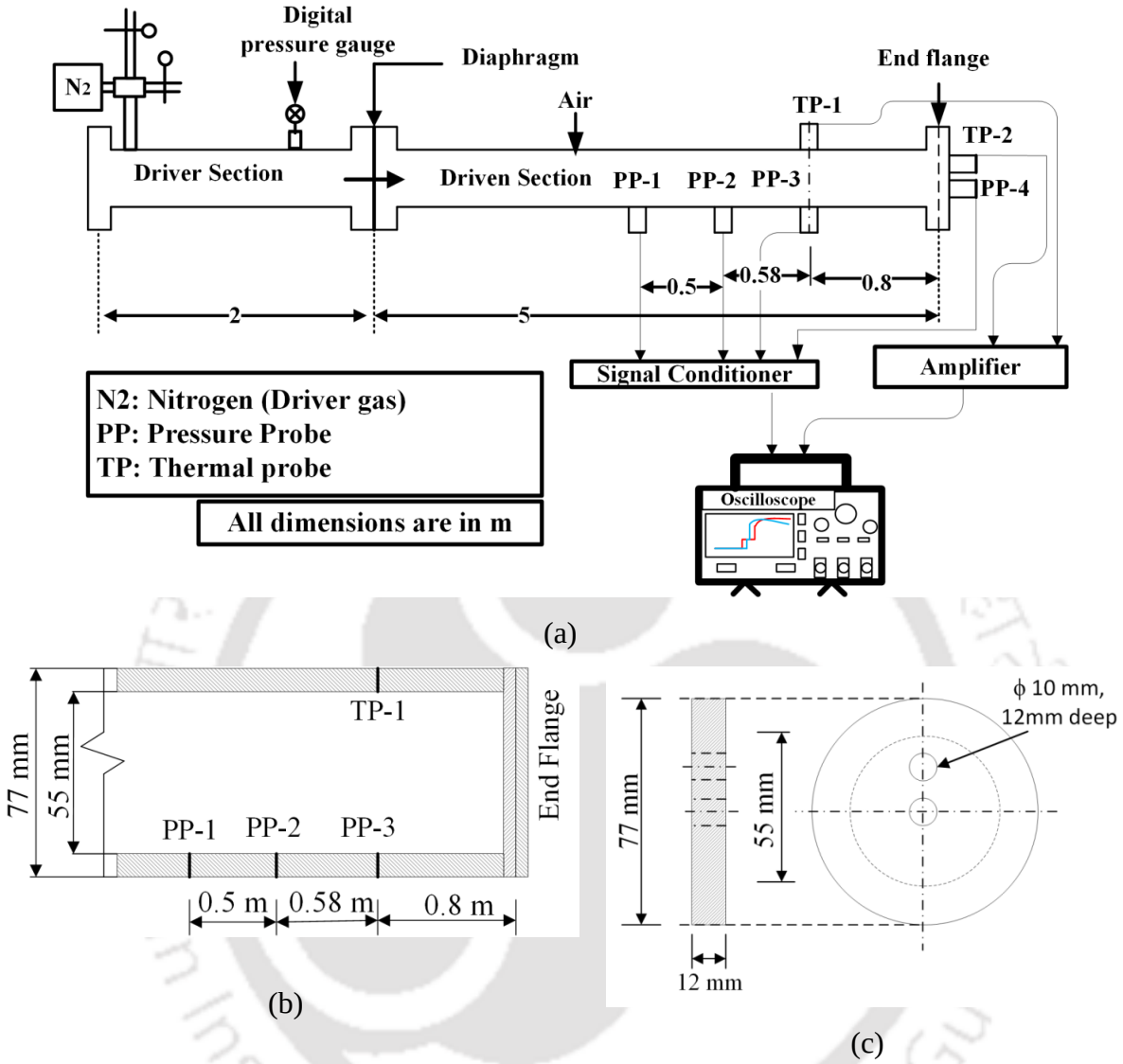

Fig. 5.6: Experimental arrangement in shock tube: (a) Schematic diagram; (b) Mounting arrangement for pressure and temperature probes; (c) End-flange instrumentation.

5.2.1 Test section instrumentation and experimental arrangement

The response to the shock wave can be captured with the help of fast response sensors located along the wall of the shock tube. However, it is mostly obtained by putting the sensors in the test section of the shock tube meant for obtaining of various parameters such as pressure and temperature etc (**Fig. 5.6 (a)**). The test section under focus is located towards the end of the driven section as shown in **Fig. 5.6 (b).** It is instrumented with four piezo-electric pressure transducers (Make: PCB piezotronics Inc. USA, Model: 113B22) at four

different axial locations along the tube wall. The transient pressure rise across primary and reflected shock are measured at two independent locations (1.88 m and 1.38 m from the end flange) by two pressure transducers PP-1 and PP-2 **(Fig. 5.6(b))**. One of the in-house fabricated CTP (TP-1) is mounted at a distance of 0.8 m from the end flange to capture the static temperature history for the shock flow. The third pressure transducer (PP-3) is mounted opposite to the TP-1 so that both the sensors face each other. It ultimately helps to have a similar flow environment at that cross-section of the shock tube. During the reflection of primary shock at the end of the shock tube, the test gas (air) in the driven section of the shock tube momentarily comes to rest and is considered a hot reservoir for a short time. In order to capture this transient flow information of the stagnant air, a specially designed end flange has been incorporated (**Fig. 5.6(c)).** The fourth pressure transducer (PP-4) is mounted along with another similar CTP (TP-2) at the end flange of the driven tube. Hence, both the probes (PP-4 & TP-2) may be considered as "stagnation probes." Adequate care has been taken for flush mounting of the sensors with the contour of the inner driven section approximating an undisturbed flow. In order to record the pressure and temperature data, an oscilloscope (Model: MDO3024, Make: Tektronix, USA) with a sampling rate of 2.5 GS/s via signal conditioner and amplifier has been incorporated.

5.2.2 Transient temperature measurements from coaxial thermal probe

In the design phase of CTP, one of the important intentions is the exposure of the probe in a real-time high enthalpy and high-density flow environment. In the shock tube, the primary shock generated at the diaphragm location and the reflected shock from the end flange creates a very hostile environment of high temperature and pressure for a very short test duration (~1 ms). The induced compressed air in the driven section of the shock tube remains stationary for this time and is considered as a momentary hot reservoir. Thus, the alignment and locations of CTPs in the shock tube (**Fig. 5.6(a))** resembles a flow field such that TP-1 experiences static heat flux rise while TP-2 experiences a rise in stagnation heat flux. For a particular flow condition, the response from both the probes can be compared with the data from pressure transducers, as shown in **Fig. 5.7**.

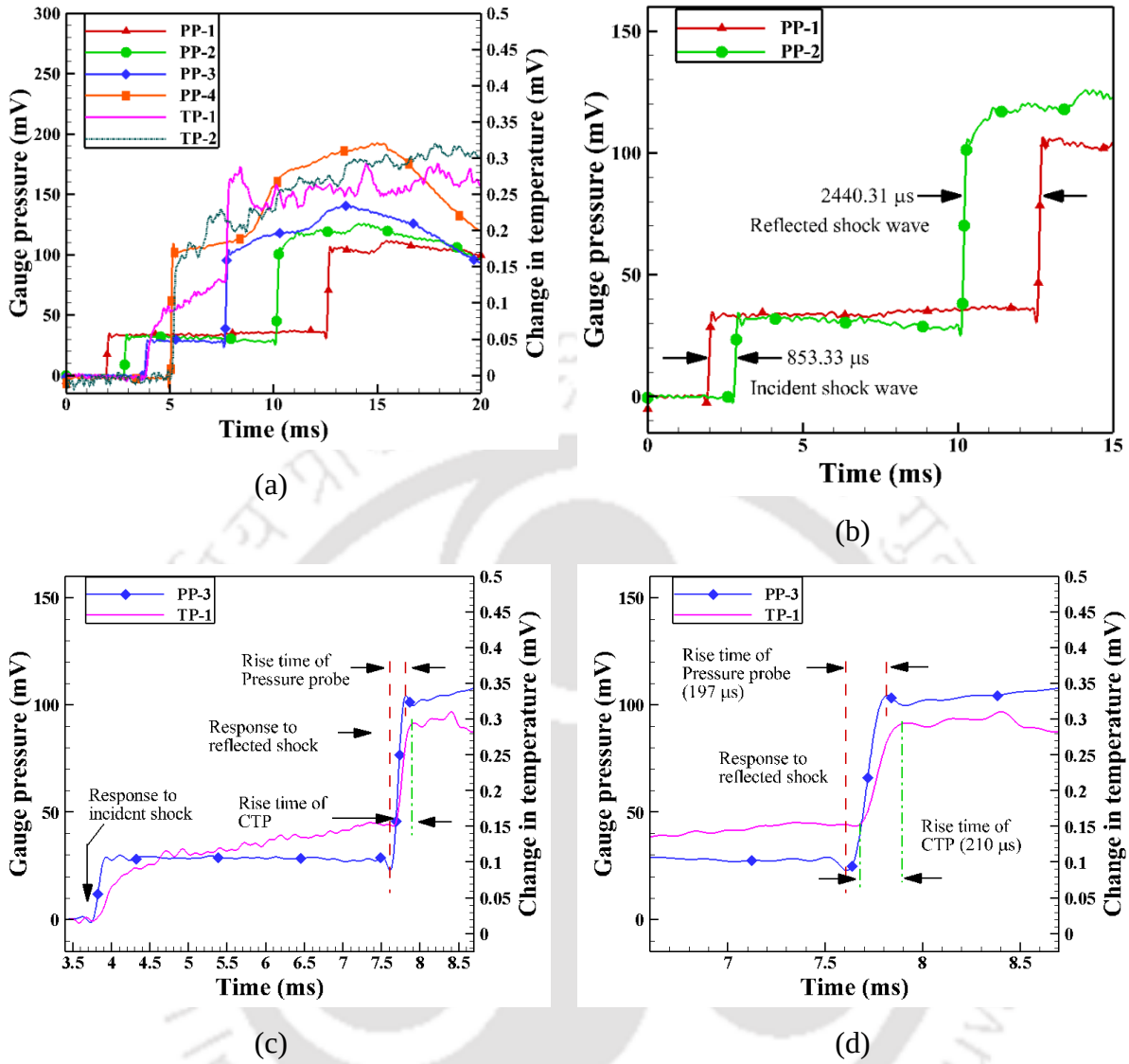

Fig. 5.7: Response characteristics of CTP for shock tube flow: (a) Superimposed pressure and temperature signals; (b) Typical voltage-time histories for measuring pressure jumps across primary and reflected shock; (c) Response of CTP with respect to primary and reflected shock; (d) Enlarged view of signals indicating the phenomena of reflected shock.

The prediction of effectiveness and performance of the CTPs are inferred from **Fig. 5.7**. With the instantaneous rupture of the diaphragm at the interface of the driver and driven section of the shock tube, the generated shock wave travels at supersonic speed towards the end of the driven section, followed by induced mass. The entire flow features experienced by different sensors (4 pressure transducers and 2 CTPs) in a single frame are captured as voltage signals (**Fig. 5.7(a)).** The flow phenomena include rising pressure and temperatures

across primary and reflected shocks. In the first instance, the instantaneous pressure rise across primary shock is immediately seen for PP-1 located at 1880 mm from the end flange. With the passage of time, a similar pressure rise is also observed from the other two pressure transducers (PP-2 & PP-3) mounted at different locations downstream of the shock tube. The step rise in static pressure values $(p_2 - p_1)$ amounts to 2.38 bar that remains steady for 10.635 ms, 7.342 ms, 3.879 ms evident from signals of PP-1, PP-2, and PP-3, respectively. As expected, the steady region is highest for PP-1 and is lowest for PP-3. The typical voltage-time histories for measuring pressure jump across primary and reflected shock (**Table 5.1**) are shown in **Fig. 5.7 (b)**. In this period, the thermal probe (TP-1) responds instantly in line with the pressure probe (PP-3). It shows parabolic rise, which is the characteristic nature of response corresponding to step heat load (**Fig. 5.7(c)).** The flow phenomena in the next event (after 1.234 ms) happen to be a rise in pressures and temperatures across in the reflected shock for which the "induced mass" is already at elevated pressures and temperatures (**Fig. 5.7(a)).**

Referring to the pressure trends, a step rise in static pressure values $(p_5 - p_1)$ after the reflected shock amounts to 7.48 bar. However, there is not any distinct evidence of steady region except for PP-1, which is about 2.38 ms. After this event, the slug of induced mass gets concentrated in the end flange and hence considered as momentary high pressure and temperature reservoir. So, the information inferred from the PP-4 and TP-2 mounted on the end flange would indicate the stagnation values of the flow field. It is interesting to note that the reflected shock wave phenomena captured by TP-1 in line with PP-3 indicate the fast response characteristics of the CTP. It may be highlighted here that the nature of the response from pressure sensors and thermal probes are different, which is clearly visible from the plot. The response of a pressure probe is 'step' in nature, whereas; the response from the thermal probe is 'parabolic,' which is in accordance with the basic heat transfer philosophy. Therefore, justifying the characteristics, the thermal probe (TP-1) shows a parabolic response when subjected to the shock flow. Before attaining the steady-state, it is imposed upon the reflected shock wave, which is responded to by the sensor. In a similar sense, the thermal probe (TP-2) also responds at the end flange along with the pressure transducer (PP-4). After

reaching the end flange, the shock wave reflects and moves back towards the driver section, which is again captured by the pressure sensors as a form of step response (**Fig. 5.7(d)).** The calculated response time for CTP (TP-1) is 210 μs in comparison with the response time of the standard pressure sensor, whose response time was 197 μs. The strength of the shock wave depends on the pressure ratio of the driver and driven section. In the present case, the driven section is at ambient pressure, which leads to the generation of a low strength shock wave and hence a slow response time. The response times for CTPs are expected to be faster for strong shocks when they are incorporated in shock tunnels (Desikan et al., 2016).

Table 5.1: Shock tube operating parameters with Nitrogen as driver gas.

Driver/Driven gas	Nitrogen/Air
Diaphragm rupture pressure (p_4) (bar)	13.5 ± 2
Shock Mach number (M_{sh})	1.7 ± 0.02
Induced mass velocity (m/s)	585 ± 10
Flow conditions across primary shock	$p_2 = 3.37$ bar ; $T_2 = 436$ K ; $\rho_2 = 2.56$ kg/m^3
Flow conditions across reflected shock	$p_5 = 8.48$ bar ; $T_5 = 592$ K ; $\rho_5 = 5$ kg/m^3

5.2.3 Surface heat flux estimation from temperature histories

In the shock tube experiment, there are two thermal probes (TP-1 & TP-2) that essentially measure the transient rise in static and stagnation temperatures, as shown in **Fig. 5.8(a)** . In the first conventional approach, the surface heat flux $(\dot{q}_a)$ is recovered through analytical one-dimensional heat conduction modeling. The other independent approach is to consider the temperature responses (**Fig. 5.8(a))** as an input for numerical simulation modeling (ANSYS) and subsequently recover surface heat fluxes $(\dot{q}_{nu})$.

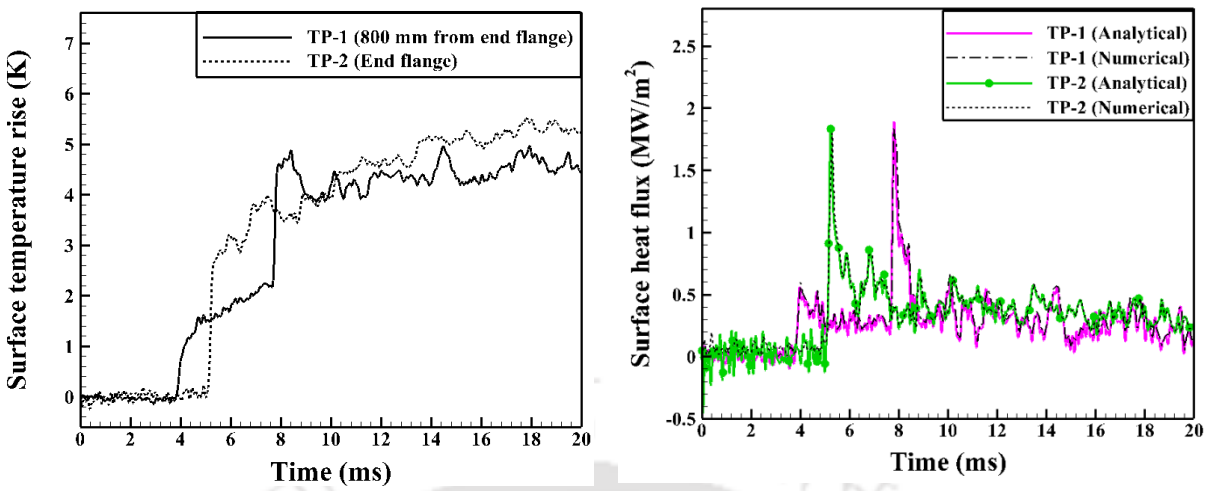

(a) (b)

Fig. 5.8: Time histories from thermal probes during shock tube experiments: (a) Measured transient temperatures; (b) Estimated surface heat fluxes.

With reference to shock-tube flow analysis, there is a sudden rise in temperature and pressure due to compression following the Rankine-Hugoniot equation (Anderson, 1990; Sahoo, 2007). The interpretation of the absolute value of this temperature rise is not justified in this case because the phenomenon is transient, and the heated air remains in contact with the probe for a short duration. Moreover, there is a significant difference in the thermal product (β) values between the sensing surface of the probe and that of heated air in the driven section of the shock tube. But, the very basic fact is the response behavior of the probe with respect to flow characteristics prevailing in the shock tube. Referring temperature response of TP-1 (**Fig. 5.8(a)),** it reveals the fact that maximum change in surface temperature (~ 5 K) occurs within a 3.93 ms time scale. The rise in temperature is gradual (seen as parabolic rise) for TP-1 initially for primary shock, followed by a sharp rise due to reflected shock phenomena for the test domain (3.93 ms) under consideration. The effect can be visualized from the surface heat flux $\{(\dot{q}_a)_{TP1}\}$ plot derived from the surface temperature history of TP-1. There are two distinct peaks shown in **Fig. 5.8(b).** The indication of the first peak refers to the fact that the primary shock wave has heated the air to a higher temperature, while the second peak refers to the reflected shock wave that has further elevated the temperature of the air. Subsequently, the surface temperatures appear to be steady after the strengths of primary and reflected shock become weak. This is exactly predicted when the surface heat

flux $\{(\dot{q}_{nu})_{TP1}\}$ is recovered independently through a numerical simulation from the transient temperature signals of TP-1 and is compared in **Fig. 5.8(b)**. In any case, the surface heat flux history predicted from measured signals of TP-1 and through numerical simulation almost exactly matches with a peak heat flux of 1.8 ± 0.05 MW/m^2 occurring after the reflection of the shock wave from the end-flange.

In the case of CTP mounted on the end flange (TP-2), different nature of the response is observed with respect to the rise of surface temperature. The maximum rise in temperature (~ 5 K) is the same as in the case of TP-2 with a single rise in temperature. The other important observation is a sharp rise in the temperature signal of TP-2 as compared to TP-1 since TP-2 is mounted in the end-flange and experiences high-temperature stagnant gas-induced through reflected shock. The arrival of primary shock essentially heated the air, and the entire slug air becomes stagnant that replicate an environment of short-duration high-temperature reservoir. After the reflection of the shock wave from the end flange, there is an instantaneous rise in temperature, as seen from **Fig. 5.8(a).** Hence, there is no evidence of primary shock in the response behavior of TP-2. This is again justified when it is compared with the response of the pressure transducer (PP-4) mounted in the end flange (**Fig. 5.7(a)**). With these transient surface temperatures, the stagnation heat flux has been computed through analytical modeling $\{(\dot{q}_a)_{TP2}\}$ (via Eq. 2.7) and numerical simulation $\{(\dot{q}_{nu})_{TP2}\}$. The estimation of stagnation heat flux histories is seen to be accurate from the above two independent predictions.

When the comparison of surface heat flux is made between the two probes (TP-1 & TP-2) in **Fig. 5.8(b),** the agreement is very good with reasonable accuracy of 2.34%. The peak heat flux (1.85 MW/m^2) value registered at 5.23 ms is nearly the same as measured by the static probe at 7.8 ms. Beyond 8.5 ms, the responses of both the probes are similar with a time-averaged value of stagnation heat fluxes in the range 0.32-0.35 MW/m^2. As discussed earlier, TP-1 is mounted very close to the end flange (800 mm). At very high speed (~ 586 m/s) of slug mass, there is a resemblance of time average values of stagnation heat flux even though TP-1 is regarded as a static thermal probe. In a nutshell, both the probes prove the

ability to capture the entire event of highly transient phenomena of high enthalpy and high-density flow features prevailing in the shock tube.

5.3 Comparison of the response of coaxial thermal probe with a silver thin film gauge

The detailed study for the short-duration experiments has been elaborated in the previous sections. The CTP has been successfully implemented to capture the shock wave phenomena in a shock tube. The response obtained from the probe is quite encouraging and acceptable. However, this fact needs to be reassured by accessing the closeness of the probe towards a standard reference probe. Most of the literature highlight the use of TFGs (preferably platinum thin-film gauges) for shock tunnel applications. Therefore, in the current experiment, it is planned to put the in-house fabricated CTP along with a TFG in a similar flow environment in the shock tube experiment (**Fig. 5.9**). In this approach, it is observed that the cost of platinum film material is very high. In lieu of it, less costly, highly conductive silver can be used for such applications whose application is also less addressed for shock tube flows. Similarly, there is limited literature that explains the usage of CTPs in shock tunnel applications. The relative merits and demerits of both the probes have been elaborated in Chapter 1. Having certain advantages of CTPs over TFGs counterparts, it is desired to make an experimental assessment in a hostile flow environment using a shock tube. Hence, both the sensors are mounted on the specific locations on the test model to infer temperature history during test flow duration.

Reference probe

Thin-film gauges are used predominantly for short-duration impulsive aerodynamic studies by several researchers due to their fast response behavior. The TFGs are prepared by placing a thin layer (~ few microns) of highly conductive material (gold, silver, platinum, nickel, etc.) on a non-conducting substrate (pyrex, quartz, etc.).

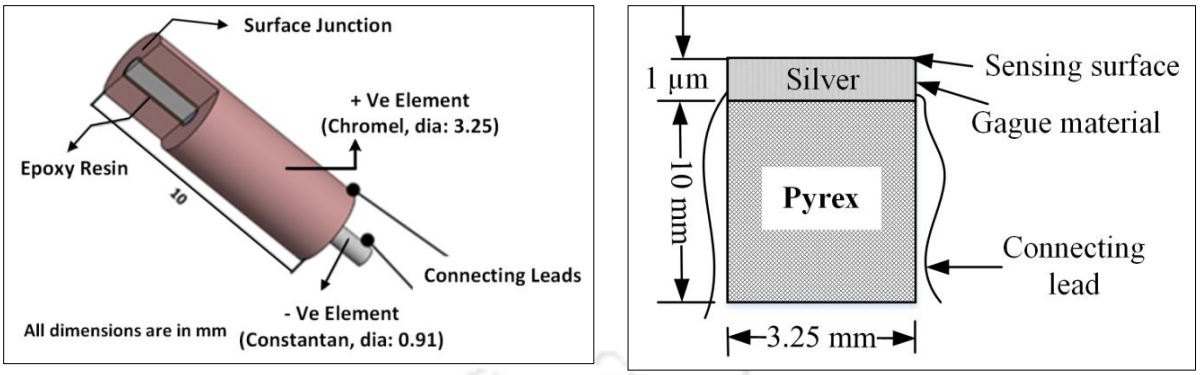

(a) (b)

Fig. 5.9: Schematic representation of thermal sensors: (a) Coaxial thermal probe; (b) Thin film gauge.

The conductive layer is deposited over the substrate either through hand panting, sputtering, or vacuum deposition, which is in general fragile in nature due to weak bonding between metal and insulator. In this investigation, an in-house fabricated thin-film gauge made out of silver is used as a reference gauge for the shock tube study. The thin film gauge works on the principle of change in resistance of a thin layer metal film on an insulating substrate due to a change in temperature. The TFGs being passive in nature, the film is supplied with an external power supply using a constant current source where, the change in voltage is measured as an output, due to change in resistance of the film subjected to change in temperature (Jadhav et al., 2020; Sarma, 2017). The insulating substrate materials such as quartz, pyrex, and macor are preferred for the fabrication of TFGs. In the present case, pyrex is chosen as a substrate material due to minimal change in thermophysical properties in the operational temperature range. One of the faces of the pyrex (3.25mm diameter and 10mm length) is flattened with the help of abrasive water paper of different grit sizes (300, 600, followed by 2000) and cleaned in the magnetic stirrer properly to avoid deposition of foreign particles. The material is then cleaned and dried in a dust-free environment. The silver conductive paint (SPI supplies, USA) is deposited on the pre-processed surface of Pyrex with the help of a fine brush. The thin layer of film is allowed to dry at room temperature and then placed in the furnace at 350ºC for nearly 15 min for evaporation of additives, leaving behind only the residue of silver. The sensor is cooled gradually to avoid any formation of cracks due to thermal shock. The film resistance is checked (and a double coat can be painted if

required) till the desired resistance (10-100 Ω) is achieved. Two connecting leads are drawn from two sides of the sensor for data acquisition purposes, leaving the sensing surface unaffected. More details can be found in reference (Sarma, 2017). The schematic of the probe is presented in **Fig. 5.9(b).**

The required parameters for heat flux modeling are the temperature history $\left[T_s(\tau)\right]$. However, the temperature is not the immediate output from the measurement; rather it needs to be calculated from the voltage output by the knowledge of temperature coefficient of resistance (TCR) through Eq. 5.2. When a TFG is powered with initial source voltage (V_0) and exposed to a temperature difference (ΔT), then the change in output voltage (ΔV) can be related to TCR.

$$TCR = \frac{1}{V_0}\frac{\Delta V}{\Delta T} \quad \text{..... (5.2)}$$

By adopting the calibration procedure of TFG as reported in the literature, the measured values of TCR and thermal product of substrate (pyrex) are found as 1529.67 $J/m^2s^{0.5}K$ and 0.0025 K^{-1}, respectively (Sarma, 2017).

5.3.2 Experimentation in the shock tube

The experiment is planned to check the simultaneous response from both the probes (CTP and TFG) by exposing them to a similar flow environment. Here the testing is carried out by putting both the probes at the end flange to face a similar flow environment. The driver gas is changed from nitrogen to helium, the ratio of $\left(\frac{P_4}{P_1}\right)$ is increased by making the driven section vacuum with the help of a vacuum pump. Here, the response of the probe is compared with a standard reference gauge (TFG) along with a pressure probe. All these changes are made to assess the feasibility and response of the probe at different flow conditions to use the CTP as a heat flux probe. In this case, three piezoelectric pressure transducers (Make: PCB piezotronics Inc. USA, Model: 113B22) are mounted at certain fixed locations in the tube. The response to primary and reflected shock wave in the flow field inside the shock tube is

captured by two pressure transducers mounted along the tube wall at two independent locations; one at 885 mm from the end flange (PP-1) and another at 385mm from the end flange (PP-2) as mentioned in **Fig. 5.10.**

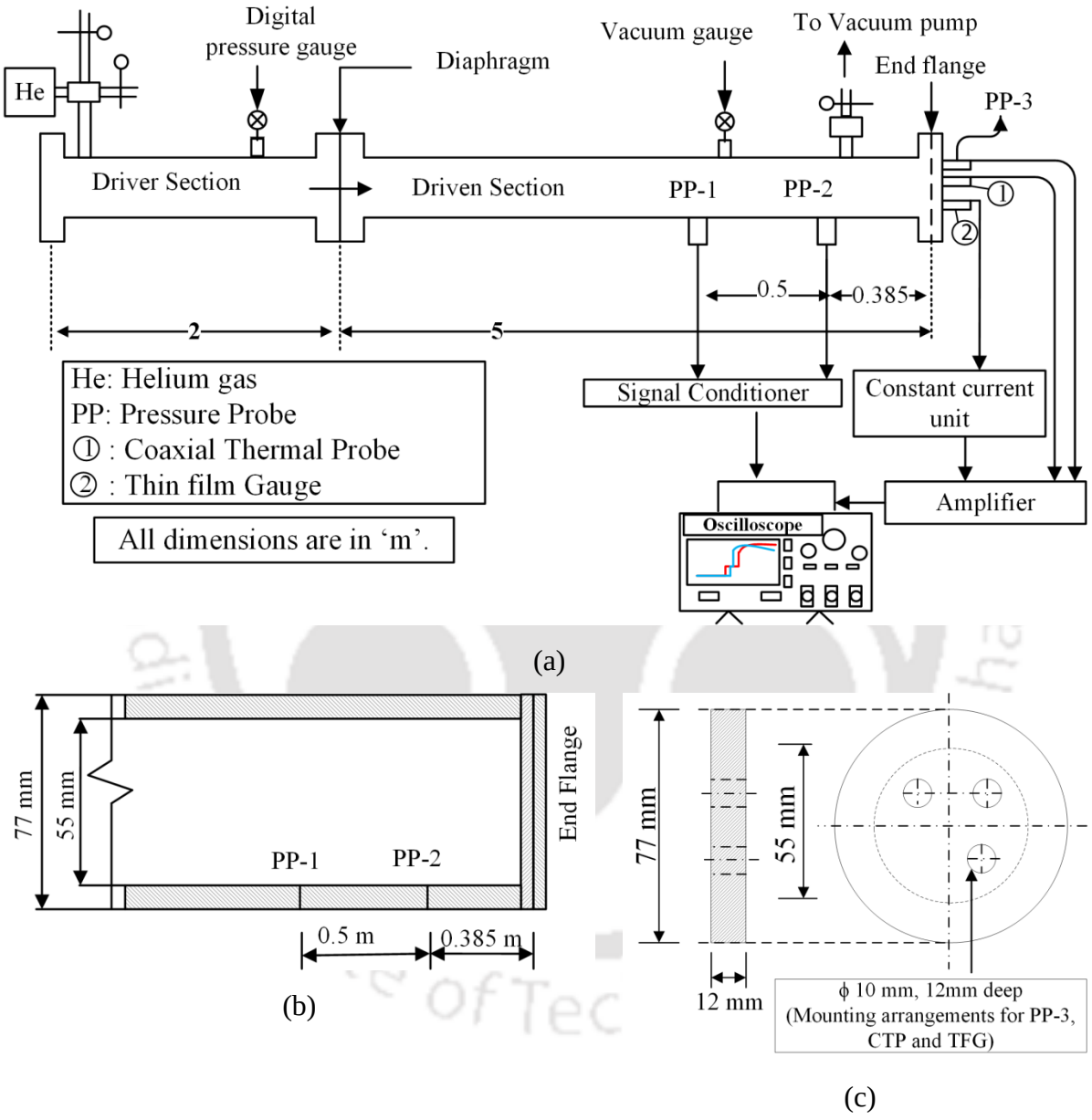

Fig. 5.10: Shock tube with experimental set up: (a) Schematic layout; (b) In-line mounting arrangement of the pressure transducers; (c) End flange mountings for sensors.

At the time of reflection of shock wave (from the end flange of the shock tube), the thermodynamic condition of the test gas (air) is equivalent to a hot reservoir for a short time duration due to momentary stagnant gas near the end flange. This region is termed as the region of instantaneous rise in pressure and temperature in the flow field. In order to capture the rise in temperature in the flow field, the designed thermal probes (CTP and TFG) are mounted in a specially prepared end flange (**Fig. 5.10** (c)). Another pressure transducer (PP-3) is placed along with both the thermal probes to capture the instantaneous rise in pressure. In fact, all the measuring devices at this location can be treated as "stagnation probes." All the probes are carefully flush-mounted facing the shock wave and are aligned in line with the inner driven section pertaining to an undisturbed flow. The constant current source is provided to the thin film gauge through a constant current source meter (Model: 2400-903-01, Keithley, USA). The voltage output is required to be amplified for the purpose of acquisition. Therefore, both CTP and TFG are channeled for acquisition through a voltage amplifier. Similarly, the piezo-pressure transducers are linked for acquisition via a signal conditioner. The data recording is carried out using an oscilloscope (Model: MDO3024, Make: Tektronix, USA) with a sampling rate of 2.5 GS/s. A sampling rate of 500000 S/s is used to capture the high-speed flow phenomena.

5.3.3 Transient temperature measurements

The probes (CTP and TFG) mounted at the end flange can capture the flow in such a harsh condition. The response from both the probes can be compared with the data from the pressure transducer. With the sudden rupture of the diaphragm at the interface of the driver and driven section (due to the pressure difference between the driver and driven) of the shock tube, the generated shock wave travels at supersonic speed (Mach 3.7) towards the end of the driven section followed by induced mass. The flow features in the form of pressure and temperature rise across the shock waves are captured by mounting them (three pressure transducers, one CTP, and one TFG) in the end flange of the shock tube.

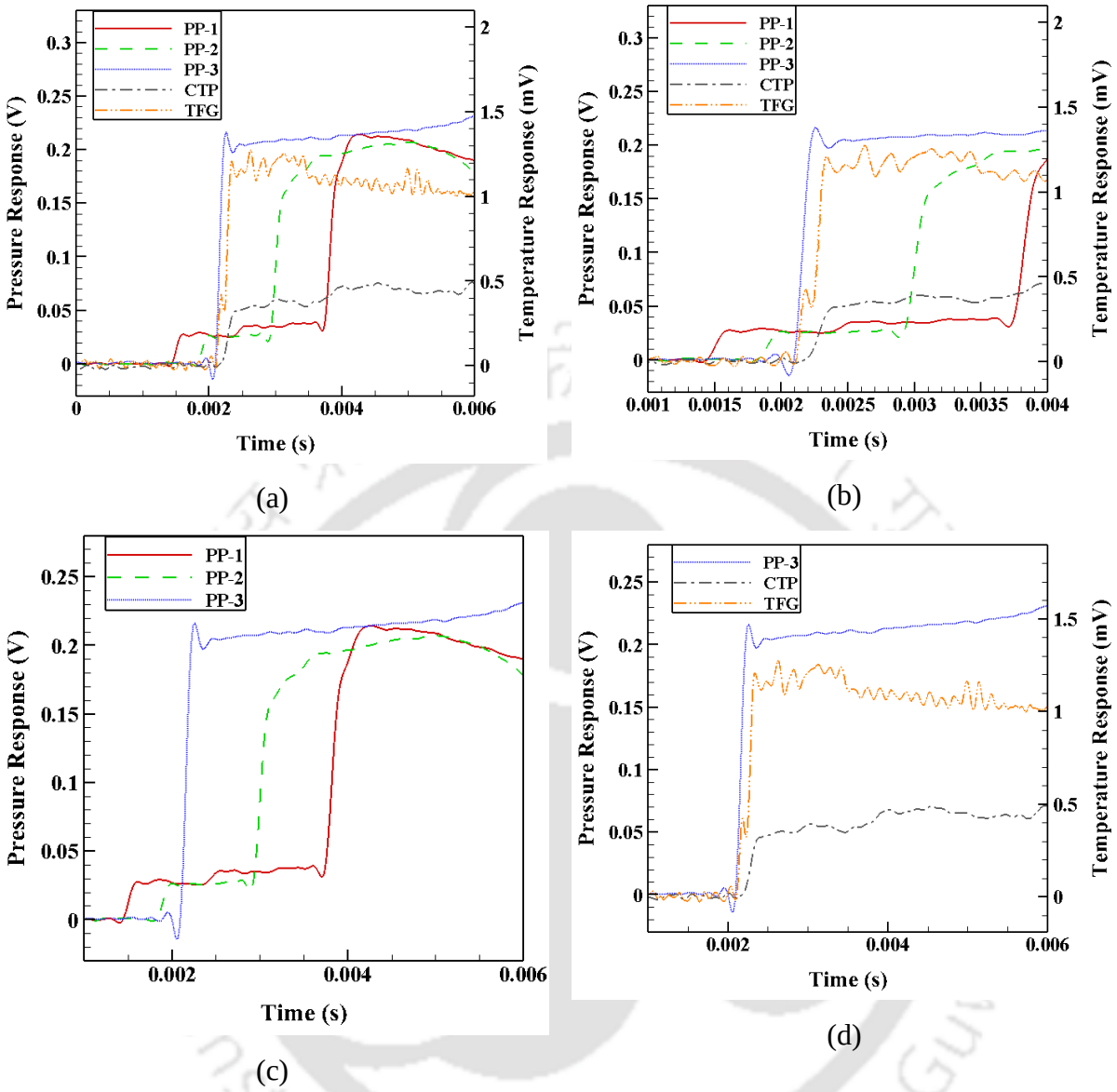

Fig. 5.11: Combined pressure and temperature traces for shock tube experiments: (a) Response plots for all probes and pressure transducers in a single frame; (b) Enlarged view of responses; (c) Responses of all the pressure transducers; (d) Pressure and temperature responses at the end flange.

The single-frame as voltage signals shown in **Fig. 5.11(a & b)** emphasizes the pressure rise across the primary shock and reflected shock as well as stagnation heat flux from thermal probes (CTP and TFG). While traveling towards the driven section, the pressure rise across primary shock is immediately perceived by PP-1 located at 885 mm from the end flange. A similar pressure rise is also experienced by PP-2 mounted at 385 mm from the end flange.

The step rise in static pressure values $(p_2 - p_1)$ amounts to 1.87 bar (**Fig. 5.11(b)).** The flow phenomenon in the next task (after 0.3 ms from PP-2) is to capture the pressure across reflected shock where the induced mass is already at elevated pressure and temperature.

A step rise in static pressure values $(p_5 - p_1)$ after the reflected shock amounts to 15.5 bar. While reflecting back from the end flange, the concentrated induced mass at the end flange behaves as a momentary reservoir of high pressure and high temperature. The flow information seen by the pressure transducer PP-3 (**Fig. 5.11(c)),** does not have pressure jump due to primary shock but due to reflected shock at the end flange. A step rise in static pressure values $(p_5 - p_1)$ after the reflected shock amounts to be higher by 0.5-1 bar from the other PP-1 & PP-2 during the experimental time scale of measurement (2ms). Following this event, almost steady pressure of 14.5 bar is seen, which can be argued as a high-pressure momentary reservoir for about 2 ms. Analogous to this event, similar response characteristics from CTP and TFG, when plotted along with PP-3 (**Fig. 5.11(d)).** However, the rise time for TFG is seen faster as compared to CTP. The rise time of CTP and TFG are found to be 265 μs and 240 μs, respectively. It may be emphasized that the piezoelectric nature of the pressure transducer shows a fast response with shock wave flow fields, which is followed by the TFG obeying almost a similar trend. Both of them (PP-3 and TFG) mimic a step response, whereas the CTP infers a parabolic rising trend with a ramp nature. However, both The PT-3 and TFG immediately attain a steady-state for 1.4 ms after the response, whereas the CTP shows a rising trend due to its thermal inertia effect for lumped heat conditions. Apart from this fact, the CTP has the ability to capture all the flow features. The strength of the shock wave depends on the pressure ratio of the driver and driven section. For the present case, the ratio is maintained at 112.5 ± 2%. The shock tube operating parameters are mentioned in **Table 5.2**.

5.3.4 Surface heat flux estimation from temperature histories

The two thermal probes (TFG and CTP) mounted at the end flange of the shock tube essentially capture the temperature history prevailing to the flows that are exposed to reflected shock. The time-dependent surface heat flux can be recovered from the transient

temperature history by modeling the sensor as a semi-infinite slab with one-dimensional heat conduction (**Fig. 5.12)**. It may be noted that in both the thermal sensors, the sensing surface is very thin, which is established on a substrate. The TFG has an insulator substrate, and that of CTP, the substrate is conductive in nature. Due to the small experimental time scale (~ 2ms), the penetration depth in both sensors is very small. Therefore, both the sensors can be assumed to obey the one-dimensional heat conduction principle (negligible lateral temperature variations) on a semi-infinite substrate. The analytical method of heat flux assessment is elaborated in Chapter 2.

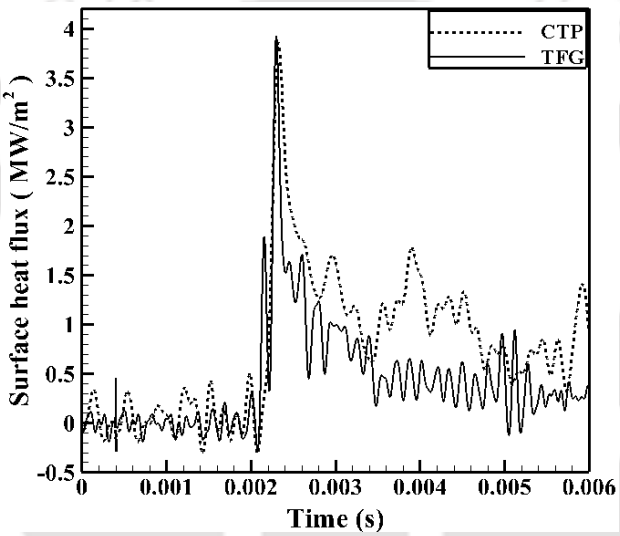

Fig. 5.12: Comparison of analytical heat flux for CTP and TFG

It may be highlighted that the trend of time-varying heat flux for both CTP and TFG are different in terms of rise and fall (**Fig. 5.13**). This may be due to the thermal inertia of the CTP, which intends the continuous rise in temperature and hence, the gradual fall in heat flux trend. In short, both the probes justify their capability to capture the event of highly transient phenomena of high enthalpy, and high-density flow features prevailing in the shock tube.

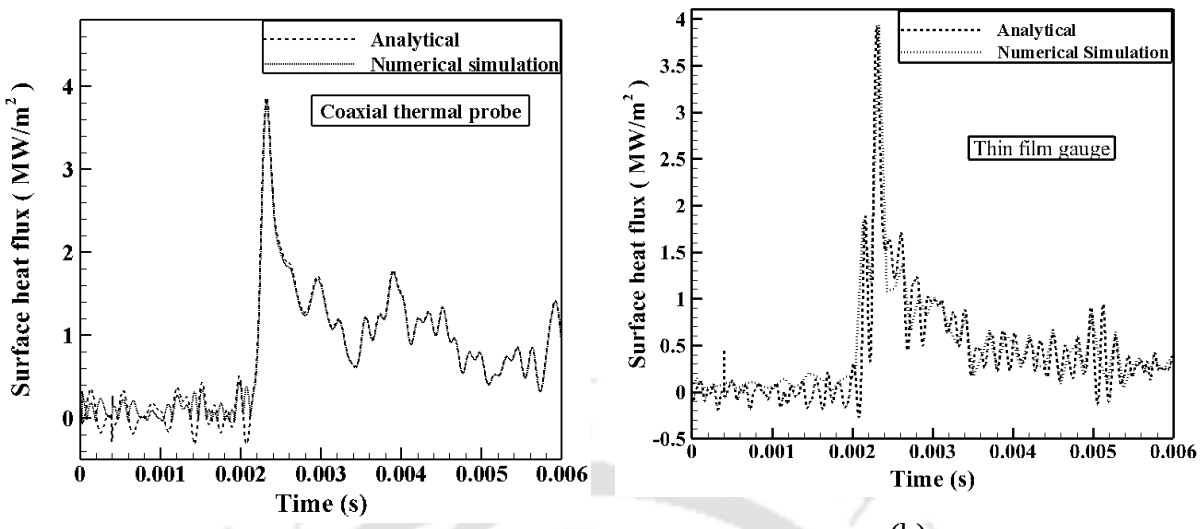

(a) (b)

Fig. 5.13: Validation of experimental heat flux trough numerical simulation: (a) CTP; (b) TFG.

5.3.5 Validation through numerical simulation

The recovery of surface heat flux $(\dot{q}_a)$ from transient temperature history through analytical modeling is found to have a nice agreement in terms of trend and magnitude for both the thermal probes. Subsequently, they are cross-verified through an independent approach using a numerical simulation modeling with experimental temperature response as input and computing the corresponding surface heat fluxes $(\dot{q}_{nu})$. ANSYS transient thermal module is used for the simulation work. The domain for the computational study is shown in **Fig. 5.14** comprises the schematic and boundary conditions for 2D numerical simulation. The size of an element is chosen by considering the requirement of an adequate number of elements for sensing surface (few micron thicknesses). The dimensions for the computational study replicate the original sensor size, while the thermal properties for different materials used for simulation are listed in **Table 2.1**. The ANSYS transient thermal module flow solver is utilized for the complete simulation process. A separate grid independent study has been performed for both the sensors to find out the mesh dependency with three different node combinations for CTP (102646,111313 and 120441) and TFG (60105, 67615, and 237386). A careful meshing is required for the TFG due to the very small size of the sensing element (1 μm) compared to its substrate (10 mm) for which a combination of mesh size of 0.5 μm,

0.4 μm, and 0.2 μm for sensing surface (silver) are examined (**Fig. 5.14**). The results are consistent and independent of the mesh size. As the time required for simulation is not at the high end, the finer mesh size is repeated for further study, keeping in view the accuracy of the result.

A composite computational domain is used for CFD simulations. The computational domain for the CTP (**Fig. 5.14 (a))** consists of different materials (chromel, constantan, and insulation). Unlikely, the computational domain for TFG consists of two materials, viz. top sensing material and bottom backing material (**Fig. 5.14 (b)).** The corresponding material properties are assigned to the respective materials (**Table 2.1**). The boundary opposite to the sensing surface is treated as an isothermal boundary, and it is maintained at ambient temperature (25ºC). The other outer boundary surfaces are imposed with adiabatic wall boundary conditions. However solid-solid interface boundaries between two different matrices are considered to have continuity in heat flux and same temperature. The sensing junction is imposed with a boundary condition of uniform and time-varying experimental temperature from the shock tube. The whole computational domain is initialized with room temperature (25ºC).

Referring to **Fig. 5.13**, the peak heat flux is observed for both signals at 2.3 ms for CTP. The peak heat flux $\left\{\left(\dot{q}_a\right)_{\text{CTP}}\right\}$ for analytical modeling is noted as 3.85 MW/m^2 against a numerical prediction $\left\{\left(\dot{q}_n\right)_{\text{CTP}}\right\}$ of 3.80 MW/m^2. Since the CTP is located at the end flange, it may be interpreted that the peak stagnation heat flux predicted through the experiment has a nominal deviation of ± 1.5% from the numerical computation. In a similar sense, the peak heat flux of TFG, evaluated through numerical simulation, $\left\{\left(\dot{q}_n\right)_{\text{TFG}}\right\}$ is 3.90 MW/m^2 against the analytical value $\left\{\left(\dot{q}_a\right)_{\text{TFG}}\right\}$ of 3.92 MW/m^2 within an accuracy range of ± 1.5% (**Fig. 5.13**). The comparative estimate of peak surface heat flux value through numerical simulation bears a very good agreement with the analytical heat flux value as mentioned in

Table 5.3. The uncertainties associated with the measurements using CTP have been discussed in Appendix A in detail using the approach given in the literature (Moffat, 1985; Moffat, 1988).

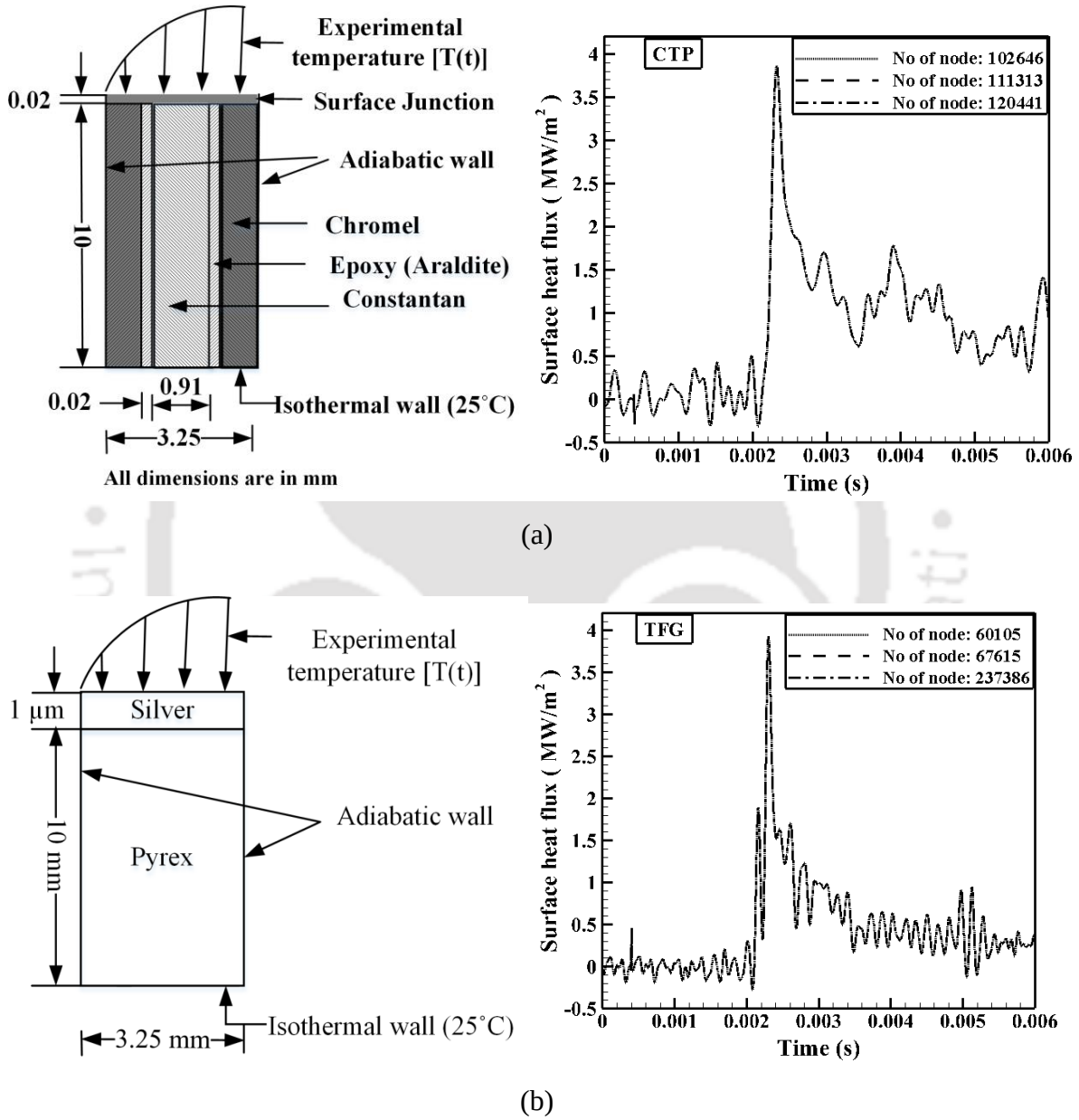

Fig. 5.14: Computational domain and grid-independent study for numerical simulation: (a) CTP; (b) TFG.

Table 5.2: Shock tube operating parameters with helium as driver gas.

Driver/Driven gas	Helium/Air
Diaphragm rupture pressure (p_4) (bar)	17.2 ± 1.4
Shock Mach number (M_{sh})	3.7 ± 0.02
Induced mass velocity (m/s)	1285 ± 10
Pressure jump across primary shock (p_2), (bar)	1.87
Pressure jump across reflected shock (p_5), (bar)	15.5

Table 5.3: Comparison of heat flux values

Type of gauge/Heat flux estimated method	Analytical heat flux $(\dot{q}_a)$ (MW/m^2)	Numerical heat flux $(\dot{q}_{nu})$ (MW/m^2)	Prediction accuracy $\frac{(\dot{q}_a)-(\dot{q}_{nu})}{(\dot{q}_a)}\times 100$
CTP	3.86 ± 3%	3.79 ± 3%	± 1.5%
TFG	3.92 ± 5%	3.90 ± 10%	± 0.5%
Prediction accuracy $\frac{(\dot{q}_a)_{\text{TFG}}-(\dot{q}_a)_{\text{CTP}}}{(\dot{q}_a)_{\text{TFG}}}\times 100$	± 1.5 %	± 2.8 %	Maximum deviation ± 2.8 %

5.4 Summary

The CTP has been successfully tested in the shock tube, and the response has been captured. The response characteristic of the CTP is compared with the standard pressure transducer and a thin film gauge. CTP is placed in the driven section of the shock tube opposite to the pressure probe, and response from both the probes has been compared. Similarly, the response of CTP is compared with TFG by putting both at the end flange of the shock tube. In all the cases, the heat flux data is recovered using the analytical method as well as numerical simulation, and the results are compared. The response of the CTP is found quite fast and can be utilized for shock tube flow diagnostics.

CHAPTER 6

Coaxial thermal probe for cyclic thermal load applications

Overview

As observed from the previous chapters, the coaxial thermal probes have the ability to capture short duration transient temperature signals. The fast response characteristics of the in-house fabricated coaxial thermal probe have been well addressed in the previous chapter through shock tube experimentation. The intention was focused on measuring transient temperature signal and estimation of heat flux through appropriate modeling. In the present chapter, the fast response of the thermal probe has been utilized to capture transient temperature response in the exhaust of an internal combustion engine. The main intention is to utilize the fast response characteristics of the probe to capture the cyclic heat load in an internal combustion (IC) engine. In line with this idea, the temperature of the gas from the engine exhaust is recorded. By analyzing the temperature signal, the cycle time and indirectly the RPM of the engine is calculated. A high-temperature coaxial thermal probe (ht-CTP) is fabricated with high-temperature insulation (alumina based) so that it can sustain the exhaust gas temperature environment. A research engine set-up running in petrol mode is used for the study. The sensor is flush-mounted on the exhaust pipe at a distance of 20 mm from the exhaust manifold without disturbing the outlet gas flow. The transient temperature of the exhaust gas is recorded for each cycle of the engine. It may be noted that in a four-stroke engine, there is only one exhaust stroke in a complete cycle and the exhaust valve also opens once in a cycle. Hence, the time duration has been measured by measuring the consecutive temperature response, and the engine RPM has been calculated. The engine revolution is compared with the recorded value by the RPM sensor. Along with this, the initial temperature signal is processed for heat flux estimation through the analytical method that provides an estimate of the magnitude of instantaneous heat flux imparted on the sensor by the engine's exhaust gas.

6.1 Introduction

Transient temperature history plays a significant role in the design and performance of a thermal system. The present in-house fabricated probe (CTP) has fast response characteristics which are widely documented in the previous chapters. The application of these probes cannot be limited to the short duration flows rather; the fast response characteristics of the probe can be employed to measure temperature histories in many real-time environments. Few sensors have been employed to measure the surface temperature in internal combustion engines (Assanis and Badillo, 1989; Marr et al., 2010; Sumin, 2013). It may be noted here that, while utilizing this sensor as a "heat flux probe" (in case of short duration experiments), the time period of application imposes a restriction owing to the assumption of one-dimensional heat conduction on a semi-infinite substrate. Otherwise, the fast response characteristics of the probe can be utilized to capture many transient phenomena in the form of transient temperature history in case of short duration as well as continuous measurements. For the present experiment, the probe has been utilized to capture the transient temperature in the exhaust of an internal combustion engine. The exhaust valve of an internal combustion engine opens periodically after a certain interval of time corresponding to the engine speed. These probes (if mounted at any place in the exhaust line of the engine) can respond to the hot exhaust gas that goes outside through the exhaust manifold after the completion of the combustion process inside the engine cylinder. The time difference between the successive responses can be measured, and the cycle time corresponding to the engine RPM can be calculated. Therefore, the present chapter focus on the in-house fabrication of a high-temperature thermal probe (ht-CTP) for engine exhaust application, its calibration for high temperature, and its application in the engine exhaust to capture transient temperature. Subsequently, the information of cycle time is obtained from the temperature response and compared with the cycle time calculated using the value from the RPM sensor of the engine. The heat flux imparted on the sensor by the exhaust gas is also estimated using the analytical modeling of the sensor.

6.2 Fabrication of thermal probe for high temperature application

In order to study the response characteristics, a CTP has been fabricated on a laboratory scale from chromel and constantan. The fabrication process is similar to the probe used for shock tube application, as explained in Chapter 3. The only difference is the use of epoxy, which can sustain high temperatures so that the probe can be used in the exhaust of the IC engine. An alumina-based adhesive is used as insulating material which can sustain a temperature of 1500ºC. The expected temperature at the exhaust of the IC engine for the present experimental condition is nearly 400ºC, and an E-type probe can record a temperature up to 700ºC. Therefore, these probes can be used to capture the response confidently. As explained previously, the bare constantan element (0.91mm diameter, 15mm length) is placed coaxially and concentrically in the annulus made in Chromel element (3.25mm diameter, 10mm length) with a small insulation thickness in between them (~20µm). The insulation avoids an electrical connection between the two thermo-elements along the entire sensor length, leaving the sensing surface un-insulated. The connection between the two thermo-elements is created at the sensing surface through the abrasion technique, which forms a junction in the form of a cold weld in between them. Chromel and constantan wires of 0.25mm diameter are spot welded and taken out as lead wire for further instrumentation purposes. The schematic of the fabricated probe is mentioned in **Fig. 6. 1**.

6.3 Response of the thermal probe towards cyclic thermal load

The response of the thermal probe can be evaluated by exposing the sensor to an environment where the operating parameters can be controlled and measured. In this context, the IC engine helps in providing a real-time application. A standard four-stroke IC engine is commonly executed in one operational cycle time for complete four strokes (suction stroke, compression stroke, power stroke, and exhaust stroke), which involves two revolutions of the crankshaft. For a fixed RPM, the cycle time of the engine (for completion of one cycle) remains constant. Along with cycle time, a few other parameters, such as valve opening time injection time of the IC engine, can be fixed. The combustion process in SI engines takes place inside the engine cylinder after getting ignited by a spark plug. Here, the air fuel

mixture is sucked inside the engine through suction valve and compressed before the starting of ignition peocess. After completion of the combustion process the byproducts goesout through exhaust valve. The entire process takes place in four strokes; suction, compression, power and exhaust. It may be noted here that the exhaust valve opens once in a complete cycle to expel the byproducts. Therefore, the sensor can be exposed to the exhaust gases at a periodic interval by mounting it at any place along the exhaust pipe. Before conducting the actual experiment in the IC engine setup, a calibration test has been performed in the laboratory scale to check the response of the probe towards cyclic heat load. Therefore, a hot water plunging setup is designed to carry out the task. In this process, the sensor is put in the hot water bath and taken out to room temperature. The process is repeated for a certain interval of time, and the response is recorded.

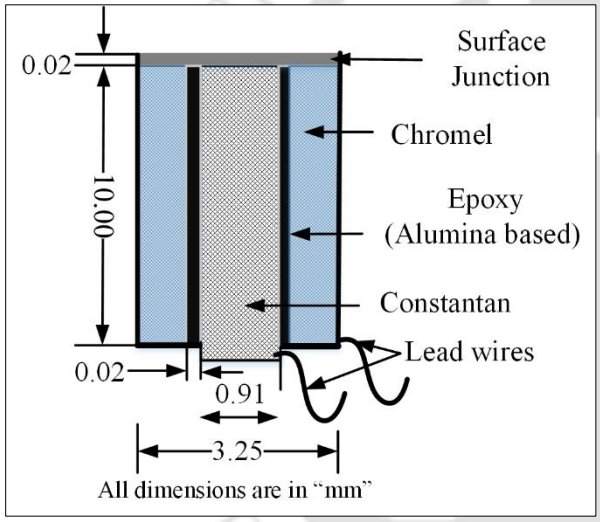

Fig. 6. 1: Schematic of the high temperature probe

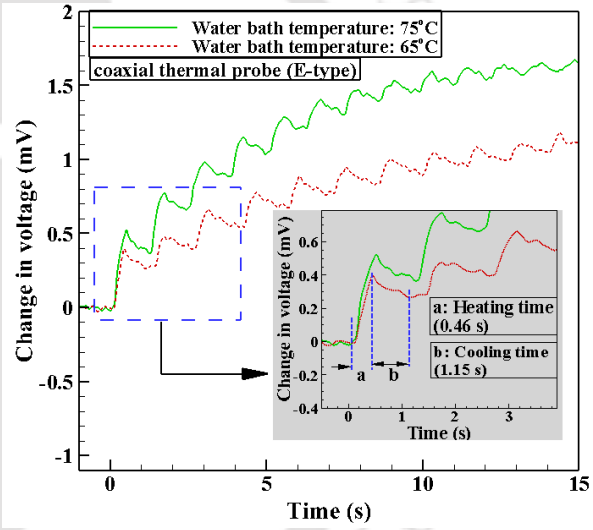

Fig. 6.2: Response from water plunging experiment

For the present case, a constant temperature bath maintained at two different temperatures (75ºC and 65ºC) is used for the plunging, and the results are plotted in **Fig. 6.2.** The results indicate a sharp rise of the signal while putting the probe in water but not a sharp cooling when taken out from the hot water. While repeating the process, there happens to be another sharp rise of the probe from its current position (position reached during the cooling process). The heating plots have a steeper slope than the cooling slopes, indicating that the sensor is taking a higher time to cool. Residual heat is always remaining in the probe, which is due to

the thermal mass of the probe. The cooling process slows down when the frequency of plunging increases. However, the heating response is very sharp, which is used in this case to find the time difference as a similar response pattern is expected in the IC engine exhaust. The detailed information about the internal combustion engine used and the experimental facility is explained in the subsequent sections.

6.4 Experimental engine set up

The setup consists of a single-cylinder, four-stroke, water-cooled, variable speed, VCR (Variable Compression Ratio) SI engine (*Make: Apex Innovation Pvt. Ltd., India, Model: 240 PE*). The rated power of the engine is 4.5kW at CR 10 and 1800 rpm in gasoline mode. The engine is coupled with a water-cooled eddy current dynamometer (*Make: SAJ International Pvt. Ltd, Model AG10*) for loading the engine crankshaft with the induced electromotive force (emf). The engine operates with a hemispherical combustion chamber, and the engine is cooled by circulating water through the jackets of the engine block and cylinder head. The detailed technical specifications of the engine, along with the mounted accessories and instrumentation, are listed in **Table 6.1**. The fuel induction mechanism of the engine consists of a fuel tank, fuel pump, fuel injector, optical crank angle encoder, and a programmable electronic control unit (ECU) of the gasoline injection timing and duration. The panel box attached to the engine consists of an airbox, fuel tank, manometer, fuel measuring burette, dynamometer loading unit. The electronic panel contains an ECU and NI USB-6210 data accusation system (DAS). A diaphragm type piezo pressure sensor (*Make: PCB Piezotronics, Model: M111A22*) is mounted on the engine head to measure the dynamic response of the cylinder pressure during combustion. The optical crank angle encoder (*Make: Kubler, Model: 8.3700.1321.0360*) is attached with the engine to deliver a signal for each degree rotation of the crankshaft. The amount of airflow consumed is measured by an airflow transmitter (*Make: Wika Instruments Ltd., Model: SL1*) attached to the airbox, while the rotameters monitor and measure the constant flow rate of cooling water to the engine jacket along with the exhaust gas calorimeter. The gasoline consumption is tracked by a differential pressure transmitter (*Make: Yokogawa Electrical Corporation, Model: EJA110-EMS-5A-92NN*) and a fuel burette attached with the fuel induction system. An ECU regulates the

triggering, measurements of air and coolant temperatures, throttle positioning, and fuel injection system. The engine is connected to the Labview-based software “Enginesoft” to record and analyze the data stored via a NI USB 6210 data logger. The ignition process is initiated by the ECU-controlled direct ignition system (DIS) attached to the engine through the ignition coil spark plug. The ignition process starts when the input signal is received from the optical crank angle encoder and is triggered by the hall effect sensor or trigger sensor. The schematic of the test facility is given in **Fig. 6.3.**

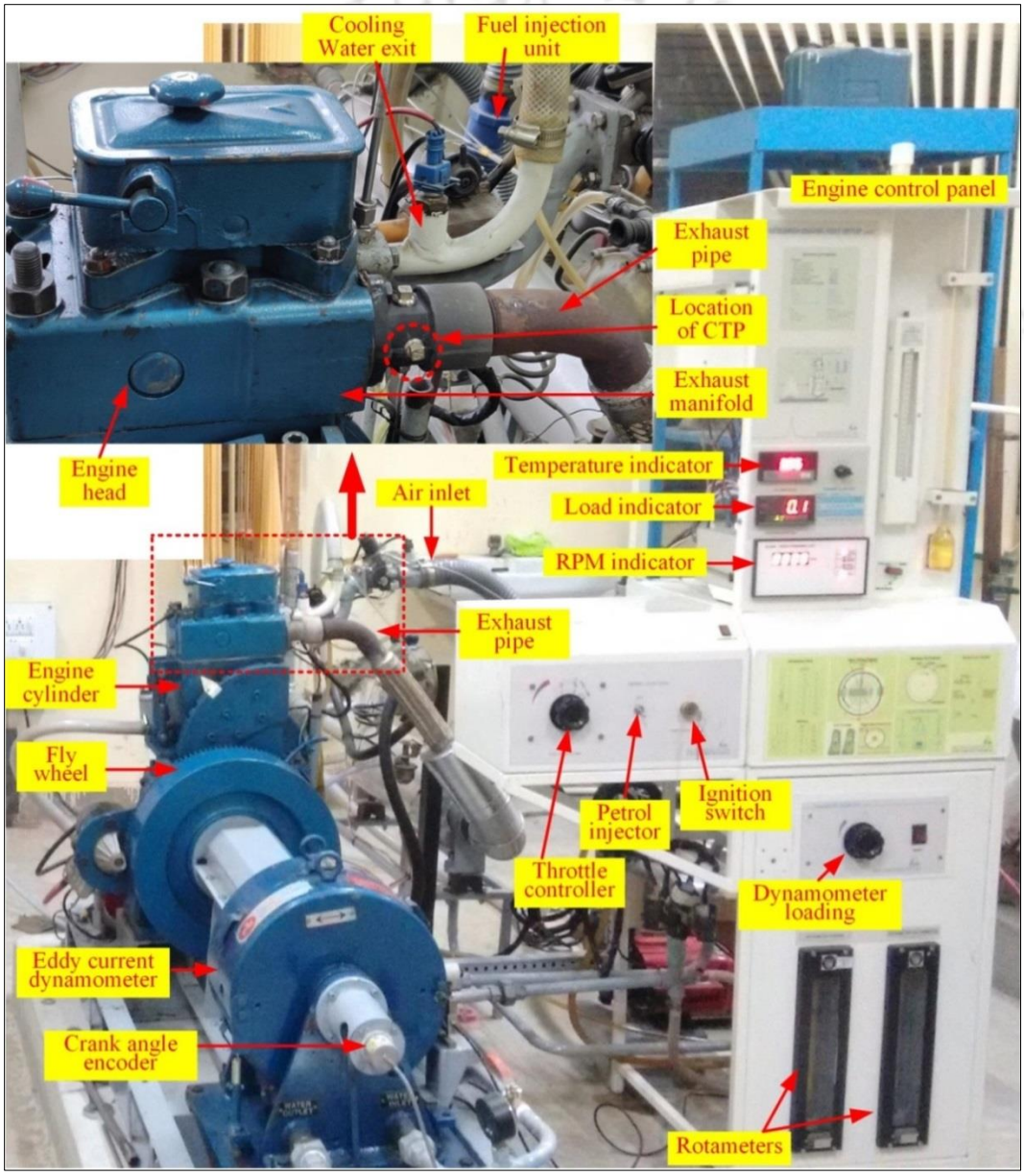

Fig. 6.3: Components of the engine set up.

Table 6.1: Engine specification

System specifications	
Parameter	*Specification*
Product	Research engine test setup, Code 240
Type	Research Engine test setup 1 cylinder, 4 stroke, Multi-fuel VCR
Power	4.5 KW @ 1800 rpm, Speed range 1200-1800 rpm.
Type of cooling	Water cooled
CR range	6:1-10:1
Combustion chamber	Hemispherical bowl in piston type
Dynamometer	Eddy current type, water cooled with loading unit
Air box	MS fabricated with orifice meter and manometer (100 - 0 - 100)
Fuel tank	Capacity 15 lit with measuring tube (0-450 ml)
Calorimeter	Pipe in pipe type
Rotameters	Engine cooling 40-400 lph, calorimeter 25-250 lph
Data acquisition	'Enginesoft' engine performance analysis software
Transmitters, sensors and indicators	
Fuel flow transmitter	DP transmitter, range 0-500 mm WC
Air flow transmitter	Pressure transmitter (-) 250 mm WC
Pressure sensors	Piezo type, range 5000 PSI, with low noise cable
Temperature sensors and	PT100 (RTD) type, range 0-100º C, output 4-20 mA (4 nos)
Load sensor and	Strain gauge type load cell with digital indicator, range 0-50 kg
Speed sensor and	Resolution 1º, range (5500 rpm) with TDC pulse
Data acquisition device	NI USB-6210, 16-bit, 250 kS/s
Setup constants	
Pulse per revolution	360º
No. of cycles	10
Fuel measuring interval	60 s
Speed scanning intervals	2000 ms
Bore × Stroke	87.5 mm × 110 mm
Capacity	661 cc
Orifice diameter	20 mm
Dynamometer arm length	185 mm
Connecting rod length	234 mm
Theoretical constants	
Orifice coefficient	0.6
Specific heat of exhaust	1.00 – 1.25 kJ/kg-K
Specific heat of water	4.186 kJ/kg-K
Density of Air	1.174 kg/m^3
EGR Specification	
EGR flow rate	orifice (ø16 mm)with manometer(100-0-100)mm
Treated EGR	Three way catalytic converter
Calorimeter	Pipe in pipe type

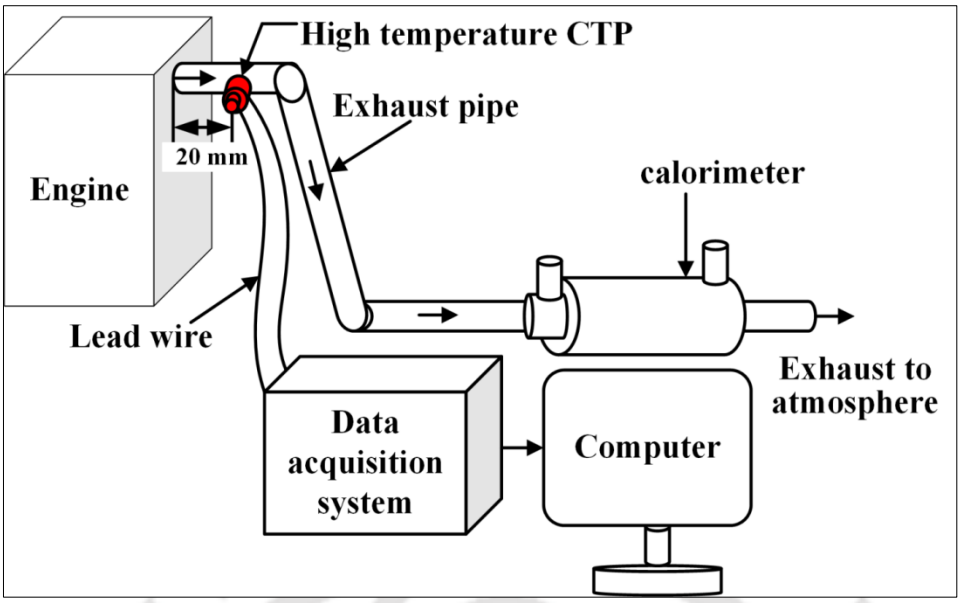

Fig. 6.4: Schematic representation of the experimental set up

6.5 Experimental procedure

The in-house fabricated CTP is exposed to the hot engine by-product (hot air) at the exhaust of the engine. The CTP is mounted at a 20 mm distance from the exhaust manifold (**Fig. 6.4**). The sensor is flush mounted so that the flow is not disturbed by the presence of the sensor, and the sensing surface is nicely exposed to the heat load. The sensor is connected to a NI-data acquisition system for capturing high-frequency voltage signals at a rate of 100000 samples per second. The compression ratio is set to 10, which is almost one end for a petrol engine. The engine is run for two different RPMs (1500 & 1700), and responses are captured through data acquisition system (**Fig. 6.5**).

6.6 Results and discussion

The voltage signals are recorded using a NI-based data acquisition system (Make: National Instruments, Model: NI-9223/ cDAQ-9178) for capturing data with the help of lab view programming. The signal is filtered with a low pass filter to omit noises, and the results are plotted. As the intention of the work is to get engine information from the external signal, the experiment is done by putting the sensor at a close location of the exhaust manifold to capture the maximum heat content of the exhaust gas. The results for 1500 and 1700 RPM are plotted in **Fig. 6.5 (a)**. As expected, the sensor indicates a sharp rise at the arrival of the hot gases and then the subsequent cooling phase. This cycle repeats itself as the exhaust valve of the engine opens after a certain interval of time

corresponding to the RPM of the engine. Depending on the speed i.e. revolution per minute (RPM) of the crank shaft, the time taken for a complete cycle can be calculated analytically from equation 6.1. The experimental cycle time is calculated using the time span between two sharp rises in signal and is compared with the theoretical cycle time (**Fig. 6.5 (b)**). The experimental and theoretical cycle time is tabulated in **Table 6.2**. A deviation of 0.12% and 0.25% is observed for 1500 RPM and 1700 RPM, respectively.

$$Cycletime, t(ms) = \frac{2 \times 60}{RPM} \times 1000 \quad \ldots\ldots\ldots\ldots\ldots\ldots\ldots\ldots\ldots\ldots\ldots\ldots\ldots\ldots \text{(6.1)}$$

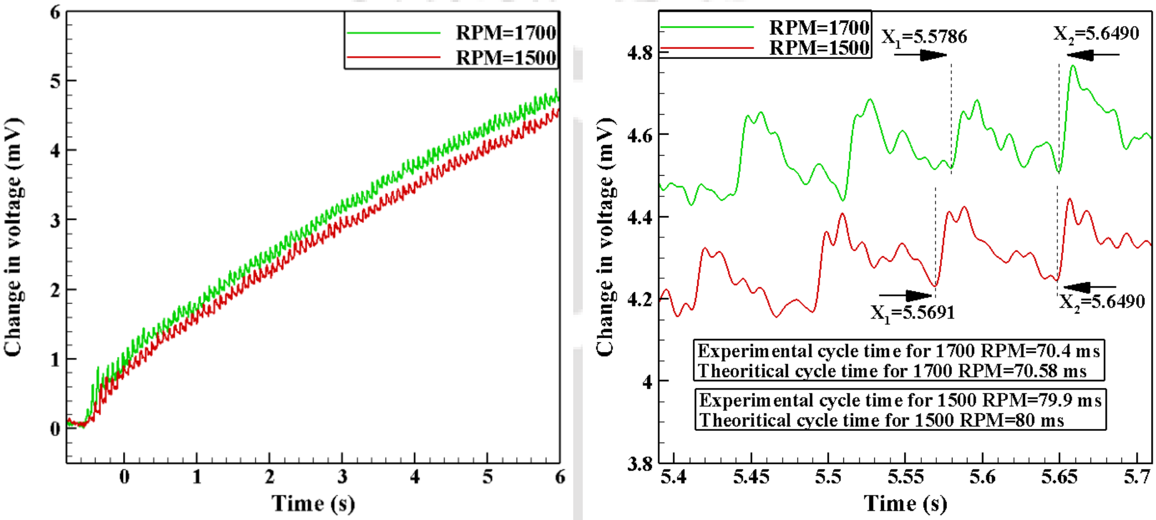

(a) (b)

Fig. 6.5: Temperature response from the probe; (a) Voltage signal; (b) Cycle time calculation

Table 6.2: Comparison of experimental and theoretical cycle time.

RPM	Experimental cycle time (ms)	Theoretical cycle time (ms)	Deviation (%)
1500	79.9	80	0.12
1700	70.4	70.58	0.25

The temperature response from the sensor is used for the estimation of transient heat flux. Considering the restrictions in the validity of one dimensional heat conduction and semi-infinite substrate assumption, the signal is considered for 0.5s from the initial rise of the temperature for the heat flux estimation. As inferred from the **Fig. 6.6**, the peak magnitude of heat flux is in the range of 500 ± 50 kW/m^2 for 1500 RPM and 550 ± 50 kW/m^2 for 1700 RPM. The exhaust valve opens once in a cycle (4 strokes), and the sensor receives an instantaneous heat load. Therefore, the peak heat flux of nearly similar magnitude indicates the nearly equivalent combustion process.

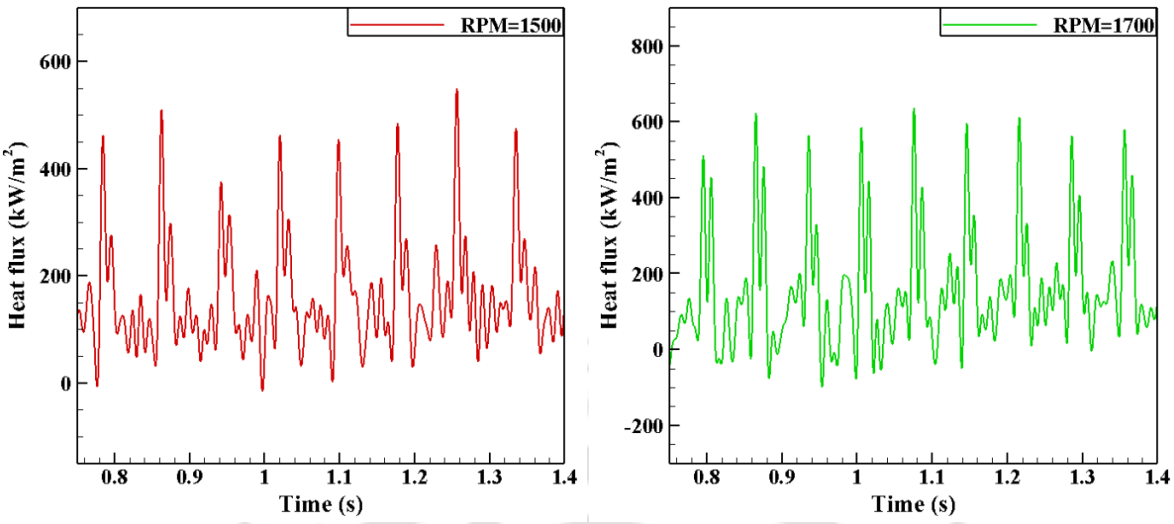

(a) **(b)**

Fig. 6.6: Heat flux estimation for 0.5s after the initial rise; (a) RPM=1500; (b) RPM=1700

6.7 Summary

The coaxial probe is exposed to the hot gas coming out from the engine exhaust manifold. The cyclic nature of heat load is well captured by the probe. From the experiment, it is clear that the sensor is able to capture cycle time correctly. The transient temperature data estimate the heat content getting lost as a by-product in terms of heat flux. This analysis can further be extended in different parametric studies such as detecting knocking, incomplete combustion, etc. The aim of the study can be extended to engines in moving vehicles where a sensor can be mounted at any location in the line of exhaust, and some amount of exhaust air may be blown over it. From the response, the driver can get on-time engine health monitoring.

CHAPTER 7

Implementation of soft computing technique for recovery of impulsive heat loads

Overview

Most research articles about short-duration heat transfer recovery focus on conventional methods through appropriate modeling of the sensor configurations. This modeling task involves a lot of assumptions and simplifications, putting a question mark on the accuracy of the result; however, the results obtained through this modeling are well within an acceptable range. With the advancement of the soft computing technique in this modern era, an alternate and less cumbersome approach can be exercised to recover the heat load for short-duration flows. Moreover, the usage of soft computing techniques for short-duration heat flux recovery is not available in the open literature. Therefore, the objective of the present work is to implement and assess the usability of soft computing ANFIS based technique to create an efficient system that can predict heat flux from temperature history. Hence, it is highly desirable to investigate the feasibility of the usage of soft computing techniques for the recovery of heat flux from the temperature data of an impulse facility. Further, it is essential to establish a methodology for recovering such heat flux signals in the backdrop of such development. This complimentary procedure needs to be validated with experimental, computational, and analytical results. Thus, a validated soft computing technique would remain a simplified and user-friendly option for recovering time variation of applied heat flux from short duration temperature measurement. Here, two exercises are planned to execute the task; one for the convective load (using shock tube) and another for radiative heat load (using laser heating). For the convection heat load, a known data set of "time-temperature-heat flux" is generated for training purposes through numerical simulations, and after training, the shock tube temperature signals is used for the heat flux recovery. Similarly, for radiation heat load, the training data set is generated through numerical simulation and laser heating. The intermediate laser heat loads are recovered from the temperature signal. Different exercises are carried out using these temperature signals to recover the heat flux while establishing the novel soft computing-based procedure.

7.1 Introduction

The analytical and numerical method for heat flux recovery has been elaborated in Chapter 2. The analytical approach by assuming the sensor as a semi-infinite body has been well accepted by the researchers for a long time, well within certain limitations. In both the methods (analytical and numerical), a certain number of equations are solved with approximations to reach the desired solutions. However, when the time scale of application is very small, and the heat flux also has a smaller magnitude, these errors are quite prominent. The conventional technique of heat flux recovery is suitable and routinely used by the researchers for thermal sensors like thin film Gauges (TFGs), thermocouples and for the commonly used sensing and backing materials as in the case of TFGs. But this technique demands the knowledge of sensor parameters like temperature coefficient of resistance (TCR) and thermal product (β). However, with the development of new materials and also gauge preparation techniques with the nano-materials, it becomes essential to calibrate the sensors for arriving at the necessary sensor parameters for heat flux recovery using exclusive and costly experimental set-ups. Further, it must be noted that the parameter "β" is treated as a constant while working with TFGs, but it changes its value for the coaxial probe during the experiment (Schultz and Jones, 1973). Further, the limitation of the conventional technique is simplified due to the assumptions involved, like one-dimensional heat transfer and semi-infinite objects. Therefore, in view of the requirement of costly calibration set-ups and assumptions involved, the application envelops of this technique get shortened for one dimensional and steady heat transfer recovery. Hence, with the advancement of the soft computing technique, it has been planned to develop an alternative technique that would have the potential for its applicability in a larger envelope and any thermal sensor. Therefore, the recovery of heat flux has been performed taking the temperature signals obtained from the previously carried out experiments at two different experimental approaches; one in convection mode and another in radiation mode. The actual heat load on the sensors in the shock tube flow (convective mode) lasts for 1-2 ms (Chapter 5). Therefore, the training and recovery process for heat flux prediction has been carried out for a 2ms duration for step and ramp heat loads (as these are most common in high-speed flows). At the same time, the radiation mode of heat transfer has been accomplished with the help of laser heating, where the sensor is heated for a time duration of 0.4s (Chapter 4). A combination of

experimental and numerical temperature signals is used to train the system, and the recovered heat flux values are compared with the known signals. The detailed working procedure for this novel approach has been elaborated in the subsequent sections.

7.2 Soft computing approach – ANFIS

Soft computing techniques have gained popularity in recent times due to their simplicity and in-dependency on an intense mathematical model. These techniques are data-driven and mostly depend on the mapping of input and output data set. Therefore, its usage is explored for the prediction of unknown data in different domains like control theory, image identification, power sectors, weather prediction (Buragohain, 2009). Soft computing is available in various forms such as neural network, fuzzy logic, machine learning, genetic algorithm, (Pratihar, 2013). However, hybrid methods (combination of two or more techniques) have evolved as potential tools in present times due to their capability towards efficient and accurate prediction of unknown data. One such hybrid technique is the Adaptive Neuro-Fuzzy Inference System (ANFIS), which is a combined approach of neural network and fuzzy logic; proposed in reference (Jang, 1993). Here, the "Takagi-Sugeno type fuzzy inference model" is embedded in the artificial neural network path. The fuzzy logic part in the ANFIS deals with the uncertainty of the system, and the neural network provides a sense of adaptability to it. Owing to the advantages, ANFIS is used widely in different engineering applications such as; prediction of heat transfer coefficient in case of heat exchanger (Elaziz et al., 2019), free convection heat transfer in case of the partitioned cavity, and also in vertical arrays of isothermal cylinders (Karami et al., 2013; Rezaei et al., 2012), heat exchangers (Hayati et al., 2009), prediction of thermophysical properties of carbon dioxide (Yılmaz et al., 2014), calibration of air-data sensors (Lando et al., 2007), machine fault diagnosis (Lei et al., 2007; Saeed et al., 2013), flow stress during deformation process (Han et al., 2011), aerodynamic estimation from flight data (Ghosh Roy and Peyada, 2017; Kumar and Ghosh, 2018), aerodynamic coefficient determination in impulsive shock tunnel testing (Nanda et al., 2016; Nanda et al., 2019). The concept is also used in the analysis of the usage of nano fluids in different applications (Li et al., 2019). Thus it is evident that soft computing techniques are quite reliable and can be applied for data prediction for a variety of applications. The step by step working procedure of ANFIS has been explained in the subsequent subsections.

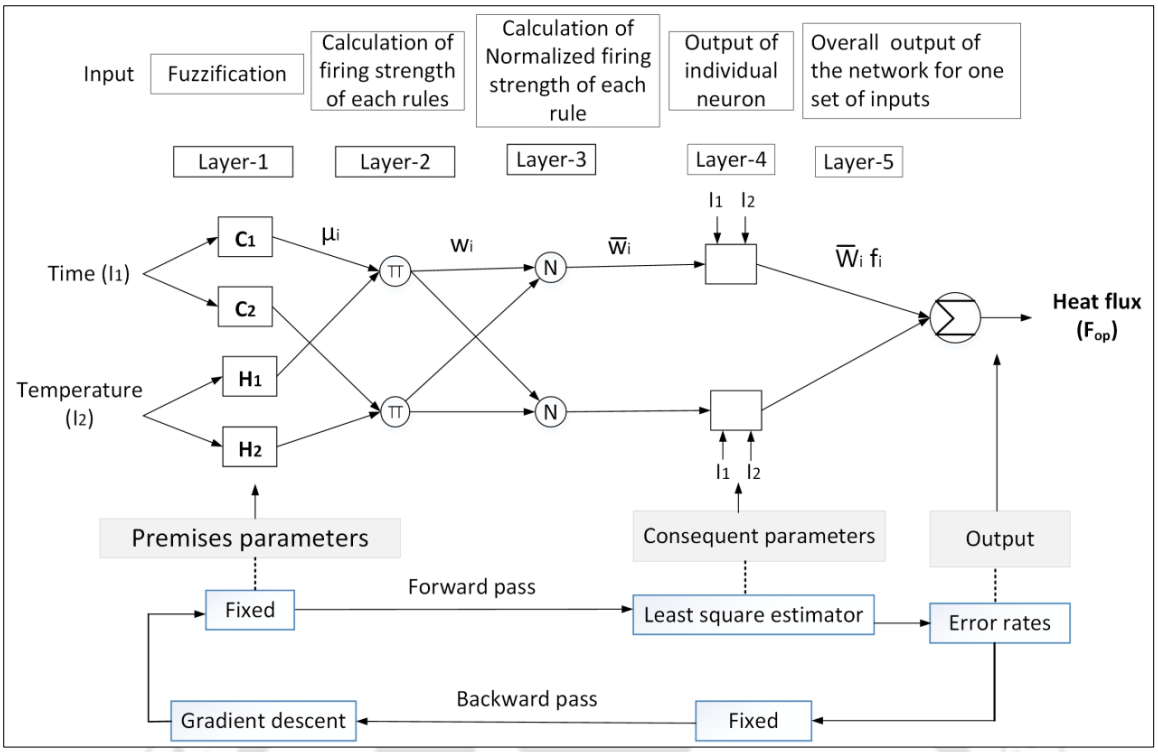

Fig. 7. 1: ANFIS architecture for short duration "time-temperature-heat flux" data set

7.2.1 ANFIS architecture

The architecture of ANFIS modeling for the "temperature-time-heat flux" data set of the short duration experiment is shown in **Fig. 7. 1**. It consists of 5 layers, and each layer contains several nodes designated with node functions (Ramesh et al., 2019). The nodes are of fixed type (denoted by circles) and adaptive type (denoted by squares). In the fixed type nodes, the parametric changes are not allowed, whereas there is a scope for improvement for the operating parameters through optimization method or using feedback loop in adaptive type nodes (Buragohain, 2009). For simplicity, the ANFIS system here is explained with two inputs and one output. The rule base of the model consists of "Takagi and Sugeno type fuzzy if-then rules" where the output is a function of input variables like

$"If\ I_1\ is\ C\ and\ I_2\ is\ H\ then\ O\ is\ f(I_1, I_2)"$

Here, $"C \& H"$ are the fuzzy sets corresponding to antecedents, and "O" is a crisp function in the consequent.

Generally, it is in the form of polynomial taking the input variables I_1 *and* I_2 of the form

$$f_n = x_n I_1^n + y_n I_2^n + z_n \tag{7.1}$$

but possibly, it can be any function that can suitably describe the system output as specified by the antecedents. Here, x_n, y_n and z_n are coefficients of the polynomial and n corresponds to the degree of the polynomial. If $n=0$, the then $f(I_1, I_2)$ is a constant, which indicates a "zero-order Sugeno fuzzy model"(El-Hasnony et al., 2020). The activities of different layer of ANFIS architecture considering a "first-order Sugeno fuzzy model" is explained below.

Layer-1: The first layer performs the fuzzification of the set of inputs where it converts a crisp set into a fuzzy set with the help of membership functions (μ). Individual nodes belonging to this layer are adaptive in nature with a node function as given in Eq. 7.2.

$$O_{1,i} = \mu_{C_i}(I_1) \quad for\ i = 1,2 \text{ and } O_{1,i} = \mu_{H_{i-2}}(I_2) \quad for\ i = 3,4 \tag{7.2}$$

Where, I_1 *and* I_2 are the inputs to nodes i , C_i, H_i are linguistic variables (large, small..etc.) associated with the node function and μ_{C_i} *and* μ_{H_i} are the membership functions of C_i *and* H_i, respectively. Different types of MFs are used for fuzzification depending on the type of data set and user experience. The parameters belonging to this layer are influencing the conclusion and hence are called "premise parameters."

Layer-2: All the nodes in this layer are fixed nodes, marked by an encircled π symbol. The activity of this layer is to calculate the firing strength (w_i) of a rule. The output corresponding to each node in this layer is the product of incoming signals to it. The firing strength, i.e., the output of the ith node, $(O_{2,i})$ can be expressed as

$$O_{2,i} = w_i = \mu_{C_i}(I_1).\mu_{H_{i-2}}(I_2) \quad for\ i = 1,2 \tag{7.3}$$

Layer-3: Nodes belonging to this layer are fixed, labeled by encircled N. The normalized firing strength $(\overline{w}_i)$ is the output from this layer. The output for the ith node $(O_{3,i})$ is the

ratio of firing strength of the i[th] node (w_i) to the sum of all the firing strengths corresponding to all the rules.

$$O_{3,i} = \bar{w}_i = \frac{w_i}{w_1 + w_2} \quad for\ i = 1,2 \tag{7.4}$$

Layer-4: All the nodes in this layer are adaptive or adjustable in nature, marked by square. The node function is described as

$$O_{4,i} = \bar{w}_i . f_i \quad for\ i = 1,2 \tag{7.5}$$

Where, $f_i = x_i I_1 + y_i I_2 + z_i$ is a first-order polynomial, $\bar{w}_i$ is the output of layer-3 and $\{x_i, y_i, z_i\}$ are consequence parameter set. The polynomial is the output corresponding to a particular rule i.e.

- Rule-1: *IF* Q_1 *is* C_1 *and* Q_2 *is* H_1, *then* $f_1 = x_1 I_1 + y_1 I_2 + z_1$
- Rule-2: *IF* Q_1 *is* C_2 *and* Q_2 *is* H_2, *then* $f_2 = x_2 I_1 + y_2 I_2 + z_2$

Layer-5: This layer contains a fixed node labeled by an encircled summation symbol which indicates the activity of the layer is to sum all the incoming signals to produce an overall output i.e.

$$O_{5,i}(overall\ output) = F_{op} = \sum_i \bar{w}_i . f_i = \frac{\sum_i w_i . f_i}{w_i} \tag{7.6}$$

7.2.2 Learning algorithm

It is observed from the final output of the ANFIS structure (Eq. 7.6) that if the premise parameters are given, the final output can be stated in the form of linear combined consequent parameters $(x_1, y_1, z_1, x_2, y_2, z_2)$. The output (F_{op}) can be expressed by Eq. 7.7.

$$F = \bar{w}_1 f_1 + \bar{w}_2 f_2 = (\bar{w}_1 I_1)x_1 + (\bar{w}_1 I_2)y_1 + (\bar{w}_1)z_1 + (\bar{w}_2 I_1)x_2 + (\bar{w}_2 I_2)y_2 + (\bar{w}_2)z_2 \tag{7.7}$$

The learning process in ANFIS deals with updating its parameters with the help of an algorithm. It consists of two passes; one is in the forward direction and the other in the reverse direction called “forward pass” and “backward pass,” respectively.

In the learning process, the parameters in the "layer-1" and "layer-4" are updated to minimize the error between desired and actual output. This training task is accomplished by ANFIS with the help of a hybrid gradient descent algorithm and least square estimator to minimize the error.

Table 7.1: Learning process in ANFIS using the hybrid technique.

Entities	Forward pass method	Backward pass method
Premises parameter	Unchanged	Gradient descent
Consequent parameters	Least square estimator	Unchanged
Signals	Output of each node	Error calculation

The "forward pass" of the algorithm deals with transporting the node outputs from the "layer-1 till layer-4" and calculation of consequent parameters using the least square estimate (**Table 7.1**). The "backward pass" deals with transporting the error information from the output layer to the input layer, where the error signals are the derivatives of the squared error with respect to individual node output. Based on the error information, the premise parameters are updated with the help of the gradient descent algorithm. Through this process, the neural network learns and trains to regulate the magnitudes of the different parameters that can sufficiently fit the training data. These basic learning approaches have been implemented for the recovery of the convective and radiative heat loads. The working procedure of ANFIS can be schematically represented in a flow chart as in **Fig. 7.2**.

7.3 Heat flux prediction in convection based experiment

Possibility of the use of the soft-computing technique for the recovery of surface heat flux, especially for short duration studies, is the main aim of the present investigation. Therefore, the heat flux prediction in the convective mode of heat transfer experimentation is planned by taking real-time experimentation in a shock tube. Here, the sensor receives a step/ramp heat load for a few milliseconds (~ 1-2 ms) induced due to the fast-moving fluid inside the shock tube. The working detail about the shock tube has been explained in chapter 5. The working parameters for the present study are 'time,' 'temperature,' and 'surface heat flux.' Time and temperature are the training input parameters, and the surface heat flux is the output parameter (**Fig. 7.3**).

Fig. 7.2: Schematic representation of ANFIS approach

The system is trained with known time-temperature-surface heat flux, and the trained model is used for the prediction of unknown surface heat flux. In this backdrop, a known data set of "time-temperature-heat flux" is generated for training purposes with the help of numerical simulations. Computations are performed for the coaxial thermal probe to arrive at temperature-time history for a known heat flux input. Here, computations are performed with input heat flux (as ramp and step signals) in the range of 1W-5W (**Fig. 7.4**). The detailed mathematical modeling for the numerical computation is elaborated in Chapter 2. This process is repeated for step and ramp, which are often encountered in short-duration testing. Different exercises are carried out by using these temperature signals to recover the heat flux. The detailed working procedure is elaborated in **Fig. 7.3**.

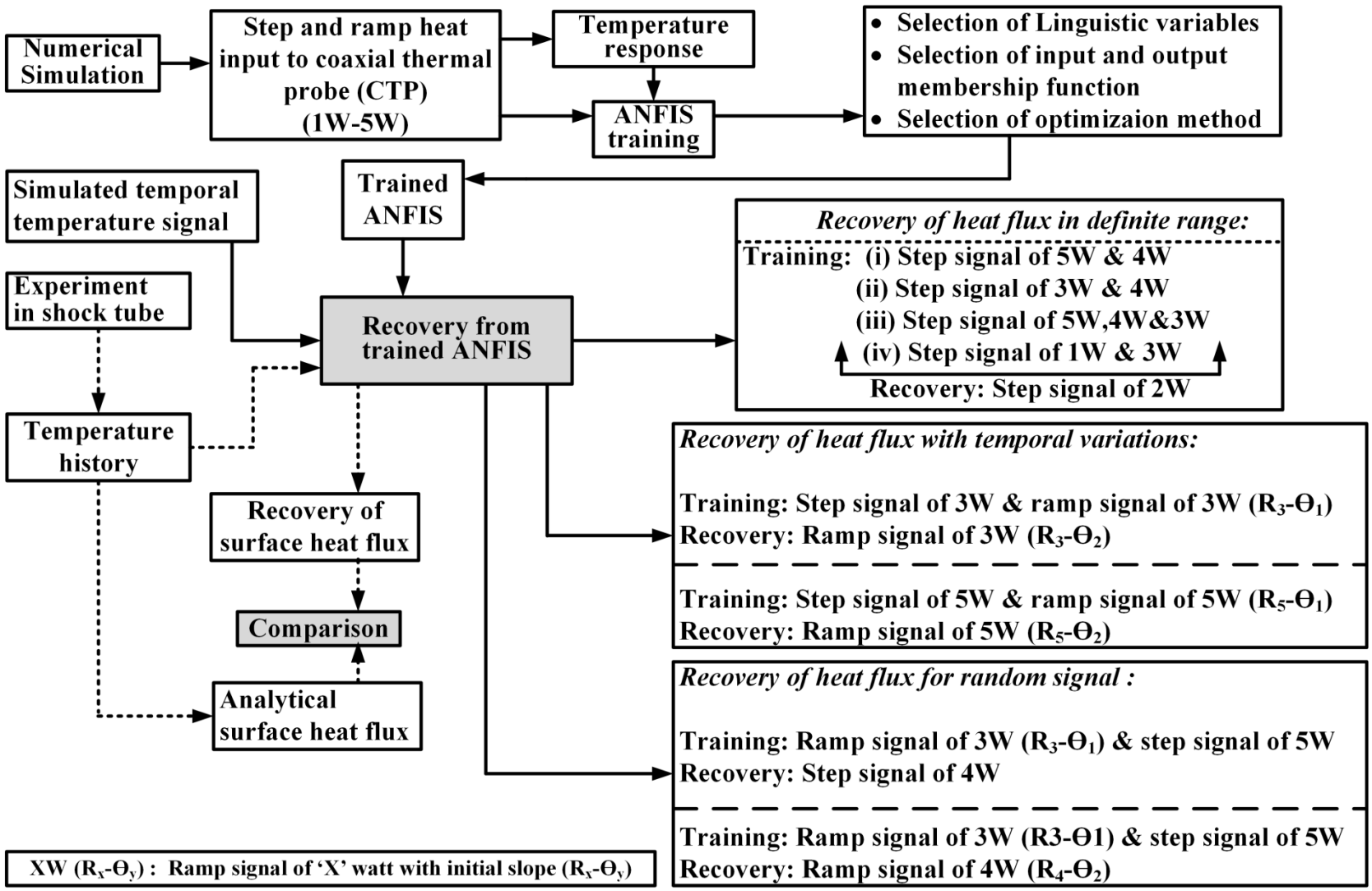

Fig. 7.3: Working methodology of heat flux recovery in case of convective heat load

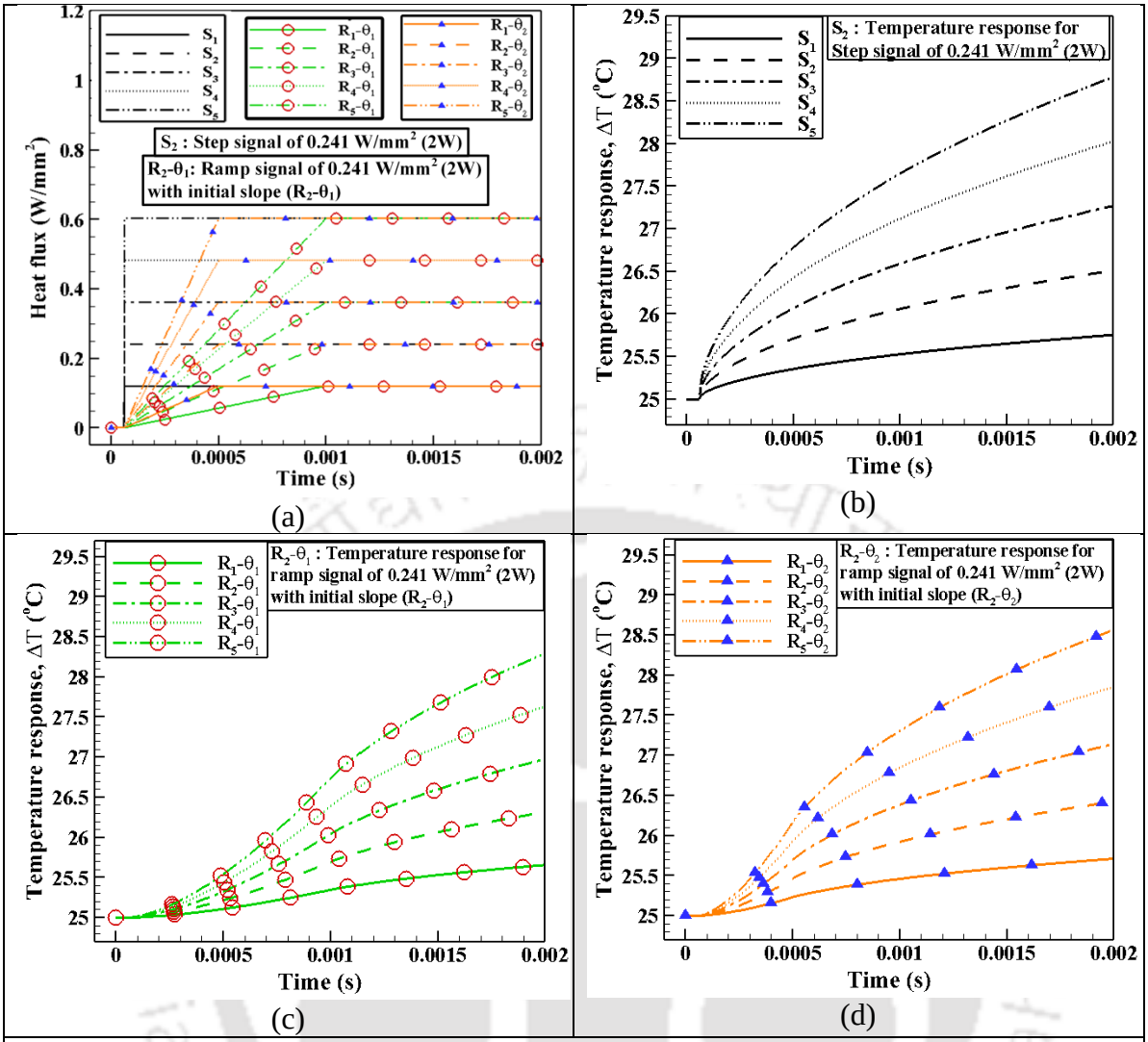

Fig. 7.4: Numerical simulation results; (a) Step and ramp heat loads (b) Temperature profiles for step heat load (c) Temperature profiles for ramp heat load with initial slope (R_x-θ_1) (d) Temperature profiles for ramp heat load with initial slope (R_x-θ_2).

7.3.1 Extraction of initial fuzzy model

Derivation of an initial fuzzy model is the initiation of the ANFIS modeling process. This requires the selection of different parameters (like number of input variables, type of membership function, number of linguistic variables), which is directly related to the number of rules in the final fuzzy model. Different ANFIS models can be constructed for a given data set using separate identification methods, e.g., different clustering techniques (Fuzzy c-means clustering) grid partitioning method (Abdulshahed et al., 2015). During the grid partition process, the data space undergoes axis paralleled partitions to create a fixed number of rectangular subdivisions (subspaces) based on predefined MFs (both type and number) in each dimension. The grid partition is only suitable for problems with a

smaller (less than 6) number of input variables (Jang, 1993). Here, the proposed model has two inputs (time, temperature) & one output (heat flux). Therefore, it is sensible to apply the grid partition method. A Matlab (version-2019a) based platform is used to exercise for the ANFIS since it can provide the requirements for its training and recovery (MathWorks, 2000). The process of training requires the selection of "number of linguistic variables," "type of input membership function (IMF)," "optimization method," and "output membership function (OMF)"(**Fig. 7.5)**. Successful implementation of ANFIS for current objectives needs a thorough understanding of the process followed or various steps of this algorithm. All such steps demand different user inputs, and the current discussion is on the selection of these inputs for the specific application.

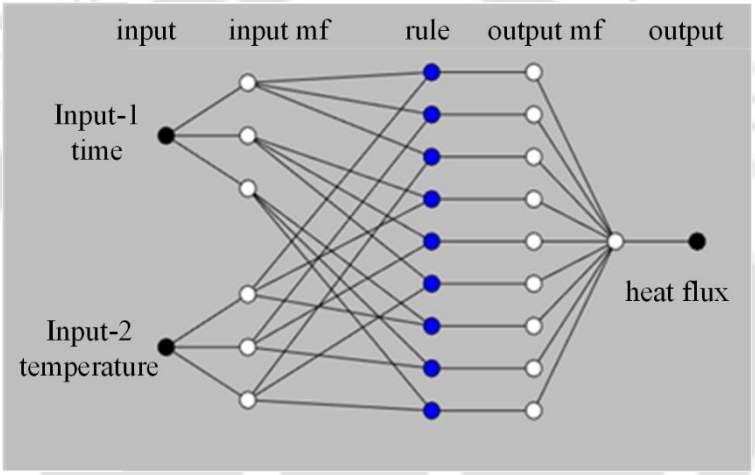

Fig. 7.5: ANFIS architecture for optimized combinations

The parametric variations for fuzzification mainly deal with the type of membership function (MF) to normalize the input training data set. Available options for these functions are from the broad categories as piecewise linear functions, Gaussian functions, bell-shaped functions, and sigmoid functions. Therefore, the standard input MFs used are triangular MFs, trapezoidal MFs, bell-shaped MFs, sigmoid MFs, Gauss MFs, singleton MF, pi MF, etc. Similarly, there are two types of output MFs viz. "linear" and "constant." Out of the different MFs, the selection of a suitable one depends on the type of data and the user experience. With the help of membership functions, the fuzzy system can be tuned by adopting an optimization technique out of the available ones as "back propagation method" and "hybrid method" such that the input-output modeling can be carried out. The backpropagation method adopts the steepest descent algorithm for modifying all parameters during training, whereas the hybrid model uses the least square

method for parameters linked to the output MFs and back propagation for the parameters linked to the input MFs. Since various options are available and the best one needs to be selected, parametric studies are performed to find out the input requirements of ANFIS, and its capability is judged for the heat flux recovery. The detailed study for the selection of input entities for the generation of fuzzy interference systems considering "grid partition" type ANFIS architecture is elaborated in the following subsections.

Selection of membership functions

The selection of input membership functions (IMF) and output membership functions (OMF) is directly related to the available data type and user's experience. As the findings in the literature related to it are very limited, it is planned to work out with all available membership functions to identify the suitable combinations for this type of data set. Before selecting the type of MF, it is required to select the appropriate number of linguistic variables for the input training data sets as required for the fuzzification of the data set. After exploring different combinations for two input parameters (i.e., time and temperature), it is observed that three linguistic variables for each input are resulting in less error. Therefore, three linguistic variables are selected both for time and temperature for the subsequent exercise. The Matlab (2019-a) based ANFIS module is well equipped with different input membership functions, viz. tri MF, trap MF, gbell MF, gauss MF, gauss2 MF, pi MF, dsig MF and psig MF. The possible combinations out of these eight membership functions are sixty-four for two different inputs (time and temperature). Therefore, the data set is exercised for all the possible combinations of input MFs, and out of them, the predicted results with a maximum root mean square error (RMSE) of 0.025 are presented here. For the initial testing, the heat flux values of 0.120 W/mm^2, 0.241 W/mm^{2,} and 0.361 W/mm^2 corresponding to three wattages as 1W, 2W, and 3W, respectively, are used for the simulation. These heat flux values are applied as a step load to the sensing surface (as a boundary condition) for 2ms duration, and the corresponding temperature values are computed. The "time-temperature-heat flux" values for 1W and 3W are then used to train the system, and the heat flux signal for 2W is recovered from this training. Before proceeding for signal recovery, the trained system is checked for training accuracy with a set of data corresponding to 2W. The accuracy is found to be 97% for the "gauss-tri" membership function combination. The recovered signal is compared with the reference value, and the RMSE is calculated. It may be highlighted

here that, for the present data set, dissimilar types of membership functions have better accuracy. The results are tested for all possible combinations, and it is observed that in eight cases, encouraging agreement in terms of both magnitude as well as a trend is seen (**Table 7.2**). Out of these combinations "gauss2-tri" and "gauss-tri" combination infers the least error **(Fig. 7.6(a))**. It is further observed that the combination of "dsig MF" and "psig MF" is not able to predict the magnitude and trend for the step response. Therefore, these functions are not considered for such recovery.

Table 7.2: Prediction error for different input membership function combinations

Membership function		Root Mean Square Error (RMSE)
Input1	Input 2	
gauss2	gauss2	0.02469
gbell	tri	0.01273
gbell	gauss2	0.02266
gauss	tri	0.00926
gauss	gauss2	0.02443
gauss2	tri	0.00934
gauss2	gbell	0.01682
pi	tri	0.01284

Similarly, the inbuilt system of the Matlab platform offers only two types of output membership functions viz. "linear MF" and "constant MF." Therefore, the best membership function combination, as mentioned previously ("gauss2-tri" and "gauss-tri"), are tested for different output membership functions with the same training and recovery data set. It is observed that the "constant MF" results in the least error (**Table 7.3**) and delivers a better trend as compared to "linear MF" (**Fig. 7.6(b)**). Therefore, for subsequent analysis, "constant MF" is considered as output membership function.

Table 7.3: Prediction error for different output membership function combinations.

Input MF Combination	Output MF	Error (RMSE)
gauss2-tri	constant	0.00934
gauss2-tri	linear	0.01821
gauss-tri	constant	0.00926

gauss-tri	linear	0.01607

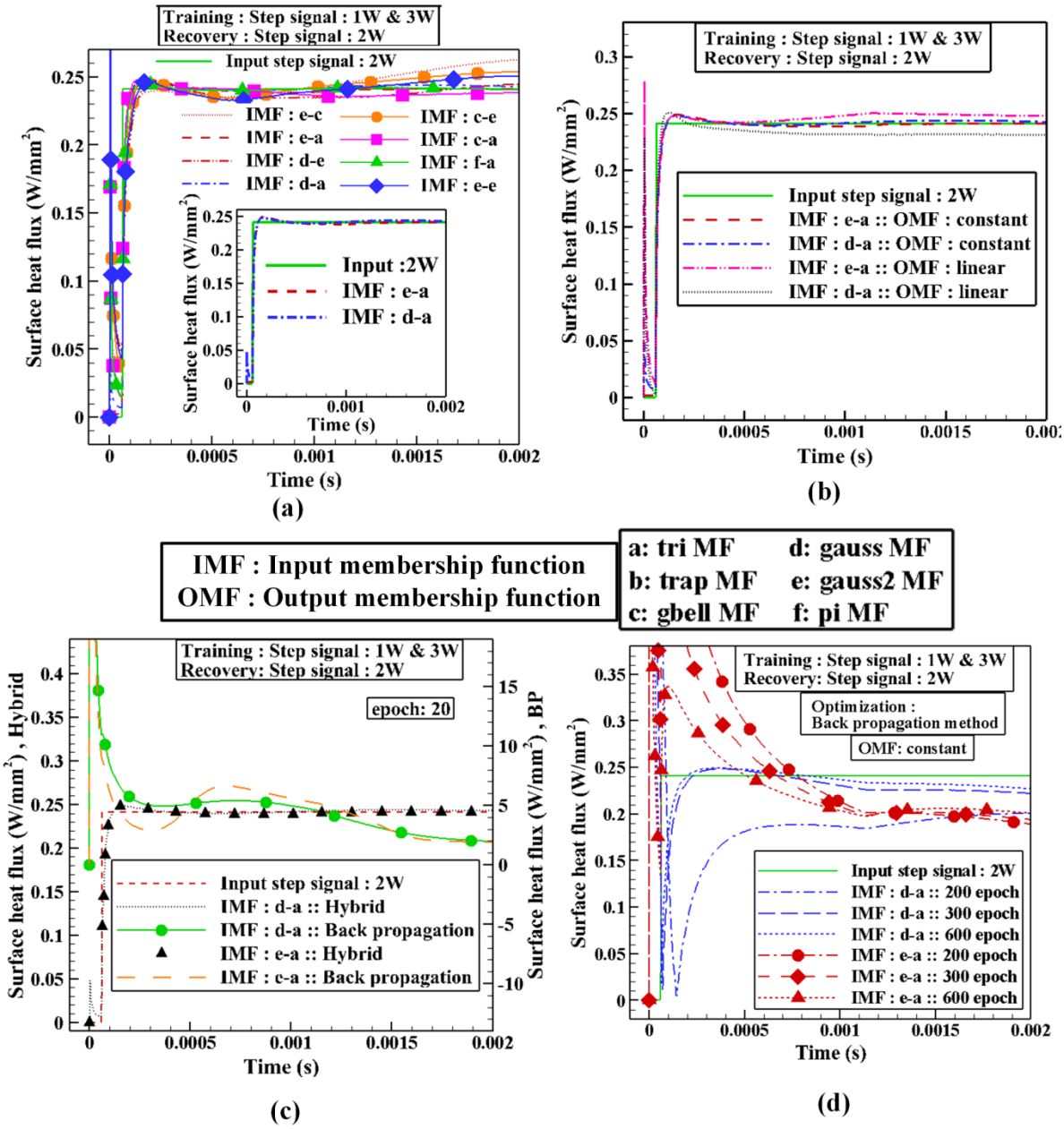

Fig. 7.6: Exercise to find out optimum parameters. (a) Effect of input membership function variations, (b) Effect of output membership function, (c) Effect of optimization technique and epoch, (d) Dependence of epoch on the back propagation technique.

Selection of optimization method

The optimization in the training process using the ANFIS model helps in the proper learning of the system. As available in the Matlab platform, the process of optimization can be accomplished by two methods viz. “back propagation” or “hybrid.” Along with

these methods, the selection of epochs is also an important factor for training. Therefore, a similar training and testing setup, as explained previously, is exercised here for "back propagation" and "hybrid" methods with different epochs. Here, the training is performed with 20 epochs with both the methods for the prediction of 2W heat load with the training of 1W and 3W (**Fig. 7.6 (c)**). The step response in the case of the hybrid method is predicted with an accuracy of 97%, whereas; the same is predicted without any matching trend and magnitude by the back propagation method. Along with this, it is also noticed that the hybrid method of optimization training could recover the step heat flux within a minimal error range irrespective of the no of epochs. The influence of initial condition and local minima might be the cause for the non-recovery of proper trend and magnitude by the back propagation method. The dependency of the back propagation method on the number of epochs is tested by increasing the no of epochs for the same training and recovery data set. **Fig. 7.6 (d)** represents the recovered results with different epochs for "gauss-tri" and "gauss2-tri" membership function combinations. The RMSE for different combinations is presented in **Table 7.4.**

It is clear from the exercise that the accuracy of the predicted results increases with an increase in the number of epochs in the case of the back propagation method. This observation can be justified since the learning rate increases with the number of epochs which in turn reduces the error in prediction.

Table 7.4: Prediction error for back propagation method with different epochs.

No. of epochs	RMSE (Gauss-tri)	RMSE (Gauss2-tri)
20	8.7573	9.90
200	0.642018	0.67692
300	0.23607	0.25755
600	0.103965	0.15046

From this analysis, it is observed that the "hybrid" type of optimization can be adopted for the prediction of heat transfer rate with minimum error at the expense of a lesser number of epochs and, in turn, the requirement of lower computational time. On the other hand, the "back propagation" optimization method requires a sufficiently higher number of epochs for the prediction of results in required accuracy, which ultimately leads to the requirement of more computational time. As an outcome of the current parametric study,

a set of conclusions can be obtained from the above analysis about ANFIS based methodology. For a step training (1W & 3W) and an intermediate step recovery (2W) of results, a combination of "three linguistics variables," "gauss-tri input membership function combinations," constant output membership function, and hybrid optimization technique yields a better recovery of the data set.

7.3.2 Application of the methodology for heat flux recovery

The present section is mostly focused on the implementation of the methodology proposed in the previous section. Here, a different set of signals with varying magnitude and frequency are recovered from the trained ANFIS system using the best training combinations. After recovering the results, the assessment of the accuracy level of the recovered results is carried out in comparison with the known results.

Recovery of heat flux in a definite range

Accuracy of recovery is expected to be reasonable if the heat flux is to be recovered in the range of data considered for training purposes. This subsection deals with the effect of the span of the range on the presently proposed heat flux recovery technique. A step heat flux corresponding to 2W is planned for recovery after training the system with different step inputs. The following case studies are considered:

1. Case-1: The ANFIS system is trained with time-temperature- heat flux data sets of 5W and 4W for the recovery of 2W
2. Case-2: The ANFIS system is trained with 3W and 4W for the recovery of 2W
3. Case-3: The ANFIS system is trained with 5W, 4W and 3W for the recovery of 2W
4. Case-4: The ANFIS system is trained with 1W & 3W for the recovery of 2W

Results obtained for these cases are given in **Fig. 7.7**. It can be observed from all the plots that after an initial transient, the predicted steady-state value matches well with the input within an RMSE band of 0.018 ± 0.01. The results imply a close prediction of the time-varying heat flux with the input parameter. Thus, it can be concluded that the prediction within the range is very much feasible with the presently proposed soft computing technique. But it is worth noting that the mid-range of the training data sets

(i.e., case-4) gives a better prediction in terms of trend and magnitude as the RMSE is the lowest (0.00926).

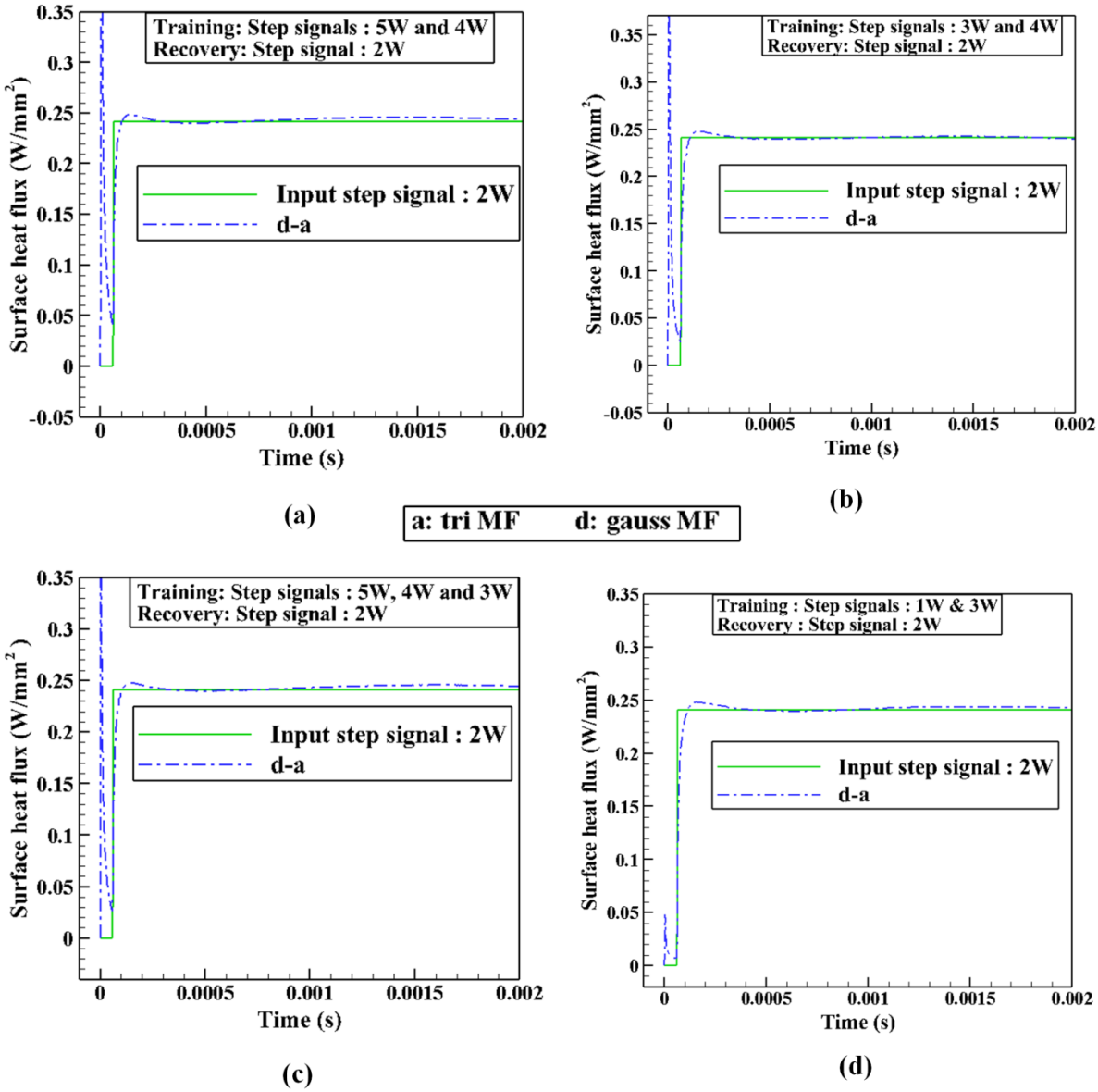

Fig. 7.7: Effect on different modes of training. (a) Training with far upper range, (b) Training with nearest upper range, (c) Training with both far and near upper range, (d) Training with nearest lower and upper range.

Recovery of temporal variation of heat flux

After the successful recovery of overall magnitude, it is planned to check for the recovery of the trend of the heat flux signal by training the ANFIS system with step and ramp heat loads, bearing the same peak magnitude. In this case, the heat loads correspond to the 3W step and 3W ramp with an initial slope (R_3-θ_1). For the recovery, a ramp signal of the

same magnitude but of a different initial slope (R_3-θ_2) than the one used for training is considered. The results show a small decrement in ramp angle (**Fig. 7.8 (a)**) from the input value; however, the peak value matches nicely for a sufficient duration. The prediction errors (RMSE) in this case are in the range of 0.04± 0.01.

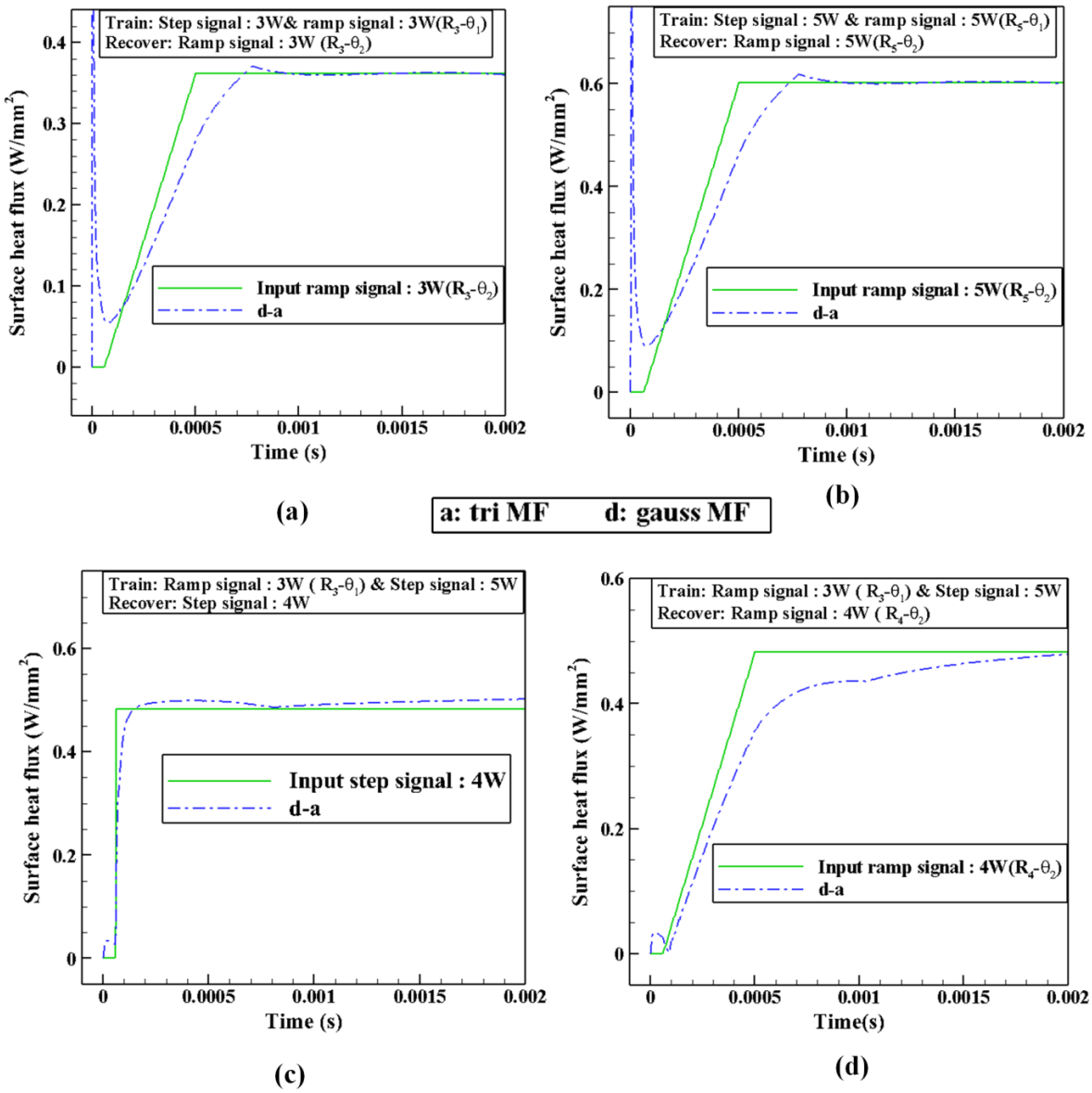

Fig. 7.8: Recovery of signal with different frequency and recovery of random signal: (a) Training wattage (3W) with different ramp angle; (b) Training wattage (5W) with different ramp angle; (c) Recovery of a random signal of a different wattage (4W step) than training (d) Random signal of a different wattage (4W ramp) than training.

A similar process is repeated for higher wattage (5W) signals, but now the system is trained with a step signal of 5W and ramp signal of 5W (R_5-θ_1) for recovery of a ramp of 5W (R_5-θ_2). Here as well, the predicted peak magnitude matches with the input but with a

slightly lower ramp angle as was in the previous case (**Fig. 7.8(b)**). The predicted results are within an RMSE range of 0.09 ±0.02. It can be concluded from this subsection that the currently proposed ANFIS based heat flux recovery technique is able to predict the trend of the signal within an appreciable error range.

Recovery of heat flux of different trends and magnitude

After recovering the step and ramp signals, it is proposed to recover a random signal for which the system is trained with a 3W ramp signal (R_3-θ_1) and 5W step signal. Here, recovery is planned for a step of 4W and a ramp of 4W (R_4-θ_2). For both cases, the prediction results are nearly close to the input signal, but the error range varies compared to the previous results. The RMSE value is 0.026 in the case of 4W step prediction and 0.051 for 4W ramp prediction. Although minor, the deviation is expected due to the less input training data sets for the arbitrary signal recovery. Therefore, it is recommended to have a sufficient number of training data set for the recovery of the surface heat flux having different trends and magnitude for further improvement of error.

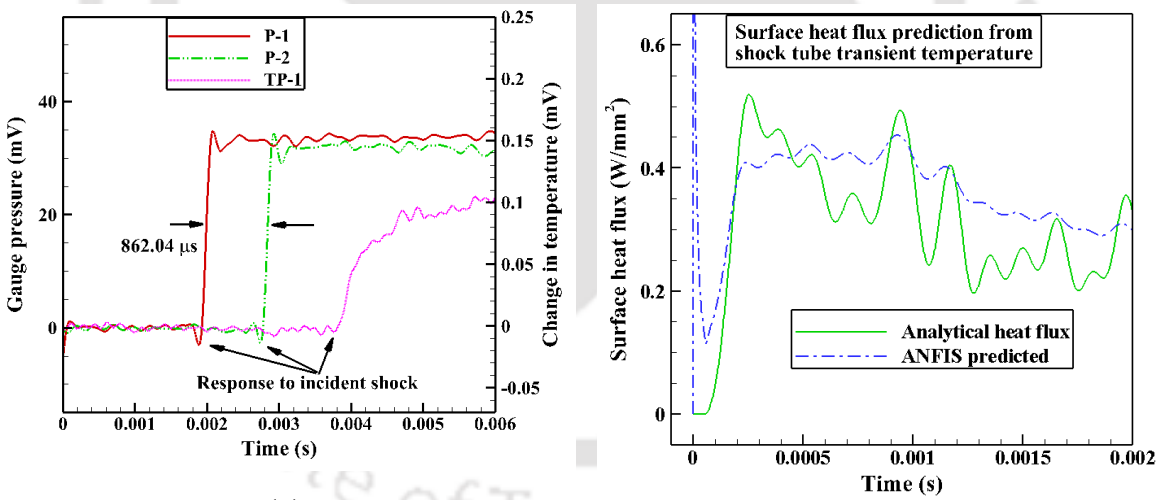

Fig. 7.9: Experimental signals from shock tube. (a) Shock tube pressure and temperature history, (b) Comparison of surface heat flux signals from temperature history (Analytical approach vs. ANFIS).

7.3.3 Recovery of heat flux in case of shock tube experiments

The recovery of results seen till now for step and ramp signals gives confidence about the current proposition, since its prediction matches very well with the input. But it is worth noting that all the training and testing data sets are numerically obtained. Hence, before

recommending this training and testing procedure, it is customary to apply it on a similar real-time experimental signal and cross-verify the possible recovery. Therefore, the temperature signals obtained from the shock tube experiment (Chapter 5) is used for the heat flux recovery.

Shock-tube experimentation

The experimental results obtained from the shock tube experimentation, as explained in Chapter 5, have been considered for the analysis purpose. The static position temperature signal obtained from the sensor TP-1 (**Fig. 5.7(a))** has been taken for analysis. The test period of 2 ms is considered from this signal for the heat flux recovery after training the system **(Fig. 7.9 (a))**. Apart from this, the recorded temperature and the conventional process are also used to recover the heat flux. Thereafter, the analytical and ANFIS based recovered heat flux values are compared.

Recovery of surface heat flux for shock tube experiments

With the confidence of previously recovered results, it is planned to recover an unknown real-time surface heat flux signal from the experimental temperature obtained from the shock tube. Therefore, with the present experience, it is proposed to train the system with a set of step and ramp signals as available from numerical simulations. To do so, the "time-temperature-surface heat flux" data sets for step response from 1W-5W and the ramp response from 1W-5W (R_1-θ_1 to R_5-θ_1 and R_1-θ_2 to R_5-θ_2) are considered for training the system. In order to assess this recovery, heat flux is obtained using the analytical method, as discussed in Chapter 2. The results show an appreciable match with the heat flux obtained from the same temperature signal through the analytical method. As observed previously, the inherent nature of the analytical method is an initial rise and then the attainment of a steady-state where the average magnitude over predicts the input value by 5% (**Table 4.1**). The analytical heat flux signal here also follows a similar trend (**Fig. 7.9(b)**). Both the signals (ANFIS recovered as well as analytical) follow the same trend. Thus, the present efforts certify the use of ANFIS based recovery algorithm for the estimation of heat flux from the temperature signal.

Summary from the convection based recovery

Current studies propose a methodology for the prediction of surface heat flux experienced in impulsive testing from the temperature measurements using soft computing based ANFIS technique. The conventionally adopted analytical method is also considered herein for comparison of recovery in terms of magnitude and trend. Initially, CFD simulations are carried out to model a coaxial thermal probe to get the necessary temperature-time history for different input heat flux variations (such as step and ramp nature). The numerically obtained temperature signals and the associated applied heat fluxes of different wattages and temporal variations are used to train the system using different user inputs like input membership functions, output membership functions, epochs, etc. An outcome of these parametric studies is a recommendation of inputs for better accuracy and lesser computational time. Thus recommended ANFIS structure is trained and assessed for recovery of step heat loads in a definite range, recovery of the heat load of certain temporal variation, and then a random heat flux. In each case, the presently proposed methodology is found quite capable of predicting the trend and the magnitude within an error band of ± 5%. Then heat flux is recovered from shock tube temperature signal using a similar training strategy as well as with the conventional analytical technique. The encouraging agreement is noted between the two methods in trend as well as the steady-state magnitude within an error band of ± 2 %. With the current explorations and assessment, the soft computing technique ANFIS is found suitable for the prediction of surface heat flux in transient measurements, commonly performed in impulse test facilities.

7.4 Heat flux prediction in a radiation-based experiment

After getting appreciable results for heat flux in the convective mode of heat transfer (shock tube flows), it is planned to explore the heat flux recovery in radiation mode using the similar ANFIS approach. The fabricated thermal sensor can also be applied for the measurement of radiation heat flux in many engineering applications hence the accuracy of predicted heat flux is also matters a lot. Like in the case of convection mode, known sets of temperature and corresponding heat flux data are also required to train the system. Laser-based experiments are performed for this purpose to obtain the temperature signal from a step heat load using different laser wattages (2w-3.5W). A detailed description of

the laser setup has been elaborated in Chapter 4. The laser light is allowed to fall on the in-house fabricated thermal probe (CTP), and corresponding temperature values are obtained.

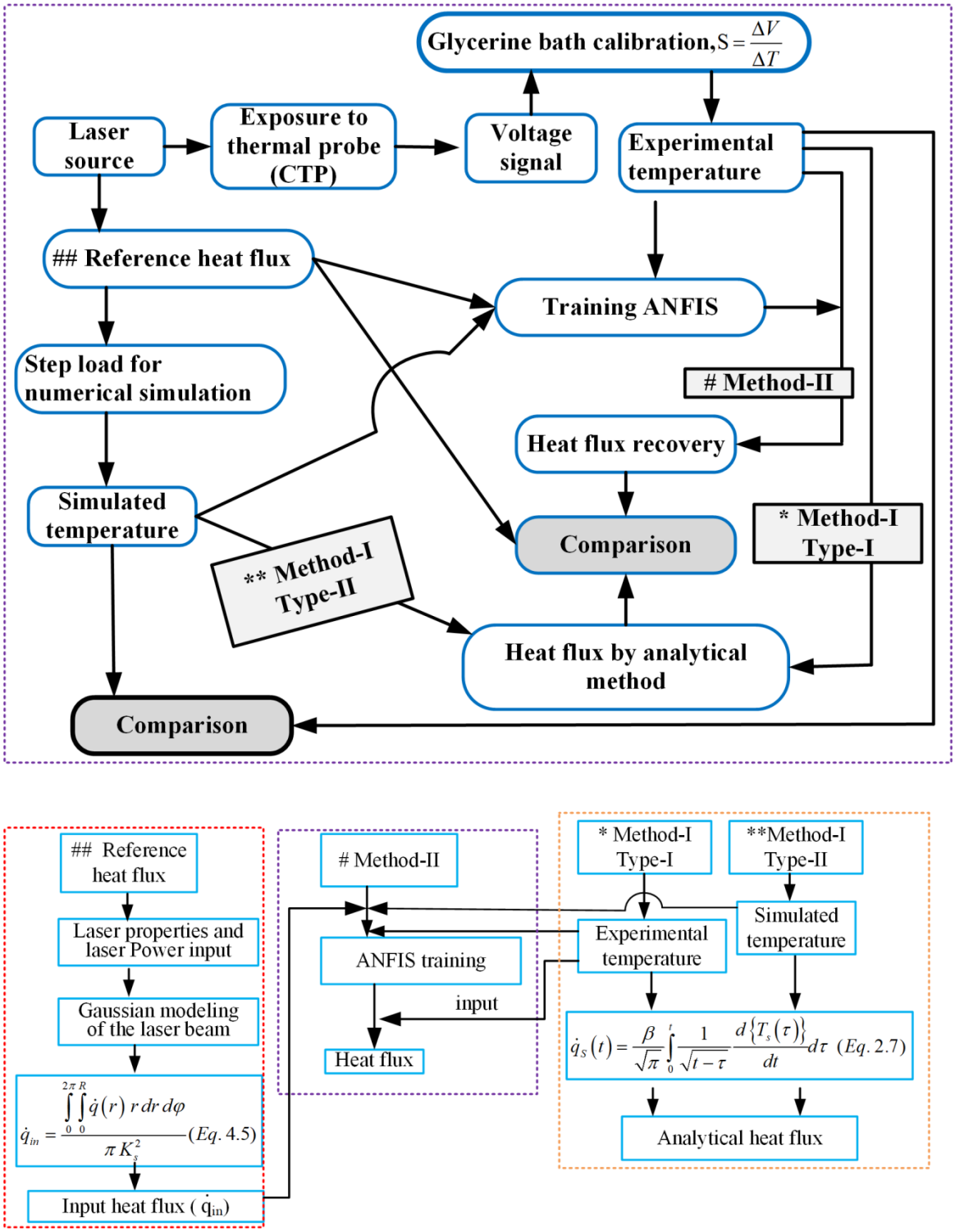

Fig. 7.10: Schematic of heat flux recovery using ANFIS approach.

The data obtained from the laser experiment (i.e., "time-temperature-heat flux") are used to train the ANFIS system. The schematic of the process followed to develop and assess the methodology proposed for heat flux recovery is given in **Fig. 7.10**. After experimenting with different IMF, OMF, and optimization methods available in the Matlab platform, it is observed that the "gauss-tri," "gauss2-tri," and "gbell-tri" IMF combinations yield better results where the first MF belongs to "time" and second for "temperature." Out of them, the "gauss-tri" combination is considered as the best since it gives a good match for trend and leads to the least root mean square error (RMSE) of (0.1 ± 10%). The detailed methodological approach has been elaborated in the previous sections. The "constant" OMF and hybrid optimization type support better results prediction. The "grid partition" type ANFIS architecture is proposed herein for better recovery of short-duration surface heat flux. All these choices of ANFIS are evolved through numerous attempts. Best options are finally recommended, and they are based on minimal RSME value.

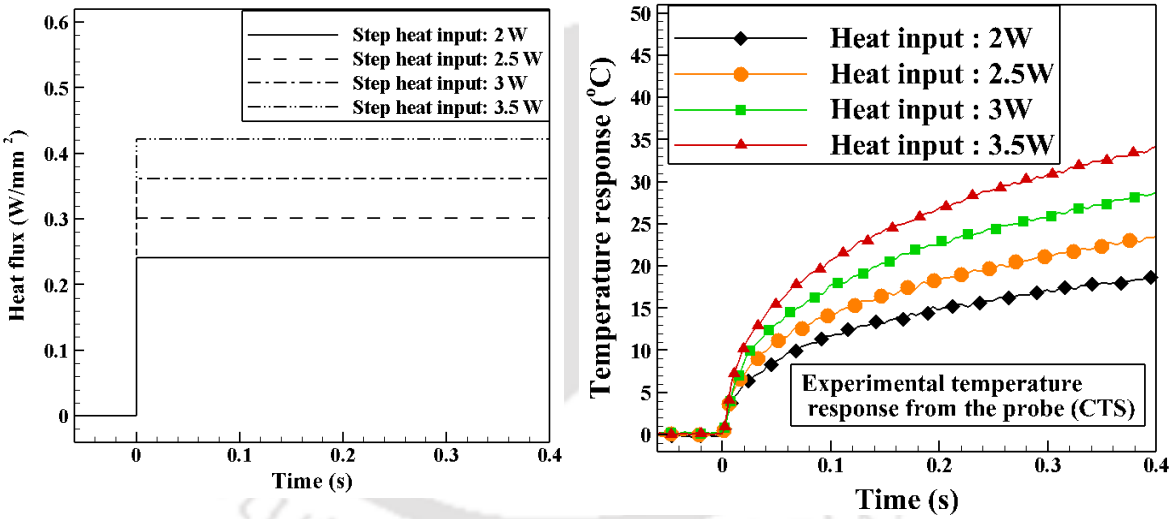

(a) (b)

Fig. 7.11: Input and output from Laser-based experiment: thermal probe; (a) Step heat input; (b) Temperature response.

7.4.1 Laser-assisted heat load experiments

One of the forms of short-duration heat load resembles the nature of step-function. Such a function can be realized in a simulated environment by exposing the probe with a laser heat source, as shown in **Fig. 7.11.** The detailed experimental approach and laser setup have been explained in Chapter 4. The temperature signals corresponding to the

laser heat loads 2W, 2.5W, 3W, and 3.5W are recorded for 0.4s and used for training and recovery purpose (**Fig. 7.12**).

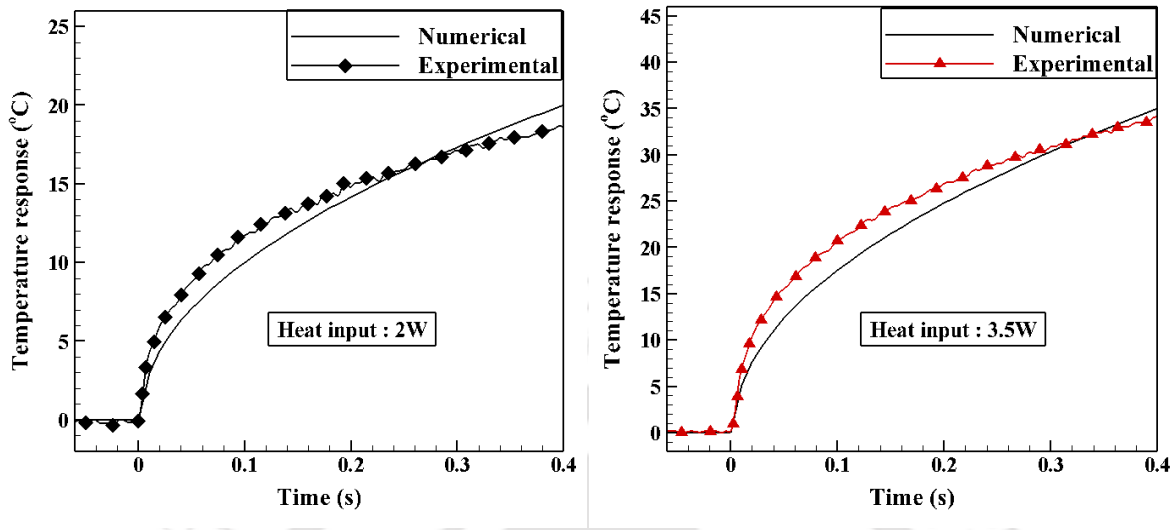

(a) (b)

Fig. 7.12: Comparison of experimental and numerical temperature signals from the thermal probes at different laser wattages: (a) 2 W; (b) 3.5 W.

7.4.2 Data analysis for interpretation of surface heat flux

One of the main intentions is to introduce data-driven soft computing (through ANFIS) as a potential approach for the recovery of heat loads during short-duration experiments. Against this backdrop, the present section illustrates the pattern and behavior of heat flux recovered through different methods as mentioned in the flowchart (**Fig. 7.10**) and subsequently evaluates the effectiveness of the ANFIS approach as compared to conventional data reduction techniques. First, the temperature signal obtained using a laser-based experiment is processed analytically (Method-I) through the classical method of heat flux recovery i.e., by modeling the sensor as a semi-infinite body with one-dimensional heat conduction. The analytical results infer a trend, which bears a high peak during the initial period and is followed by a decay in magnitude. Referring to **Fig. 7.13,** the heat flux results obtained by using numerical signal (Method-I, type-II) follow a similar trend as analytical estimate (method-I, Type-I) with a smaller initial peak which can be inferred as a closer estimate of data with experimental heat flux. The results also have a very small deviation among themselves (± 2%). It is worth mentioning here that heat flux can be recovered not only using experimental temperature signals but also simulated signals through computation. Further, recovery using both temperature signals

has also encouraged agreement. But, the time-averaged magnitude is well within an acceptable range when compared with the experimentally applied heat flux. On the other hand, the advanced approach of heat flux recovery is data-driven and well-trained ANFIS system (Method-II). Here, the system is trained for temperature values obtained from both experimental as well as through separate numerical simulations. Subsequently, heat flux is predicted through well trained ANFIS network with robust prediction.

7.4.3 Implementation of ANFIS technique

With reference to the prior application of soft computing algorithms to several research areas, an attempt is made herein for the prediction of the surface heat flux. It is noted from different iterations that the prediction is better if the applied heat flux falls in the training range. The recovery of surface heat flux is implemented through ANFIS for any transient temperature data (Method-II). Therefore, the temperature history obtained from the laser-based experiment as well as from numerical simulations for step heat load (2 W and 3.5 W) are used to train the system.

Table 7.5: ANFIS training combination of temperature signals.

Training Categories	Temperature signals from step input wattage 2 W	Temperature signals from step input wattage 3.5 W	Remarks
Case-I	Numerical	Numerical	Prediction of intermediate heat flux signal (2.5W & 3W)
Case-II	Numerical	Experimental	
Case-III	Experimental	Numerical	
Case-IV	Experimental	Experimental	

Referring to **Table 7.5**, the “time-temperature-heat flux” values are fed to the ANFIS system as training data where “time and temperature” are inputs and “heat flux” is the output. The intermediate heat flux values corresponding to 2.5W and 3W step loads are recovered from the trained system with corresponding “temperature history” as input. An exercise is also attempted by training the system separately or in a combined manner with the numerical and experimental signals to find the deviation in the recovery. As an outcome, intermediate recovery results are shown in **Fig. 7.13**.

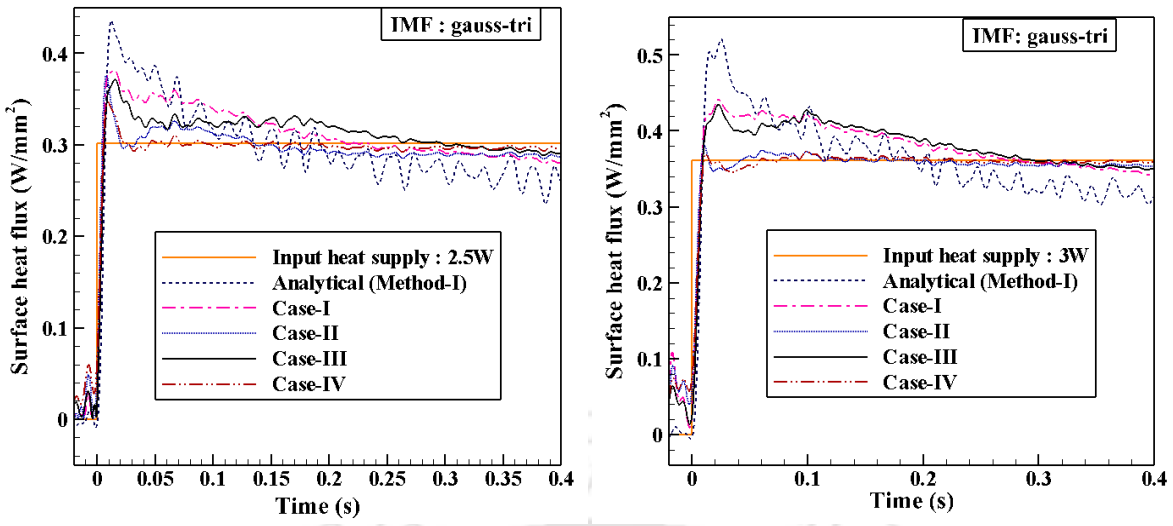

(a) (b)

Fig. 7.13: Comparison of heat flux histories recovered through analytical and soft computing methods: (a) 2.5 W; (b) 3W.

7.4.4 Summary from the radiation-based recovery

A measured signal from a coaxial temperature sensor (E-type) has been the focal point of present investigations for a short experimental time scale. This thermal probe is then subjected to laser light of known wattage in an exclusively designed experimental setup to acquire the corresponding temperature history. The recorded temperature signals are processed to obtain the heat flux using a classical method, which has the basis of heat transfer through a semi-infinite body. A similar set of heat flux signals is recovered through the soft computing based ANFIS technique. The step heat loads of magnitude 2W and 3.5W heat loads are adopted in the training phase, while the intermediate heat flux signals of step magnitude (2.5 W and 3 W) are recovered using the trained ANFIS network. Such training process includes the values of time, temperature, and corresponding heat flux from their signals. The results are found to be in line with the applied heat loads as well as the prediction using the conventional technique for all the possible training cases. It is worth mentioning here that; the training data sets of heat flux and corresponding temperature signals are considered either from experimental measurements, computational results, or both. Thus, feasibility has been verified herein for the possible use of the soft computing technique (ANFIS) to recover any short-duration signal. Beyond the reduced mathematical complications, the leverage to use the available data sets from the experimental measurements and computational results for

training widens the application envelop of soft computing techniques for heat flux recovery. At the time of unavailability of experimental temperature signal, the numerical signal alone can be considered for training the system. Therefore, present studies recommend using soft computing technique (ANFIS) since it has portrayed its ability to recover the time history of surface heat flux with all possible combinations of the training data set with sufficient accuracy. One of the main intentions is to introduce a data-driven soft computing approach (through ANFIS) as a potential approach for the recovery of heat loads during short-duration experiments. It will increase the confidence level and improve the uncertainties band of experimental data, mainly for short duration flows prevailing in shock tunnels and hypersonic wind tunnels. As an overall conclusion, the soft computing technique is recommended for the recovery of heat flux with a suitable training strategy since it neither needs any assumptions for simplification nor intense mathematical understanding and computations.

CHAPTER 8

Conclusion and scope of future work

8.1 Conclusion

The assessment of surface heat flux for short-duration experiments is one of the primary aspects of the present investigation. In line with this, a novel soft computing approach has been adopted and successfully implemented for the heat flux assessment. The training data set for the soft computing technique (ANFIS) has been acquired through laser based experiment using an in-house fabricated coaxial thermal probe and from numerical simulations by modeling the same probe. The fast response characteristics of the probe enable the transient temperature measurement, and these temperatures are the prime ingredients for the heat flux assessment. The probe has been fabricated from the chromel and constantan alloys which are the thermo-elements for the E-type thermal probe. The sensitivity and thermal product of the probe has been obtained experimentally. the probe is employed in a shock tube study to estimate heat flux for short duration experiment. Along with this, the fast response characteristics have been tested and utilized to capture the transient temperature signal at the exhaust of an internal combustion engine, and from the data, the engine cycle time has been predicted. The heat content carried by the exhaust gas has been estimated using the CTP. Most of the objectives are accomplished through this research work. Some of the important findings have been listed here as follows.

- Design and modeling of the probe: The constituent thermo-elements forming the probe should have nearly close thermal properties to avoid temperature gradient along the lateral direction. The minimal insulation thickness helps in avoiding localized heat dislocation. The junction thickness also plays an important role in the response characteristics of the probe. A sensor length of 10 mm is sufficient to have the analytical modeling with semi-infinite substrate assumption.
- Fabrication and mechanical characterization of the probe: The flatness of the sensing surface helps in capturing uniform heat load on the surface. From the abrasion technique of junction formation, the use of water paper provides a better junction which can be confirmed from the FESEM image. A nearly equal or little

deviation in the junction width than the insulation thickness (~20 µm) confirms the accuracy of the fabrication technique.

- Thermal calibration of the probe: The process of static calibration using glycerin bath and the furnace are effective in their way. The use of glycerin helps avoid expansion of the medium, as observed in silicone oils. For the experimental determination of thermal product value, the "water plunging" and "water droplet" methods are adopted. The water droplet method provided more convenient results compared to the water plunging. The gradual stepping and pre-sensing of temperature are the major problems associated with the plunging technique. The thermal product values obtained are in the range of 8442 ± 5% J/m^2 K $s^{0.5}$ and 8673 ± 5% J/m^2 K $s^{0.5}$, respectively, for plunging and droplet techniques. A heat flux calibration is performed with the help of laser light as a step heat load. The temperature response is post-processed to determine heat flux by analytically modeling the sensor as a semi-infinite body with one-dimensional heat conduction. The input heat flux is calculated by assuming the laser beam intensity to obey the Gaussian distribution. The heat flux is also calculated by numerical simulation using the temperature signal as input. In all the cases, the heat flux values are found matching for 0.4s with a maximum uncertainty band of ± 5.64 %.
- Application of the probe for step heat load: The probe is used for flow diagnostics in the IITG shock tube. The response behavior of the probe is checked at the static as well as stagnation location against the standard high-frequency pressure transducer. The rise time of the probe is 210 µs against the rise time of the pressure transducer of 197 µs which justifies its fast response characteristics. Apart from this, the pressure transducer and the thermal probe respond at the same time to the induced mass traveling towards the end flange. Therefore, these probes can be used as a replacement for finding the shock Mach number in the shock tube. The response is also validated against a reference silver thin film gauge at the end flange (stagnation location), and the rise time of the probe is 265 µs against the rise time of the TFG of 240 µs. The stagnation heat flux value from CTP for a particular flow condition is compared with the heat flux obtained from a thin-film gauge. The results match with a maximum error band of ± 2.8 %.
- Application of the probe for cyclic heat load: The fast response characteristics of the probe have been utilized to capture the transient temperature signal at the

exhaust of the internal combustion engine. The cycle time of the engine has been calculated inversely from the temperature response. The transient heat flux signal has been estimated from the temperature signal. Nearly equal peaks of the heat flux signal (500 ± 50 kW/m^2 for 1500 RPM and 550 ± 50 kW/m^2 for 1700 RPM) indicate about the capability of the probe to capture the transient heat flux. Therefore, this probe can be used to evaluate the engine health from external measurements.

- Soft computing based prediction of heat flux for short duration experiments: In the end, ANFIS approach has been exercised for the transient temperature to estimate the unknown heat flux signals. The system is trained with a known time-temperature-heat flux signal, and from the trained system, the unknown heat flux is predicted for known temperature input. The Gaussian and triangular membership function for time and temperature, respectively, yields a better result. The recovered heat flux results are well within an acceptable root mean square error value of ± 0.025.

8.2 Response characteristics of coaxial thermal probe

As discussed in previous sections, it is evident that the in-house designed E-type CTP is found to be capable of responding at a faster rate with respect to temperature change. In particular, the probe has been effectively utilized to capture information pertaining to high-density, and high enthalpy flows prevailing in a shock tube. While mounting at the driven section of the shock tube, it responds instantaneously in a similar manner along with the pressure transducer. The distinct features of primary and reflected shocks could be easily traced from the transient response of the probe in line with the pressure transducer. Again at the location of the end flange, the response behavior of CTP is similar to a "stagnation probe" since it experiences a "hot momentary temperature reservoir" for which high velocity induced air comes to rest. Referring to signals of pressure transducers (PP 4) and CTP (TP 2) in **Fig. 5.7**, there is a rise of pressures and temperatures corresponding to stagnant flow in the vicinity of the end flange. However, it does not retain for a long time, followed by a drop in pressure and temperature values.

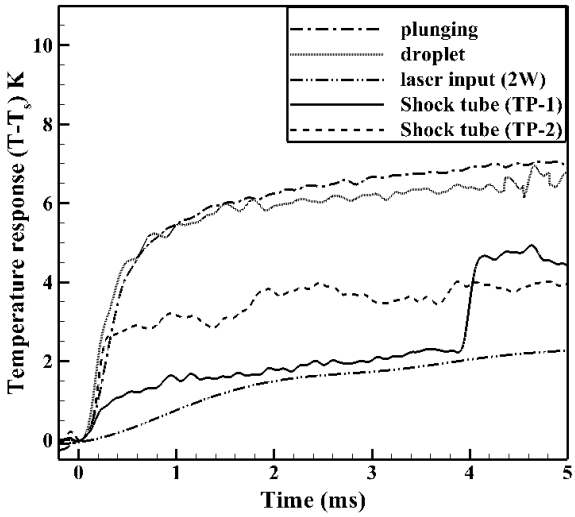

Fig. 8. 1: Response characteristics of CTP for different flow regime.

This fact is an indication of the end of the test time in the shock tube followed by the arrival of multiple waves and their complicated interactions. Further, the occurrence of any interaction between different waves depends upon the shock tube driving conditions, which is accounted for by the change in the pattern of the temperature signals. By revisiting the temperature signals for all the experiments, it is possible to quantify a characteristic response factor $\left(\Delta T_s/\Delta t\right)$ as depicted in earlier references (Agarwal and Sahoo, 2018). The surface temperature history for TP 1 and TP 2 resembles the nature of 'ramp,' which otherwise should resemble the nature of "step" corresponding to a pressure transducer (**Fig. 8. 1**). The possible reason could be the inherent nature of the thermal inertia of the sensing surface of the probe. The higher magnitude in temperature rise for TP 2 is mainly for heated stagnation gas, which remains the same for the test duration. In contrast, TP 1 experiences a rise in temperatures (2.18 K) during primary shock and a further rise in temperature of (2.673 K) after reflected shock. From this plot, the temperature gradient $\left(\Delta T_s/\Delta t\right)$ for both the probes are calculated and presented in **Table 8.1.** As a representative nature of this number, these values were compared with all other experiments discussed in earlier sections. It is an indication that this in-house make CTP is capable of responding to transient flow phenomena, i.e., higher is the impulsive thermal loading, faster is the response characteristics of the probe. The complete information and summary sheet of the research work is given in **Table 8.1**.

Table 8.1: The in-house make E-type surface junction probe and its response parameters.

Research acomplishments			Remarks
Design of the CTP	**Diemensional Features**	E-type probe: 11 ± 1 mm	# High sensitivity and nearly similar properties of thermo-elements (Chapter 2)
		Length: 10 ± 0.2 mm	# Semi-infinite substrate (1-D numerical simulation (Chapter 2)
		Diameter: Outer: 3.25 ± 0.02 mm Inner: 0.91 ± 0.01 mm	# Material avalability and low cost fabrication technique (Chaper 3)
Fabrication & characterization	**Material composition**	Chromel: Ni (87.1%) & Cr (10.1%) Constantan: Ni (38.4%) & Cu (54.8%)	# EDX technique (Chapter 3)
	Insulating material	Insulating material: # Epoxy resin (~200ºC) #Alumina based adhesive (~1500ºC)	# High temperature probe fabrication (Chaper 3) # High temperature probe fabrication (Chapter 6)
	Probe topography	Insulation thickness: 20 ± 2 µm	# Laboratory scale fabrication (Chaper 3)
		Junction width: 21 ± 2 µm Junction height: 12 ± 5 µm	# FESEM technique (Chaper 3)
Calibration	**Sensitivity**	59 ± 0.5 µV/ºC	# Infered from glycerine bath calibration (Chapter 4)
	Thermal product	8500 ± 200 $J/m^2s^{0.5}K$	# Water plunging and water droplet technique (Chapter 4)
	Response time	(210-250) µs	# Shock tube experiment (Chapter 5)
	Response characteristics parameter $\left(\Delta T_s/\Delta t\right)$	745 ± 20 K/s 4550 ± 30 K/s 5425 ±20 K/s 2676 ± 30 K/s 9245 ± 30 K/s	# Laser-based experiment (Chapter 4) # Water plunging experiment (Chapter 4) # Water droplet experiment (Chapter 4) # Response to primary shock (Chapter 5) # Response to reflected shock (Chapter 5)
Application	**Nature of heat load**	Step heat load	# Shock tube based study (Chapter 5) # Laser assisted experiment (Chapter 4)
		Cyclic heat load	# Experiment in internal combustion engine (Chapter 6)
	Heat flux recovery techniques	Analytical approach	# Modeling with semi-infinite subatrate and 1-D heat conduction (Chapter 2)
		Numerical Simulation	# Using ANSYS transient thermal module (Chapter 2)
		Soft-computing approach (ANFIS)	# Recovery of step, ramp heat load along with signal from shock tube (Chapter 7)

8.3 Future work

After having a thorough investigation about the surface junction probes, starting from fabrication till heat flux estimation, it is experienced that there are still scopes for further improvement in every aspect of the coaxial thermal probe. Some of them are listed below:

1. Design and modeling: The decay time of the present probe is a bit higher, which can be reduced by reducing the sensor dimensions. Therefore, an exercise with a smaller diameter and smaller probe length can be explored for short duration studies obeying the satisfaction of semi-infinite principle.
2. Fabrication and surface junction formation: The junction formed through the abrasion technique provides uncontrollable surface properties. Therefore, a tapered probe can be planned to avoid any artificial junction formation.
3. The thermal product magnitude and the associated uncertainties can be obtained for a different time scale range and standardized. Also, an exercise can be attempted to reduce the thermal product of the present existing sensors.
4. The temperature range for the N-type probe is in the range of K type probe. So, the effectiveness of the N-type coaxial probe can be explored on a laboratory scale.
5. Different optimization techniques (e.g., genetic algorithm, Particle Swarm Optimization, etc.) can be adopted for soft-computing-based heat flux recovery.
6. Under-tailored, tailored and over-tailored operations of the shock tube can be considered to impose known unsteadiness to the sensor. Therefore, the sensor can be tested in the shock tube operated at different conditions.

References

Abdulshahed, A.M., Longstaff, A.P., Fletcher, S. (2015). The application of ANFIS prediction models for thermal error compensation on CNC machine tools. *Applied Soft Computing*, *27*, 158-168.

Agarwal, S. (2018). Surface junction thermal probe for transient measurements–conceptual design to field applications (Doctoral dissertation, Indian Institute of Technology, Guwahati).

Agarwal, S., Sahoo, N. (2018). An experimental investigation towards calibration of a shock tube and stagnation heat flux determination. *International Journal of Aerodynamics*, *6*(1), 18-40.

Agarwal, S., Sahoo, N., Irimpan, K.J., Menezes, V., Desai, S. (2017). Comparative performance assessments of surface junction probes for stagnation heat flux estimation in a hypersonic shock tunnel. *International Journal of Heat and Mass Transfer*, *114*, 748-757.

Agarwal, S., Sahoo, N., Singh, R.K. (2016). Experimental techniques for thermal product determination of coaxial surface junction thermocouples during short duration transient measurements. *International Journal of Heat and Mass Transfer*, *103*, 327-335.

Alam, T., Kumar, R. (2018). Radiation based calibration of thin film gauge for transient measurement. *Measurement*, *128*, 352-361.

Alkidas, A.C., Cole, R.M. (1985). Transient Heat Flux Measurements in a Divided-Chamber Diesel Engine. *Journal of Heat Transfer*, *107*(2), 439-444.

Anderson, J.D. (1990). *Modern compressible flow: with historical perspective* (12). McGraw-Hill: New York.

Anderson, J.D., Wendt, J. (1995). *Computational fluid dynamics* (206), 332, McGraw-Hill: New York.

Assanis, D.N., Badillo, E. (1989). On Heat Transfer Measurements in Diesel Engines Using Fast-Response Coaxial Thermocouples. *Journal of Engineering for Gas Turbines and Power*, *111*(3), 458-465.

Bendersky, D. (1953). A special thermocouple for measuring transient temperatures. *Mechanical Engineering*, *117*.

Bergman, T.L., Incropera, F.P., DeWitt, D.P., Lavine, A.S. (2011). *Fundamentals of heat and mass transfer*. John Wiley & Sons.

Buragohain, M. (2009). Adaptive network based fuzzy inference system (ANFIS) as a tool for system identification with special emphasis on training data minimization (Doctoral dissertation, Indian Institute of Technology Guwahati).

Buttsworth, D.R. (2001). Assessment of effective thermal product of surface junction thermocouples on millisecond and microsecond time scales. *Experimental Thermal and Fluid Science*, *25*(6), 409-420.

Buttsworth, D.R., Stevens, R., Stone, C. R. (2005). Eroding ribbon thermocouples: impulse response and transient heat flux analysis. *Measurement Science and Technology*, *16*(7), 1487-1494.

Caldwell, F.R. (1962). Thermocouple materials. Temperature; Its Measurement and Control in Science and Industry, 2 (2), Reinhold, NewYork, 81-134.

Childs, P.R.N., Greenwood, J.R., Long, C.A. (1999). Heat flux measurement techniques. *Proceedings of the Institution of Mechanical Engineers, Part C: Journal of Mechanical Engineering Science*, *213*(7), 655-677.

Cook, W.J., Felderman, E.J. (1966). Reduction of data from thin-film heat-transfer gages - A concise numerical technique. *AIAA Journal*, *4*(3), 561-562.

Desikan, S.L.N., Suresh, K., Srinivasan, K., Raveendran, P.G. (2016). Fast response co-axial thermocouple for short duration impulse facilities. *Applied Thermal Engineering*, *96*, 48-56.

Diller, T.E. (1993). Advances in Heat Flux Measurements. In J. P. Hartnett & T. F. Irvine (Eds.), *Advances in Heat Transfer, Elsevier, 23*, 279-368.

Diller, T.E. (1999). *Heat flux. The Measurement Instrumentation and Sensors Handbook*. Boco Raton, Florida: CRC Press LLC, 34.1-34.15

El-Hasnony, I.M., Barakat, S.I., Mostafa, R.R. (2020). Optimized ANFIS Model Using Hybrid Metaheuristic Algorithms for Parkinson's Disease Prediction in IoT Environment. *IEEE Access*, *8*, 119252-119270.

Elaziz, M.A., Elsheikh, A.H., Sharshir, S.W. (2019). Improved prediction of oscillatory heat transfer coefficient for a thermoacoustic heat exchanger using modified adaptive neuro-fuzzy inference system. *International Journal of Refrigeration*, *102*, 47-54.

Fay, J.A., Riddell, F.R. (1958). Theory of stagnation point heat transfer in dissociated air. *Journal of the Aerospace Sciences*, *25*(2), 73-85.

Ghosh Roy, A., Peyada, N.K. (2017). Longitudinal aircraft parameter estimation using neuro-fuzzy and genetic algorithm based method. In *AIAA Atmospheric Flight Mechanics Conference*. American Institute of Aeronautics and Astronautics, 3896.

Han, Y., Zeng, W., Zhao, Y., Qi, Y., Sun, Y. (2011). An ANFIS model for the prediction of flow stress of Ti600 alloy during hot deformation process. *Computational Materials Science*, *50*(7), 2273-2279.

Hayati, M., Rezaei, A., Seifi, M. (2009). Prediction of the heat transfer rate of a single layer wire-on-tube type heat exchanger using ANFIS. *International Journal of Refrigeration*, *32*(8), 1914-1917.

Hollis, B.R. (1995). *User's manual for the one-dimensional hypersonic experimental aero-thermodynamic (1DHEAT) data reduction code* , NASA.

http://www.techno-office.com/file/MED_TCS.pdf

Incropera, F.P., DeWitt, D.P., Bergman, T.L., Lavine, A.S. (1996). *Fundamentals of Heat and Mass transfer* ,6. Wiley New York.

Irimpan, K. J., Mannil, N., Arya, H., Menezes, V. (2015). Performance evaluation of coaxial thermocouple against platinum thin film gauge for heat flux measurement in shock tunnel. *Measurement*, *61*, 291-298.

Irimpan, K. J., Menezes, V., Srinivasan, K. (2019). Base heat flux measurement techniques in impulse hypersonic test facilities. *Heat Transfer—Asian Research*, *48*(6), 2414-2427.

Jadhav, A., Peetala, R., Kulkarni, V. (2020). Multi-walled carbon nano-tubes for performance enhancement of thin film heat flux sensors. *Heat and Mass Transfer*, *56*(5), 1537-1549.

Jagadeesh, G.J.R. (2008). Fascinating world of shock waves. *13*(8), 752-767.

Jang, J.S.R. (1993). ANFIS: adaptive-network-based fuzzy inference system. *IEEE Transactions on Systems, Man and Cybernetics*, *23*(3), 665-685.

Kant, R., Joshi, S.N. (2013). Finite element simulation of laser assisted bending with moving mechanical load. *International Journal of Mechatronics and Manufacturing Systems*, *6*(4), 351-366.

Karami, A., Akbari, E., Rezaei, E., Mahmoudinezhad, S., Ashjaee, M. (2013). Neuro-fuzzy modeling of the free convection from vertical arrays of isothermal cylinders. *Journal of Thermophysics and Heat Transfer*, *27*(3), 588-592.

Kovacs, A., Mesler, R.B. (1964). Making and testing small surface thermocouples for fast response. *Review of Scientific Instruments*, *35*(4), 485-488.

Kumar, A., Ghosh, A.K. (2018). Data-Driven Method based Aerodynamic Parameter Estimation from Flight Data. In *2018 AIAA Atmospheric Flight Mechanics Conference*. American Institute of Aeronautics and Astronautics,0768.

Kumar, C.S., Takayama, K., Reddy, K. (2014). *Shock Waves Made Simple*. Wiley-Blackwell.

Kumar, R., Sahoo, N. (2013). Dynamic calibration of a coaxial thermocouples for short duration transient measurements. *Journal of Heat Transfer*, *135*(12):124502.

Kumar, R., Sahoo, N., Kulkarni, V. (2012). Conduction based calibration of handmade platinum thin film heat transfer gauges for transient measurements. *International Journal of Heat and Mass Transfer*, *55*(9), 2707-2713.

Kumar, R., Sahoo, N., Kulkarni, V., Singh, A. (2011). Laser based calibration technique of thin film gauges for short duration transient measurements. *Journal of Thermal Science and Engineering Applications*, *3*(4):044504.

Lando, M., Battipede, M., Gili, P.A. (2007). Neuro-fuzzy techniques for the air-data sensor calibration. *Journal of Aircraft*, *44*(3), 945-953.

Lawton, B., Klingenberg, G., Barton, J. (1996). *Transient Temperature in Engineering and Science*. Oxford University Press Oxford.

Lei, Y., He, Z., Zi, Y., Hu, Q. (2007). Fault diagnosis of rotating machinery based on multiple ANFIS combination with GAs. *Mechanical Systems and Signal Processing*, *21*(5), 2280-2294.

Li, J., Chen, H., Zhang, S., Zhang, X., Yu, H. (2017). On the response of coaxial surface thermocouples for transient aerodynamic heating measurements. *Experimental Thermal and Fluid Science*, *86*, 141-148.

Li, Z.X., Renault, F.L., Gómez, A.O.C., Sarafraz, M.M., Khan, H., Safaei, M.R., Filho, E.P.B. (2019). Nanofluids as secondary fluid in the refrigeration system: Experimental data, regression, ANFIS, and NN modeling. *International Journal of Heat and Mass Transfer*, *144*, 118635.

Madison, D.P. (2013). Thermal Characterization of a gasoline turbocharged direct injection (GTDI) engine utilizing lean operation and exhaust gas recirculation (EGR) (Doctoral dissertation, Michigan Technological Unicversity)

Manjhi, S.K., Kumar, R. (2019a). Performance assessment of K-type, E-type and J-type coaxial thermocouples on the solar light beam for short duration transient measurements. *Measurement*, *146*, 343-355.

Manjhi, S.K., Kumar, R. (2019b). Transient surface heat flux measurement for short duration using K-type, E-type and J-type of coaxial thermocouples for internal combustion engine. *Measurement*, *136*, 256-268.

Marr, M.A., Wallace, J.S., Chandra, S., Pershin, L., Mostaghimi, J. (2010). A fast response thermocouple for internal combustion engine surface temperature measurements. *Experimental Thermal and Fluid Science*, *34*(2), 183-189.

MathWorks, I. (2000). *MATLAB: The Language of Technical Computing. Using MATLAB* (3). MathWorks.

Mavropoulos, G.C., Rakopoulos, C.D., Hountalas, D.T. (2009). Experimental assessment of instantaneous heat transfer in the combustion chamber and exhaust manifold walls of air-cooled direct injection diesel engine. *SAE International Journal of Engines*, *1*(1), 888-912.

Moffat, R. J. (1985). Using uncertainty analysis in the planning of an experiment. *journal of fluids engineering*, *107*(2), 173-178.

Moffat, R. J. (1988). Describing the uncertainties in experimental results. *Experimental Thermal and Fluid Science*, *1*(1), 3-17.

Mohammed, H., Salleh, H., Yusoff, M.Z. (2008). Design and fabrication of coaxial surface junction thermocouples for transient heat transfer measurements. *International Communications in Heat and Mass Transfer*, *35*(7), 853-859.

Mohammed, H., Salleh, H., Yusoff, M.Z., Campo, A. (2010). Thermal product of type-E fast response temperature sensors. *Journal of Thermal Science*, *19*(4), 364-371.

Mohammed, H., Salleh, H., Yusoff, M.Z. (2011). Thermal product estimation method for aerodynamics experiments. *Journal of Engineering Physics and thermophysics*, *84*(4), 849-859.

Mohammed, H.A., Salleh, H., Yusoff, M.Z. (2010a). Determination of the effusivity of different scratched coaxial temperature sensors under hypersonic flow. *International Journal of Thermophysics*, *31*(11), 2305-2322.

Mohammed, H.A., Salleh, H., Yusoff, M.Z. (2010b). Fast response surface temperature sensor for hypersonic vehicles1. *Instruments and Experimental Techniques*, *53*(1), 153-159.

Mohammed, H.A., Salleh, H., Yusoff, M.Z. (2011). Dynamic calibration and performance of reliable and fast-response coaxial temperature probes in a shock tube facility. *Experimental Heat Transfer*, *24*(2), 109-132.

Mohammed, H.A., Salleh, H., Yusoff, M.Z. (2011). The effect of scratch technique on the thermal-product value of temperature sensors. *Thermophysics and Aeromechanics*, *18*(1), 51-64.

Nanda, S.R., Agarwal, S., Kulkarni, V., Sahoo, N. (2017). Shock tube as an impulsive application device. *International Journal of Aerospace Engineering*, *2017*, 2010476.

Nanda, S.R., Kulkarni, V., Sahoo, N. (2016). Design of artificial neuro-fuzzy based methodology for six component force balance. *Procedia Engineering*, *144*, 528-536.

Nanda, S.R., Kulkarni, V., Sahoo, N., Menezes, V. (2019). An innovative approach for prediction of aerodynamic coefficients in shock tunnel testing with soft computing techniques. *Measurement*, *134*, 773-780.

Olivier, H., Gronig, H., Schulze, B. (1995). Instrumentation techniques of the Aachen shock tunnel TH2. *International Congress on Instrumentation in Aerospace Simulation Facilities*, *IEEE*, 1-1.

Ongkiehong, L., Duijn, J. (1960). Construction of a thermocouple for measuring surface temperatures. *Journal of Scientific Instruments*, *37*(6), 221-222.

Pratihar, D.K. (2013). *Soft computing: Fundamentals and Applications*. Alpha Science International, Ltd.

Ramesh, P., Nanda, S.R., Kulkarni, V., Dwivedy, S.K. (2019). Application of neural-networks and neuro-fuzzy systems for the prediction of short-duration forces acting on the blunt bodies. *Soft Computing*, *23*(14), 5725-5738.

Rezaei, E., Karami, A., Yousefi, T., Mahmoudinezhad, S. (2012). Modeling the free convection heat transfer in a partitioned cavity using ANFIS. *International Communications in Heat and Mass Transfer*, *39*(3), 470-475.

Rodiger, T. (2010). The Atomic Layer Thermopile-A new heat transfer measurement technique in fluid mechanics and thermodynamics.(Doctoral dissertation, University of Stuttgart).

Roeser, W F., Dahl, A.I. (1938). Reference tables for iron constantan and copper constantan thermocouples, *Journal of the Research of the National Bureau of Standards*, *20*, *337-355*.

Saeed, R.A., Galybin, A.N., Popov, V. (2013). 3D fluid–structure modelling and vibration analysis for fault diagnosis of Francis turbine using multiple ANN and multiple ANFIS. *Mechanical Systems and Signal Processing*, *34*(1), 259-276.

Sahoo, N. (2007). Experiments on a blunt cone model in a hypersonic shock tunnel, *16th Australasian Fluid Mechanics Conference Crown Plaza, Gold Coast, 2007*, 503-506.

Sahoo, N., Kumar, R. (2016). Performance assessment of thermal sensors during short-duration convective surface heating measurements. *Heat and Mass Transfer*, *52*(9), 2005-2013.

Sahoo, N., Peetala, R.K. (2010). Transient temperature data analysis for a supersonic flight test. *Journal of Heat Transfer*, *132*(8).

Sahoo, N., Peetala, R.K. (2011). Transient surface heating rates from a nickel film sensor using inverse analysis. *International Journal of Heat and Mass Transfer*, *54*(5), 1297-1302.

Sanderson, S.R., Sturtevant, B. (2002). Transient heat flux measurement using a surface junction thermocouple. *Review of Scientific Instruments*, *73*(7), 2781-2787.

Sarma, S. (2017). “Thin film heat transfer gauges for short duration transient measurements” (Doctoral dissertation, Indian Institute of Technology Guwahati)

Sarma, S., Sahoo, N., Unal, A. (2016a). Calibration of a silver thin film gauge for short duration convective step heat load. *Sadhana*, *41*(7), 787-794.

Sarma, S., Sahoo, N., Unal, A. (2016b). Thin-film gauges using carbon nanotubes as composite layers. *Journal of Engineering Materials and Technology*, *138*(4).

Schultz, D.L., Jones, T.V (1973). Heat-transfer measurements in short-duration hypersonic facilities. AGARDograph-AG-165.

Stalker, R. J. (1967). A study of the free-piston shock tunnel. *AIAA Journal*, *5*(12), 2160-2165.

Sumin, M. (2013). Heat flux measurement inside internal combustion engine with gradient heat flux sensor (Master's Thesis, Lappeenranta University of Technology).

Taler, J. (1996). Theory of transient experimental techniques for surface heat transfer. *International Journal of Heat and Mass Transfer*, *39*(17), 3733-3748.

Touloakian, YS. (1970). Thermal Conductivity Metallic Elements and Alloys. Y.S. Touloukian (Ed.), *Thermophysical Properties of Matter*, TPRC data series, *1*, IFI/Plenum press, New York.

Tropea, C., Yarin, A.L., Foss, J.F. (2007). *Springer handbook of experimental fluid mechanics*, *1*, Springer Science & Business Media.

Van der Graaf, F. (1995). Heat flux sensors. *Sensor Set: A comprehensive Survey*, 295-322.

Velmre, E. (2007). Thomas Johann Seebeck (1770-1831). *Estonian Journal of Engineering*, *13*(4), 276-282.

Warnes, L. A. (1994). *Electronic and electrical engineering: principles and practice*. Macmillan international higher education.

Wu, S., Shu, Y.H., Li, J.P., Yu, H.R. (2014). An integral heat flux sensor with high spatial and temporal resolutions. *Chinese Science Bulletin*, *59*(27), 3484-3489.

Yılmaz, F., Ozdemir, A., Sencan Sahin, A., Selbas, R. (2014). Prediction of thermodynamic and thermophysical properties of carbon dioxide. *Journal of Thermophysics and Heat Transfer*, *28*(3), 491-498.

Appendix-A

Uncertainty analysis

In the experiments, quantification of the level of uncertainty is a crucial part of the measurement of different parameters. As such, no measurement can be absolutely perfect, where understanding the limitation in terms of precision in the measurement can help to avoid drawing some unwarranted conclusions. In the present case, the combined effect of all the experimentally measured uncertainties will affect the global uncertainties in predicting the final derived quantity, i.e., "surface heat flux." In general, the uncertainty has two main components, i.e., "bias" (systematic error) which is related to "accuracy," and the "random variation," which comes out of repeated experiments in relation to "precision." The "total accuracy uncertainty (δ_{au})" can be obtained from the instrument-specific uncertainty (δ_{ai}) (Table A1) and other uncertainties considering the contribution from various experimental sources (δ_{ac}) using Eq. A1.

$$\delta_{au} = \sqrt{\delta_{ai}^2 + \delta_{ac}^2} \tag{A1}$$

The aim of uncertainty analysis is to address the aggregate propagation of error into the derived quantity, also known as the "propagation of error." The combined uncertainty can be expressed by Eq. A2.

$$\delta_{cu} = \sqrt{\delta_{au}^2 + \delta_{pu}^2} \tag{A2}$$

Where δ_{cu} is the combined uncertainty, δ_{au} is total accuracy uncertainty, and δ_{pu} is precision uncertainty. Unless otherwise mishandled, the maximum "accuracy uncertainties" for the instruments remain constant, which in most of the instruments are provided by the manufacturer whereas, the precision uncertainties are required to be obtained from the repeated experimental data. The uncertainties related to the present experimental investigation involve the accuracy of instruments in terms of measured data and their subsequent contribution to the global uncertainty of measured parameters. The current experimentation includes few instruments such as a thermometer for calibration purposes, pressure transducers in shock tubes, current source meter, data acquisition system, oscilloscope linked to an amplifier. As per the manufacturer's specification, the errors associated with the mentioned instruments are well within the limit of ± 1%. The absolute values of "accuracy and precision uncertainty" are listed in Table A1. The

uncertainty associated with surface heat flux is a function of surface temperature and the thermal product of the probe. In the case of TFGs, the thermal product (β) is a fixed parameter because the sensing element sits on an insulating substrate, and the thermal parameters (density, specific heat, and thermal conductivity) of the substrate do not change. On the other hand, in the case of CTP, the sensing surface is prepared through plastic deformation of substrate combination (i.e., Chromel and constantan). The overall uncertainty for heat flux assessment accounting for different uncertainties has been evaluated. Table A2 shows the mathematical expressions and estimates of overall uncertainties of measured surface heat flux values. The detailed uncertainty magnitudes have been exhaustively calculated and precisely presented here.

Table A1: Sources of uncertainties.

<table>
<tr><td>Accuracy Uncertain (δ_{ai})
(Instrument specific)</td><td colspan="2">Voltage amplifier: ±0.01% ; Source meter: ±0.035%
Pressure transducers: ±0.009%; Oscilloscope: ±0.004%
Data acquisition system: ±0.0041%; Thermometer: ±0.2 ºC</td></tr>
<tr><td colspan="2">Accuracy uncertainty (calculated) (δ_{ac})</td><td>Precision uncertainty (δ_{pu})</td></tr>
<tr><td rowspan="2">CTP:
(voltage)</td><td>due to lead wires: 1.5 ºC (± 88.5 µV)
due to cold junction compensation: ± 0.1 ºC (5.9µV)
due to data acquisition system (± 0.328 µV)</td><td rowspan="2">deviation in voltage reading:
± 51µV.</td></tr>
<tr><td>Total accuracy uncertainty (δ_{au}) : ± 88.7 µV (Eq. A1)</td></tr>
<tr><td rowspan="2">CTP:
(Temperature, T)</td><td>due to sensitivity: ± 0.7 (0.01ºC)
due to voltage: ± 102.3µV (~1.7 ºC)</td><td rowspan="4">deviation in thermometer reading:
± 0.1 ºC.</td></tr>
<tr><td>Total accuracy uncertainty (δ_{au}) : ± 1.7 ºC (Eq. A1)</td></tr>
<tr><td rowspan="2">CTP:
(Temperature, T_s, T_{ct})</td><td>due to sensitivity: ± 0.7 (0.01ºC)
due to voltage: ± 102.3µV (~1.7 ºC)
due to voltage amplifier: ± 0.47µV (~0.01 ºC)</td></tr>
<tr><td>Total accuracy uncertainty (δ_{au}) : ± 1.7 ºC (Eq. A1)</td></tr>
<tr><td rowspan="2">TFG
(voltage)</td><td>due to lead wires: (± 2 µV)
due to source meter: 0.035% (± 23 µV)
due to data acquisition system (± 2.7 µV)</td><td rowspan="2">deviation in voltage reading:
± 40µV.</td></tr>
<tr><td>Total accuracy uncertainty (δ_{au}) : ± 23.24 µV (Eq. A1)</td></tr>
<tr><td rowspan="2">TFG
(Temperature)</td><td>due to TCR: ± 7.5e-6 (0.003ºC)
due to voltage: ± 23.24µV (~0.16ºC)</td><td rowspan="2">deviation in thermometer reading:
± 0.1 ºC.</td></tr>
<tr><td>Total accuracy uncertainty (δ_{au}) : ± 0.16 ºC (Eq. A1)</td></tr>
<tr><td rowspan="2">*Pressure
Measurement</td><td>due to oscilloscope: ± 6e-4 bar
due pressure transducer: ± 1.35e-3 bar</td><td rowspan="2">*deviation in pressure reading: ± 0.01bar</td></tr>
<tr><td>Total accuracy uncertainty (δ_{au}) : ± 1.48e-3 bar (Eq. A1)</td></tr>
<tr><td colspan="3">*Total Uncertainty in pressure measurement is 0.01 bar (Eq. A2)</td></tr>
</table>

Table A2: Uncertainiy estimates for experimental parameters.

CTP								
	V (μV)	**T (°C)**	**Ts (°C)**	**Tw (°C)**	**Tct (°C)**	**Sensitivity (μV/°C) (Eq. 4.1)**	**Thermal Product (J/m^{2}s$^{0.5}$K) (Eq. 4.2)**	**Heat flux (MW/m^2) (Eq. 2.7)**
Accuracy uncertainty	± 88.7	± 0.2	NA	NA	NA	$S = f(V,T)$	$\beta = f(T_s, T_w, T_{ct})$	$\dot{q}_S = f(\beta, T_s)$
Precision uncertainty	± 51	± 0.1	NA	NA	NA	$\frac{\Delta V^{\#}}{V} = 1.28\times10^{-2}; \frac{\Delta T^{\#}}{T} = 1.57\times10^{-3}$ $\frac{\Delta S}{S} = \sqrt{\left(\frac{\Delta V}{V}\right)^2 + \left(\frac{\Delta T}{T}\right)^2} = 0.012$	$\frac{\Delta T_w^{\#}}{T_w} = 8\times10^{-3}; \frac{\Delta T_s^{\#}}{T_s} = 2.12\times10^{-2}; \frac{\Delta T_{ct}^{\#}}{T_{ct}} = 2.38\times10^{-2}$ $\frac{\Delta\beta}{\beta} = \sqrt{\left(\frac{\Delta T_w}{T_w}\right)^2 + \left(\frac{\Delta T_s}{T_s}\right)^2 + \left(\frac{\Delta T_{ct}}{T_{ct}}\right)^2} = 0.03$	$\frac{\Delta\beta^{\#}}{\beta} = 3\times10^{-2}; \frac{\Delta T_s^{\#}}{T_s} = 5\times10^{-2}$ $\frac{\Delta\dot{q}_s}{\dot{q}_s} = \sqrt{\left(\frac{\Delta\beta}{\beta}\right)^2 + \left(\frac{\Delta T_s}{T_s}\right)^2} = 0.058$
Combined uncertainty (Eq. 8)	± 102.3	± 0.22	± 1.7	± 0.22	± 1.7	59 ± 0.7	$\beta = 8673 \pm 260$	3.85 ± 0.22

TFG						
	V (μV)	**T(°C)**	**T_s(°C)**	**TCR(1/K) (Eq. 5.2)**	**Thermal Product (J/m^{2}s$^{0.5}$K) (Table 2.1)**	**Heat flux (MW/m^2) (Eq. 5.2)**
Accuracy uncertainty	± 23.24	± 0.2	NA	$\mathrm{TCR} = f(V,T)$	Constant	$\dot{q}_S = f(T_s)$
Precision uncertainty	± 40	± 0.1	NA	$\frac{\Delta V_0^{\#}}{V_0} = 7.9\times10^{-4}; \frac{\Delta V^{\#}}{V} = 7\times10^{-4}; \frac{\Delta T^{\#}}{T} = 2.85\times10^{-3}$ $\frac{\Delta(\mathrm{TCR})}{(\mathrm{TCR})} = \sqrt{\left(\frac{\Delta V_0}{V_0}\right)^2 + \left(\frac{\Delta V}{V}\right)^2 + \left(\frac{\Delta T}{T}\right)^2} = 0.003$		$\frac{\Delta T_s^{\#}}{T_s} = 4.77\times10^{-3}$ $\frac{\Delta\dot{q}_s}{\dot{q}_s} = \sqrt{\left(\frac{\Delta T_s}{T_s}\right)^2} = 0.0047$
Combined uncertainty (Eq. 8)	± 46.26	±0.22	± 0.16	0.0025 ± 7.5x10^{-6}	$\beta = 1529.67$ (Table 2.1)	3.92 ± 0.018

Data obtained from separate experiments & Table A1.
NA: Not applicable.